

Mathematical Modelling
of
Nucleating and Growing Precipitates:
Distributions and Interfaces

PROEFSCHRIFT

ter verkrijging van de graad van doctor
aan de Technische Universiteit Delft,
op gezag van de Rector Magnificus prof.ir. K.C.A.M. Luyben,
voorzitter van het College voor Promoties,
in het openbaar te verdedigen op
woensdag, 21 januari 2015 om 15:00 uur

door

Dennis DEN OUDEN
wiskundig ingenieur, Technische Universiteit Delft

geboren te Lekkerkerk

Dit proefschrift is goedgekeurd door de promotoren
Prof.dr.ir. C. Vuik
Prof.dr.ir. J. Sietsma

Copromotor Dr.ir. F.J. Vermolen

Samenstelling promotiecommissie:

Rector Magnificus	voorzitter
Prof.dr.ir. C. Vuik	Technische Universiteit Delft, promotor
Prof.dr.ir. J. Sietsma	Technische Universiteit Delft, promotor
Dr.ir. F.J. Vermolen	Technische Universiteit Delft, copromotor
Prof M. Picasso	École Polytechnique Fédérale de Lausanne, Switzerland
Prof.dr.ir. C.R. Kleijn	Technische Universiteit Delft
Dr. H.S. Zurob	McMaster University, Canada
Dr. E. Javierre	Centro Universitario de la Defensa, Spain
‡Dr. L. Zhao	VDL Weweler, The Netherlands
Prof.dr.ir. C.W. Oosterlee	Technische Universiteit Delft, reservelid

‡ Dr. L. Zhao heeft als begeleider in belangrijke mate aan de totstandkoming van het proefschrift bijgedragen.

Mathematical Modelling of Nucleating and Growing Precipitates: Distributions and Interfaces.

Dissertation at Delft University of Technology.

Copyright © 2015 by D. den Ouden



This research was carried out under the project number M41.5.09341 in the framework of the Research Program of the Materials innovation institute (M2i) in the Netherlands (www.m2i.nl).

ISBN 978-94-91909-21-4

Printed by: Proefschriftmaken.nl || Uitgeverij BOXPress

Contents

Samenvatting	vii
Summary	ix
1 Introduction	1
1.1 Background of this thesis	1
1.2 Precipitation models	2
1.3 This thesis	3
I Distributions	9
2 The binary KWN-model	11
2.1 Introduction	11
2.2 The model	12
2.2.1 Elastic stress	12
2.2.2 Nucleation and growth of precipitates	14
2.3 Numerical methods	18
2.3.1 Elastic stress	18
2.3.2 Nucleation and growth of precipitates	18
2.4 Results	20
2.4.1 Application to the Cu-Co system	21
2.4.2 Application to a hypothetical HSLA steel	36
2.5 Conclusions	39
3 The multi-component, multi-phase KWN-model	43
3.1 Introduction	43
3.2 The model	44
3.2.1 Extension to multiple precipitate types	45
3.2.2 Nucleation of precipitates	45
3.2.3 Growth of precipitates	51
3.2.4 Coupling of the multiple precipitate types	52
3.3 Numerical methods	52

3.4	Results	53
3.4.1	Frequency of atomic attachment	54
3.4.2	Multi-component growth	56
3.4.3	Interaction of multiple phases	57
3.4.4	Application to heating	62
3.5	Conclusions	65
4	Modelling the evolution of multiple hardening mechanisms	69
4.1	Introduction	69
4.2	Hardness component model	70
4.3	Nucleation and growth model	72
4.3.1	Nucleation of TiC	73
4.3.2	Growth of TiC	74
4.4	Experimental	76
4.5	Model fitting	77
4.5.1	Input parameters	77
4.5.2	Fitting approach	78
4.6	Results and discussion	79
4.6.1	Fitting parameters	79
4.6.2	TiC-precipitates and recovery	81
4.6.3	Evolution of multiple hardness components during tempering	83
4.7	Conclusions	85
II	Interfaces	91
5	A Fully Finite-Element Based Level-Set Method	93
5.1	Introduction	93
5.2	The Stefan Problem	94
5.2.1	Evolution of the Concentration	94
5.2.2	The Level-Set Method	96
5.3	Numerical Methodology	97
5.3.1	Mesh Generation	98
5.3.2	Discretisation of Equation (5.1)	99
5.3.3	Reinitialisation	101
5.3.4	Calculation of the interface curvature	103
5.3.5	The algorithm	103
5.4	Computer Simulations	105
5.4.1	The experimental accuracy: dissolution of planar and circular precipitates	105
5.4.2	Mixed-mode dissolution	105
5.4.3	Mixed-mode growth	107
5.4.4	Curvature-influenced growth	107
5.4.5	Precipitate breakup	110
5.4.6	Cementite dissolution in austenite	110
5.5	Summary and Conclusion	115

6	The Level-Set Method for Multi-Component Alloys	119
6.1	Introduction	119
6.2	The Stefan Problem	119
6.2.1	Evolution of the Concentrations	119
6.2.2	The Level-Set Method	122
6.2.3	The initial condition	123
6.3	Numerical Methodology	124
6.3.1	Solution of Equation (6.1)	124
6.3.2	Gradient and sum-curvature recovery	125
6.3.3	Obtaining the normal velocity	126
6.4	Numerical tests	127
6.4.1	Sum-curvature recovery	127
6.4.2	The need for and effect of smoothing	128
6.5	Summary and Conclusion	135
7	Conclusions and recommendations	139
7.1	Introduction	139
7.2	Distributions	139
7.2.1	Conclusions	139
7.2.2	Recommendations	140
7.3	Interfaces	141
7.3.1	Conclusions	141
7.3.2	Recommendations	141
A	Proof of Proposition 2.1	143
B	Motivation of Equation (3.13)	147
C	Derivation of Equation (3.37)	153
	Curriculum Vitae	157
	Publications	159

Samenvatting

Staal met een hogere sterkte en een betere vervormbaarheid wordt in toenemende mate vereist door de auto-industrie, omdat ze een hogere veiligheid kan bieden, voor minder energieverbruik zorgen en daarmee leiden tot een betere bescherming van het milieu. Om aan deze eisen te voldoen, is het een duurzame inspanning voor de staalindustrie om hoge sterkte en vervormbare staalsoorten te ontwikkelen. Een van de gangbare werkwijzen voor een dergelijke ontwikkeling is micro-legeren, dat wil zeggen de toevoeging van micro-legeringselementen zoals niobium, vanadium en titaan in een hoeveelheid van enkele honderdste gewichtsprocent leidt tot een zeer uitgesproken sterkte-bevorderingseffect op de staalsoorten, op voorwaarde dat er een adequate hittebehandeling wordt toegepast. Het is duidelijk dat het verstevigende effect voornamelijk voort komt uit een sterke verlaging van de gemiddelde korrelgrootte van het ferriet, afkomstig van het korrelverfijningseffect tijdens de austenisatie-behandeling. De reden voor het korrelverfijningseffect is dat de micro-legeringselementen een zeer sterke affiniteit voor de interstitiële elementen koolstof en stikstof hebben, waardoor zeer fijne en wijdverspreid precipitaten ontstaan. Het bestaan van de precipitaten voorkomt de groei van austenietkorrels via Zener pinning. Daarom is het een essentiële kwestie voor de staalindustrie om een nauwkeurige regeling van de nucleatie en groei van de precipitaten tijdens thermomechanische verwerking van het staal te hebben.

In dit proefschrift zullen we ons richten op modellen die de nucleatie en/of groei van precipitaten beschrijven. Eerst zullen we ons richten op modellen die de evolutie van de precipitaten met behulp van deeltjesgrootteverdelingen beschrijven, uitgaande van het KWN-model en dit model uitbreidend op verschillende manieren. Daarna richten we ons vooral op de grootte evolutie van één precipitaat door het gebruik van level-set methode.

Het KWN-model is uitgebreid met de invloed van elastische spanning, welke voornamelijk leidt tot een verhoging van de nucleatiesnelheid en de gemiddelde radius van precipitaten in de beginfase van nucleatie en groei. Als effect wordt er een kleinere gemiddelde radius bereikt door een snellere uitputting van de matrix. We hebben bovendien het KWN model zodanig aangepast dat alle chemische stoffen die in een legering zitten van invloed zijn op de nucleatie en groei van precipitaten. Het theoretische model geïntroduceerd voor de frequentie van de atomaire aanhechting is de eerste in zijn soort in de literatuur en toont redelijke waarden vergeleken met andere modellen, maar heeft een betere afhankelijkheid van alle chemische stoffen. De

opname van alle chemische elementen in de vergelijkingen voor de groei- en nucleatiesnelheden heeft geleid tot een natuurlijke koppeling tussen verschillende precipitaatfasen en het is aangetoond dat de aanwezigheid van een precipitaatfase significante invloed kan hebben op precipitaatfasen. Tenslotte is het KWN-model gecombineerd met een hardheid-model voor martensitische staalsoorten met precipitaten met een kubusvorm, die dichtbij dislocaties ontstaan. Met behulp van dit hardheid-model hebben wij een fit met experimentele resultaten verkregen. De resultaten tonen aan dat deze modellen nauwkeurig kunnen worden gebruikt om de hardheid evolutie door precipitaten, elementen in oplossing en door dislocatie herstel te voorspellen.

We hebben een mixed-mode model voor de grootte ontwikkeling van willekeurig gevormde precipitaten op basis van verschillende chemische elementen geanalyseerd. Het voorgestelde meshing algoritme, gebaseerd op het huidige niveau van de level-set functie, geeft goede meshes waarop de oplossingen eerste orde experimentele convergentie ten opzichte maaswijdte vertonen. De voorgestelde numerieke methoden voor het binaire model kunnen de interface evolutie gebaseerd op de interface reactiesnelheid en de interface kromming nauwkeurig vangen. Het doorbreken van precipitaten wordt ook correct behandeld. Een belangrijk onderdeel in de level-set methode is de reinitialisatie van de level-set functie tot een afstandsfunctie met teken, waarvoor wij een eenvoudige alternatieve methode voorgestellen. Deze methode maakt direct gebruik van de beschikbare informatie en is ten minste net zo efficiënt als andere veel gebruikte methoden voor reinitialisatie, maar is niet afhankelijk van de gradient van de level-set functie. Verder hebben we een patch-gebaseerde kromming-recovery-methode geïntroduceerd, waarbij een minimale experimentele orde van convergentie van één vertoont. Voor de voorgestelde numerieke methoden voor het model met meerdere componenten hebben we een gevoeligheid voor numerieke artefacten laten zien, die gedeeltelijk kan worden verminderd door toepassing van Laplace smoothing. Dit leidt echter niet tot een robuuste methode. Tot slot is een vergelijking voor de waarde van de interface reactiesnelheid voorgesteld die tot realistische resultaten leidt.

Summary

Steels with higher strength and better formability are increasingly required by the automotive industry because they can provide higher safety, reduce energy consumption and thus lead to a better environmental protection. To meet these requirements, it is a sustainable effort for steel industry to develop high strength formable steels. One of the commonly used methods for such a development is micro-alloying, that is, the addition of micro-alloying elements such as niobium, vanadium and titanium at a level of only a few hundredths of a weight percent results in a very pronounced strength-enhancing effect on the steels, provided that an appropriate heat treatment is applied. It is understood that the strength-enhancing effect primarily arises from a strong reduction in the average grain size of the ferrite, originating from the grain-refining effect during the austenisation treatment. The reason for the grain-refining effect is that the micro-alloying elements have a very strong affinity for the interstitial elements such as carbon and nitrogen, leading to the precipitation of extremely fine and widely distributed precipitates. The existence of the precipitates prevents the growth of austenite grains by means of Zener pinning. Therefore it is an essential issue for steel industry to have an accurate control of the nucleation and growth of the precipitates during thermomechanical processing of the steels. In this thesis we focus on several models describing the nucleation and growth of precipitates.

In this thesis we will focus on models describing the nucleation and/or growth of precipitates. First we will focus on models describing the evolution of particles using particle size distributions, starting from the KWN-model and extending it in various manners. Then we focus primarily on the size evolution of single precipitates by use of the level-set method.

The KWN-model has been extended with the effects of elastic stress, which primarily leads to an increase of the nucleation rate and the mean radius of precipitates in the initial stages of nucleation and growth. As an effect, a smaller mean radius is attained due to a faster depletion of the matrix. We, furthermore, adapted the KWN model such that all chemical species occurring within the alloy influence the nucleation and growth of precipitates. The theoretical model introduced for the frequency of atomic attachment is the first of its kind in literature and shows reasonable values compared to other models, but has a better dependence on all chemical species. The incorporation of all chemical species within the equations for the growth rates and nucleation rates has led to a natural coupling between different precipitate phases and it has been shown that the occurrence of one precipitate phase can significantly

influence other precipitate phases. Finally the KWN model has been combined with a hardness model for martensitic steels containing precipitates with a cubic shape, which nucleate near dislocations. With the use of this hardness model, we obtained a fit to experimental results. The results show that these models can accurately be used to predict the hardness evolution due to precipitate hardening, solid solution strengthening and due to dislocation recovery.

We have analysed a mixed-mode model for the size evolution of arbitrarily shaped precipitates based on several chemical elements. The proposed meshing algorithm, based on the current level-set function gives good meshes on which the solutions exhibit first order experimental convergence with respect to mesh size. The proposed numerical methods for the binary model are able to capture the interface evolution accurately based on the interface reaction speed and interface curvature. Precipitate breakup is handled correctly as well. An important part within the level-set method is the reinitialisation of the level-set function to a signed-distance function, for which we have proposed a simple alternative method. This method makes direct use of the information available and is at least as efficient as other common methods for reinitialisation, but does not rely on the gradient of the level-set function. Furthermore, we introduced a patch-based curvature-recovery method, which exhibits a minimal experimental order of convergence of one. For the proposed numerical methods for the multi-component model we have shown a sensitivity to numerical artefacts, which can partially be reduced by application of Laplace smoothing. This however does not lead to a robust method. Finally, an equation for the value of the interface reaction speed has been proposed which has led to realistic results.

Chapter 1

Introduction

1.1 Background of this thesis

Steels with higher strength and better formability are increasingly required by the automotive industry because they can provide higher safety, reduce energy consumption and thus lead to a better environmental protection. To meet these requirements, it is a sustainable effort for steel industry to develop high strength formable steels. One of the commonly used methods for such a development is micro-alloying, that is, the addition of micro-alloying elements such as niobium, vanadium and titanium at a level of only a few hundredths of a weight percent results in a very pronounced strength-enhancing effect on the steels, provided that an appropriate heat treatment is applied. It is understood that the strength-enhancing effect primarily arises from a strong reduction in the average grain size of the ferrite, originating from the grain-refining effect during the austenisation treatment. The reason for the grain-refining effect is that the micro-alloying elements have a very strong affinity for the interstitial elements such as carbon and nitrogen, leading to the precipitation of extremely fine and widely distributed precipitates. The existence of the precipitates prevents the growth of austenite grains by means of Zener pinning. Therefore it is an essential issue for steel industry to have an accurate control of the nucleation and growth of the precipitates during thermomechanical processing of the steels.

During thermomechanical processing of steels several physical processes occur. During this process the major phase of the steel will transform from ferrite to austenite and vice versa, mainly due to temperature changes. Also nucleation and growth of cementite can occur, which leads in combination with the growth of ferrite grains to more intricate structures, such as bainite, pearlite and martensite. Within these crystal structures both dislocations and precipitates can be present, which both influence the properties of the steel, but also each other. Dislocations are primarily created due to plastic deformation applied to the steel, both at low and high temperatures. These dislocations can recover partially in time due to temperature, but this recovery can be slowed down by precipitates. Furthermore recrystallisation of deformed grains occurs. Based on energetic principles, precipitates are likely to nucleate and grow at or near lattice defects, such as dislocations, and can subsequently pin dislocations,

thereby retarding recovery and allowing for possibly more nucleating precipitates.

In this thesis we focus on several models describing the nucleation and growth of precipitates.

1.2 Precipitation models

Over the course of more than two decades various models for the nucleation and growth of precipitates in alloys have been proposed and evaluated. These models can be divided into five general categories. The first category concerns models which predict the nucleation and growth of precipitates on the evolution of a particle size distribution function. A classical example of this model is the KWN-model by Kampmann and Wagner [1991], which has been extended and evaluated by, amongst others, Robson [2004b]. The second category consists of models that predict the nucleation and growth of precipitates using a mean variable approach, which model the time evolution of variables such as the mean particle radius and the particle number density. An example of such a model has been proposed by Deschamps and Brechet [1999]. The next category contains models that predict the growth and dissolution of precipitates present in a system by solving Stefan-like problems for different precipitate sizes. One of the latest models in this area is developed by Vermolen et al. [2007]. The penultimate category is based on phase field modelling, assuming diffuse interfaces, see for example Hu and Henager Jr. [2009]. Finally a category containing models which describe precipitation dynamics using statistical methodologies can be identified, such as the model by Soisson et al. [1996]. Within this thesis we focus on models based on size distributions as well as on models for the growth of precipitates assuming sharp interfaces.

Currently two major approaches are taken in modelling particle size distribution functions. In both approaches classical nucleation theory predicts the number of nucleating precipitates of a certain size, but the manner in which these precipitates are added to the system differs. In the Lagrange-like approach every (discrete) time-step a new dynamic size-class of precipitates is added, which is tracked individually in time during growth, dissolution and coarsening. In the Euler-like approach a fixed number of static size-classes is predefined and nucleation precipitates are added to the correct size class every time-step. Both approaches make use of equations for the growth rates of precipitates. Again two major lines of thought are present in literature. The first is the so-called Zener approach [Robson, 2004a], where the growth rates of precipitates are determined by approximating the concentration fields around a single precipitates with an analytical solution of the stationary diffusion equation [Zener, 1949]. The second is developed in Svoboda et al. [2004] and uses the global thermodynamic extremum principle [Onsager, 1931a,b] and is currently implemented in the software MatCalc [2012]. In this thesis, we will adapt the Euler-like approach with static size-classes in combination with the Zener approach for growth rates.

Modelling and simulating sharp-interface kinetics can also be done in several ways. One of the most common approaches is by using moving grids, where the sharp interface is embedded explicitly within the (discretization of) the model using moving mesh methods [Segal et al., 1998]. Instead of embedding the moving interface explicitly, the level-set method can also be used [Osher and Sethian, 1988], in which the interface is the zero-contour of an evolving function. There have been several applications of

this approach to growing and dissolving precipitates, see for example Vermolen et al. [2007]. A third and less known approach is by the use of variational inequalities, but is only applicable to one-phase Stefan problems, see for example Ichikawa and Kikuchi [1979] and Vuik [1990]. In this thesis we will apply the level-set technique to the sharp-interface Stefan-like problems governing precipitate growth.

In using the level-set method, the function of which the zero-contour represents the interface of interest, this function is taken in a point \mathbf{x} as the signed-distance from this point to the interface. The signed-distance is defined as the minimum distance to the interface, multiplied with negative one if the the point is within one of the two phases defined. A common problem in using the level-set method is the loss of the signed-distance property, which stems from numerical errors during advection of the level-set function. Recovering the signed-distance property has been the topic of research since the introduction of the level-set method, and is commonly called reinitialisation. Common solution methods are the use of pseudo-time partial differential equations, as proposed originally by Osher and Sethian [1988], fast-marching type methods [See for example Sethian, 1999] and variational methods [See for example Basting and Kuzmin, 2013]. In this thesis we will not make use of any of these methods, but will discuss a new method suited for our applications.

1.3 This thesis

In this thesis we will focus on models describing the nucleation and/or growth of precipitates. In Part I, we will focus on models describing the evolution of particles using particle size distributions, starting from the KWN-model [Kampmann and Wagner, 1991] and extending it in various manners. The chapters in Part I focus on the nucleation of precipitates as well as on the size evolution of (nucleated) precipitates. Part II focuses primarily on the size evolution of single precipitates by use of the level-set method. The chapters in Part II focus on the numerical techniques needed and issues encountered in obtaining an accurate description of evolving precipitates.

We start in Chapter 2 with a short review of the KWN-model. The KWN-model describes the evolution in time of a precipitate-size probability-density function multiplied by the total number density of spherical precipitates present within a system. From this function several quantitative properties of the precipitates can be derived, such as number density, volume fraction, mean radius and average matrix concentrations. The evolution of the particle-size distribution function is governed by two aspects, the first being the nucleation of new precipitates, the second the size evolution of these precipitates. In the KWN-model, nucleation is described using classical nucleation theory, of which an extensive review can be found in Aaronson et al. [2010]. We extend the classical nucleation rate in Chapter 2 by including the effect of elastic stress due to deformations. The size evolution of precipitates is in Chapter 2 described using the Zener approach [Zener, 1949]. This approach assumes around each precipitate of a certain size an instantaneous concentration profile which increases from the local equilibrium at the precipitate-matrix interface to the far-field concentration away from the precipitate. In Chapter 2 a (quasi-)binary approach is taken, in which the slowest diffusing element limits the nucleation rate as well as the growth rates. Subsequently we apply the model to a copper-cobalt alloy and to an HSLA steel.

Although the (quasi-)binary assumption in Chapter 2 gives correct results in many

cases, for more complex systems this assumption is invalid. If for example we consider a steel containing low amounts of carbon and high amounts of niobium, equilibrium calculations indicate nucleation of niobium carbides. We believe the nucleation rates and growth rates of these precipitates can be limited not only by the slower diffusing element niobium but also by the low amount of carbon, as both are needed for the nucleation and growth of niobium carbides. We therefore improve the KWN-model in Chapter 3 by redefining all parameters used within the nucleation rate on a multi-component basis. To this end we propose a theoretical model for the attachment frequency of atoms to a growing particle, which to our knowledge is the first time such a model has been proposed in literature. Furthermore, in Chapter 3 a model for growth rates is proposed which incorporates the Zener approach for multi-component precipitates and the Gibbs-Thomson effect [Perez, 2005]. The new model is thereafter analysed by application to an HSLA steel with several competing precipitate phases to show the benefits of the improved model.

Obtaining precipitate size distributions experimentally is commonly done by Transmission Electron Microscopy (TEM). Due to a resolution of at most 1 Å, TEM is capable of detecting very fine precipitates. However, obtaining an accurate size distribution is time consuming. Also sample preparation for TEM is a difficult process and can cause the structure of the material to be altered. Other options for precipitate detection are Atom Probe Tomography (APT) and Small-Angle Neutron Scattering (SANS). APT has the benefits of obtaining accurate sizes, compositions and shapes of precipitates, but is also prone to failure during experiments and the samples are relatively small, so finely dispersed precipitates might not be present in the sample or only at low numbers in the taken samples, see for example Öhlund et al. [2014], thereby not producing realistic information on precipitate size distributions. SANS does however produce precipitate size distributions [Dijk et al., 2002], but different precipitate types cannot be easily separately detected and the maximum size of precipitate sizes is also limited. In Chapter 4 we will investigate the use of hardness measurements of martensitic steels to predict the precipitate size distributions of titanium carbides in martensitic steels. We will therefore propose a model for the heterogeneous nucleation of cubic-shaped TiC precipitates near dislocations and the subsequent growth of these precipitates. We will introduce an adapted form of the Gibbs-Thomson effect to account for the misfit strain energy associated with the coherently nucleated TiC. This will lead to a consistent model in which nucleating precipitates are of a stable size, i.e. they will not grow or dissolve at the time of nucleation. In Chapter 4 we also introduce a model which can predict the hardness of steels using solid solution strengthening, dislocation recovery and precipitate strengthening and investigate the separate hardening effects. As both models contain several unknown parameters, such as the misfit strain energy, we will use the experimental data from Öhlund et al. [2014] to obtain approximate values and compare these values with literature.

In Part I we have repeatedly made use of analytical solutions for the growth of spherical particles and the surrounding concentration fields. These solutions were possible to obtain by assuming a fixed geometry of the precipitate, stationary concentration fields and local equilibrium near the precipitate-matrix interface. In Chapter 5 we will investigate the growth of single precipitates of arbitrary initial geometry without posing any further restrictions on the development in time of the geometry. We will describe the evolution in time of the precipitate and the surrounding concentra-

tion field by assuming that this development occurs due to a single chemical element, while we do not demand local equilibrium near the precipitate-matrix interface. We will employ the level-set method to capture the geometry of the precipitate and introduce a new approach to the reinitialisation of the level-set function. The governing equations are solved using only finite-element techniques, as this allows for (intermediate) mesh-generation and flexibility, for which novel techniques will be presented. We will furthermore in Chapter 5 investigate the dependence of the precipitate geometry on the physical parameters within the model, such as the interfacial energy between precipitate and matrix.

The assumption of a single chemical element driving the growth of a precipitate is not correct in general. In Chapter 6, in analogy with Chapter 3, we will introduce the multi-component model for the evolution of the precipitate geometry and the surrounding concentration fields, departing from the model introduced in Chapter 5. The techniques needed to solve this complex problem are described in detail and some remaining issues encountered are discussed. We, furthermore, introduce and compare several techniques for the recovery of the interface curvature from the level-set function, of which two exhibit experimental (super-)convergence.

In the last chapter, Chapter 7, we will repeat the major results and conclusions from this thesis and discuss points for future research and possible solution directions.

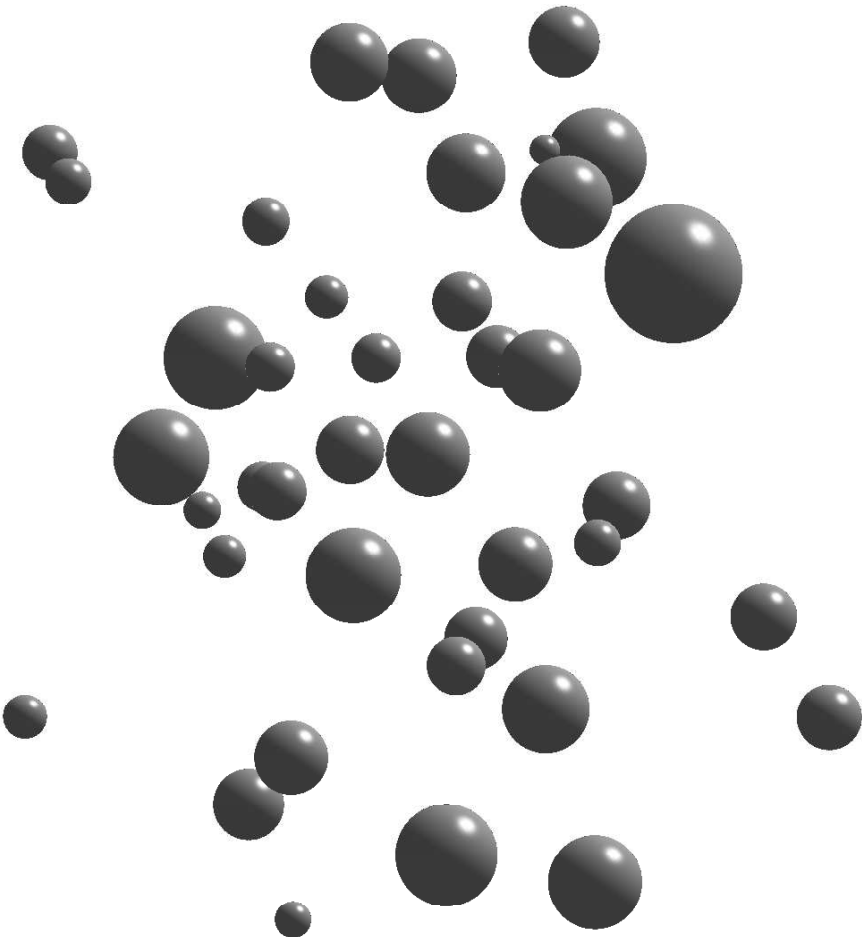
Bibliography

- H.I. Aaronson, M. Enomoto and J.K. Lee. Mechanisms of Diffusional Phase Transformations in Metals and Alloys. CRC Press, Boca Raton, FL, United States of America, 2010.
- C. Basting and D. Kuzmin. A minimization-based finite element formulation for interface-preserving level set reinitialization. Computing, 95(1):13–25, 2013.
- A. Deschamps and Y. Brechet. Influence of predeformation and ageing of an Al-Zn-Mg alloy – II. Modeling of precipitation kinetics and yield stress. Acta Materialia, 47(1):293–305, 1999.
- N.H. van Dijk, S.E. Offerman, W.G. Bouwman, M.Th. Rekveldt, J. Sietsma, S. van der Zwaag, A. Bodin and R.K. Heenan. High temperature SANS experiments on Nb(C,N) and MnS precipitates in HSLA steel. Metallurgical and Materials Transactions A, 33:1883 – 1891, 2002.
- S. Hu and C.H. Henager Jr. Phase-field simulations of Te-precipitate morphology and evolution kinetics in Te-rich CdTe crystals. Journal of Crystal Growth, 311(11):3184–3194, 2009.
- Y. Ichikawa and N. Kikuchi. A one-phase multi-dimensional Stefan problem by the method of variational inequalities. International Journal for Numerical Methods in Engineering, 14(8):1197–1220, 1979.
- R. Kampmann and R. Wagner. Materials Science and Technology - A Comprehensive Treatment, volume 5. VCH, Weinheim, Germany, 1991.

- MatCalc. Institut für Werkstoffwissenschaft und Werkstofftechnologie, 2012. URL <http://matcalc.tuwien.ac.at>.
- C.E.I.C. Öhlund, J. Weidow, M. Thuvander and S.E. Offerman. Effect of Ti on evolution of microstructure and hardness of martensitic Fe-C-Mn steel during tempering. ISIJ International, 54, 2014. IN PRESS.
- L. Onsager. Reciprocal relations in irreversible processes. i. Phys. Rev., 37:405–426, Feb 1931a.
- L. Onsager. Reciprocal Relations in irreversible processes. ii. Phys. Rev., 38:2265–2279, Dec 1931b.
- S.J. Osher and J.A. Sethian. Fronts propagating with curvature-dependent speed: Algorithms based on Hamilton-Jacobi formulations. Journal of Computational Physics, 79(1):12–49, 1988.
- M. Perez. Gibbs-Thomson effects in phase transformations. Scripta Materialia, 52(8):709–712, 2005.
- J.D. Robson. Modelling the evolution of particle size distribution during nucleation, growth and coarsening. Materials Science and Technology, 20:441–448, 2004a.
- J.D. Robson. Modelling the overlap of nucleation, growth and coarsening during precipitation. Acta Materialia, 52(15):4669–4676, 2004b.
- G. Segal, C. Vuik and F.J. Vermolen. A conserving discretization for the free boundary in a two-dimensional Stefan problem. Journal of Computational Physics, 141(1): 1–21, 1998.
- J. A. Sethian. Fast marching methods. SIAM Rev., 41(2):199–235, 1999.
- F. Soisson, A. Barbu and G. Martin. Monte Carlo simulation of Copper precipitation in dilute Iron-Copper alloys during thermal ageing and under electron radiation. Acta Materialia, 44(9):3789–3800, 1996.
- J. Svoboda, F.D. Fischer, P. Fratzl and E. Kozeschnik. Modelling of kinetics in multi-component multi-phase systems with spherical precipitates: I: Theory. Materials Science and Engineering: A, 385(1-2):166–174, 2004.
- F.J. Vermolen, E. Javierre, C. Vuik, L. Zhao and S. van der Zwaag. A three-dimensional model for particle dissolution in binary alloys. Computational Materials Science, 39:767–774, 2007.
- C. Vuik. An L^2 -error estimate for an approximation of the solution of a parabolic variational inequality. Numerische Mathematik, 57(1):453–471, 1990.
- C. Zener. Theory of growth of spherical precipitates from solid solution. Journal of Applied Physics, 20(10):950–953, 1949.

Part I

Distributions



Chapter 2

The binary KWN-model

With applications to a Copper-Cobalt alloy and an HSLA steel under the influence of elastic stress

2.1 Introduction

This chapter presents an adapted KWN-model for homogeneous nucleation and growth of particles by Robson's formalism [2004] which incorporates the effect due to elastic stress. This goal is achieved by introducing strain energy terms. The elastic stress is modelled using standard linear elastic models in cylindrical coordinates, see for example Jaeger et al. [2007] and Chau and Wei [2000]. Furthermore, a numerical algorithm is presented to simulate the influence of the elastic stress on the nucleation and growth of precipitates, which decreases the computational cost significantly without a high loss of accuracy.

In this chapter, we first present the models for the elastic stress, and for the nucleation and growth of precipitates, after which the models are discretised using a finite-element method for the model for elastic displacements and a finite-volume method for the nucleation model. Thereafter the mentioned algorithm for simulating the influence of the elastic stress on the nucleation and growth of precipitates is discussed. The use of the models and algorithm is demonstrated by an application to a Cu-0.95wt%Co alloy, similar to the application by Robson [2004], as for this alloy

This chapter is based on the articles:

D. den Ouden, F.J. Vermolen, L. Zhao, C. Vuik and J. Sietsma. Modelling of particle nucleation and growth in binary alloys under elastic deformation: An application to a Cu-0.95 wt%Co alloy. Computational Materials Science, 50(8):2397–2410, 2011a.

D. den Ouden, F.J. Vermolen, L. Zhao, C. Vuik and J. Sietsma. Mathematical Modelling of NbC Particle Nucleation and Growth in an HSLA Steel under Elastic Deformation. Solid State Phenomena, 172–174:893–898, 2011b.

it is known to a fair extent that primarily homogeneous nucleation of precipitates occurs. Next the results of the influence of elastic stress on a specimen is given and a discussion on the influence of the temperature and the interface energy is presented. Finally the validity of the model is demonstrated by an application to an undeformed hypothetical HSLA steel and subsequently the results of the influence of elastic stress on a specimen are given and discussed.

2.2 The model

The nucleation and growth of precipitates are modelled by the KWN model by Robson [2004]. We present an extensive discussion of this model. The main features of the KWN model are:

- All particles are spherical and classified by their radius in meters (m). In this chapter, we assume that the precipitates are mechanically much harder than the matrix, which causes the shape of the particles to remain spherical during elastic deformation.
- The time behaviour in seconds (s) of the model is described by the partial differential equation:

$$\frac{\partial N}{\partial t} = -\frac{\partial[Nv]}{\partial r} + S, \quad (2.1)$$

in which $N \equiv N(r, t)$ in m^{-3} represents the number density of particles with radius r and at time t , $v \equiv v(r, t)$ in ms^{-1} denotes the growth rate of particles with radius r and at time t and $S \equiv S(r, t)$ in $\text{m}^{-3}\text{s}^{-1}$ represents a source function representing the number of new particles with radius r and at time t per second. The velocity v will be defined in Section 2.2.2.

- The value of the source function S is calculated from classical nucleation theory (CNT) and is given by

$$S(r, t) = \begin{cases} I(t) & \text{if } r \in [r^*(t), 1.05r^*(t)], \\ 0 & \text{otherwise.} \end{cases} \quad (2.2)$$

Here $I \equiv I(t)$ is the nucleation rate of the particles following from CNT and $r^* \equiv r^*(t)$ the critical radius following from CNT. The value 1.05 is adopted from Myhr and Grong [2000]. Both I and r^* will be defined in Section 2.2.2.

- To Equation (2.1) the well-known first-order upwind method is applied, combined with a time integration method.

In this chapter, we also couple the KWN-model with a model for elastic stress.

2.2.1 Elastic stress

In the present chapter we only model the influence of elastic stress applied to a cylindrical test sample on the process of nucleation and growth of particles, however in principle the concept can be extended to regions with different geometries.

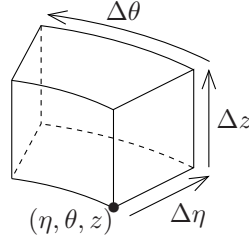


Figure 2.1: *Cylindrical element at (η, θ, z) .*

The concept of elastic stress is simplified under the assumptions of local isotropy, instantaneous displacement, rotation symmetry around the central axis and that a formulation of the model for elastic stress in cylindrical coordinates (η, θ, z) is possible. The symbol η represents the radial coordinate in cylindrical coordinates, as r has previously been defined as the precipitate radius. Furthermore, θ and z represent, respectively, the azimuthal coordinate and the height coordinate in cylindrical coordinates. The latter two assumptions immediately impose restrictions on the formulation of the model. Rotation symmetry implies that at the central axis no radial displacements can occur. This yields the boundary condition

$$u_\eta(0, \theta, z) = 0. \quad (2.3)$$

Furthermore, the assumptions indicate that all displacements are constant with respect to the azimuthal direction θ , i.e. $\partial/\partial\theta=0$, and that in the azimuthal direction no displacements occur, i.e. $u_\theta=0$, at any point in the material.

Consider a small element of the cylindrical test sample, which is of the form as in Figure 2.1. Applying a simple balance of forces in the axial and radial direction and taking the appropriate limits, we arrive at the following system of equations on the domain Ω [Jaeger et al., 2007]

$$-\frac{\partial\sigma_{\eta\eta}}{\partial\eta} - \frac{\partial\sigma_{\eta z}}{\partial z} - \frac{\sigma_{\eta\eta} - \sigma_{\theta\theta}}{\eta} = 0, \quad (2.4a)$$

$$-\frac{\partial\sigma_{\eta z}}{\partial\eta} - \frac{\partial\sigma_{zz}}{\partial z} - \frac{\sigma_{\eta z}}{\eta} = 0. \quad (2.4b)$$

Here the elastic stress $\sigma_{\alpha\beta}$ acts on a plane normal to the β direction in the direction α^\dagger . Due to the assumption of rotational symmetry no force balance for the azimuthal direction is needed.

By the assumption of local isotropy, we can model the relationship between the elastic stresses and strains using Hooke's Law:

$$\sigma_{\alpha\beta} = \delta_{\alpha\beta}\lambda_m(\varepsilon_{\eta\eta} + \varepsilon_{\theta\theta} + \varepsilon_{zz}) + 2\mu_m\varepsilon_{\alpha\beta} \quad \alpha, \beta \in \{\eta, \theta, z\}, \quad (2.5)$$

where λ_m is Lamé's first parameter, μ_m the shear modulus of the material, $\delta_{\alpha\beta}$ the Kronecker delta and $\underline{\underline{\varepsilon}}=(\varepsilon_{\alpha\beta})_{\alpha,\beta\in\{\eta,\theta,z\}}$ the strain tensor. The parameters λ_m, μ_m are

[†]These elastic stresses are symmetric, so the location of α and β in the definition can be switched.

calculated from the materials constants ν_m , the Poisson's ratio, and the bulk modulus K_m by

$$\lambda_m = \frac{3K_m\nu_m}{1 + \nu_m} \quad \text{and} \quad \mu_m = \frac{3K_m(1 - 2\nu_m)}{2(1 + \nu_m)}. \quad (2.6)$$

The strains are in turn related to the displacements in the radial and axial direction, being (u_η, u_z) , as [Chau and Wei, 2000]:

$$\begin{aligned} \varepsilon_{\eta\eta} &= \frac{\partial u_\eta}{\partial \eta}, & \varepsilon_{\theta\theta} &= \frac{u_\eta}{\eta}, \\ \varepsilon_{zz} &= \frac{\partial u_z}{\partial z}, & \varepsilon_{\eta z} &= \frac{1}{2} \left(\frac{\partial u_\eta}{\partial z} + \frac{\partial u_z}{\partial \eta} \right). \end{aligned} \quad (2.7)$$

Besides the partial differential equations defined in Equation (2.4), boundary conditions for both u_η and u_z should be defined. Let the boundary Γ of Ω consist of four regions $\Gamma_{\text{ess},\eta}$, $\Gamma_{\text{nat},\eta}$, $\Gamma_{\text{ess},z}$ and $\Gamma_{\text{nat},z}$, where ‘‘ess’’ refers to essential boundary conditions, ‘‘nat’’ to natural boundary conditions and η, z refer to the direction on which the boundary conditions act. For these sub-boundaries we have:

$$\begin{aligned} \Gamma_{\text{ess},\eta} \cup \Gamma_{\text{nat},\eta} &= \Gamma, & \Gamma_{\text{ess},z} \cup \Gamma_{\text{nat},z} &= \Gamma, \\ \Gamma_{\text{ess},\eta} \cap \Gamma_{\text{nat},\eta} &= \emptyset, & \Gamma_{\text{ess},z} \cap \Gamma_{\text{nat},z} &= \emptyset. \end{aligned} \quad (2.8)$$

Then we can define the following boundary conditions:

$$u_\eta = u_\eta^0 \quad \text{for } (\eta, z) \in \Gamma_{\text{ess},\eta}, \quad (2.9a)$$

$$\left(\underline{\underline{\sigma}} \cdot \underline{\underline{n}} \right)_\eta = f_\eta \quad \text{for } (\eta, z) \in \Gamma_{\text{nat},\eta}, \quad (2.9b)$$

$$u_z = u_z^0 \quad \text{for } (\eta, z) \in \Gamma_{\text{ess},z}, \quad (2.9c)$$

$$\left(\underline{\underline{\sigma}} \cdot \underline{\underline{n}} \right)_z = f_z \quad \text{for } (\eta, z) \in \Gamma_{\text{nat},z}, \quad (2.9d)$$

in which u_η^0, u_z^0 are predefined displacements along the essential boundaries and f_η, f_z are predefined forces along the natural boundaries.

After solving the system given by Equations (2.4) and (2.9), the elastic strain energy density Δg_s^{el} present in the system at any point is calculated, using the formula:

$$\Delta g_s^{el} = \frac{1}{2} \underline{\underline{\sigma}} : \underline{\underline{\varepsilon}}, \quad (2.10)$$

in which $:$ represents the Frobenius inner product, defined for two $n \times m$ matrices A and B as:

$$A : B = \sum_{i=1}^n \sum_{j=1}^m A_{ij} B_{ij}. \quad (2.11)$$

2.2.2 Nucleation and growth of precipitates

This section describes the models for nucleation and growth of precipitates, which is based on the model by Robson [2004]. The changes with respect to this model are discussed.

Nucleation

Robson [2004] assumes that the time-dependent homogeneous nucleation rate I , as used in Equation (2.2), is given by

$$I = N_v Z \beta^* \exp \left[-\frac{\Delta G^*}{kT} \right] \exp \left[-\frac{\tau}{t} \right], \quad (2.12)$$

where k and T represent the Boltzmann constant and the temperature, respectively. Furthermore, N_v is the number of potential homogeneous nucleation sites per unit volume, Z the Zeldovich factor, β^* the frequency of atomic attachment to a critical nucleus and τ the incubation time for homogeneous nucleation. The term ΔG^* is the free energy barrier for homogeneous nucleation which must be overcome before nucleation occurs. Using the assumption of all precipitates being spherical, the three variables Z, β^*, τ can be expressed by [Robson, 2004]:

$$Z = \frac{V_a^p \sqrt{\gamma}}{2\pi \sqrt{kT}} \left(\frac{1}{r^*} \right)^2, \quad (2.13a)$$

$$\beta^* = \frac{4\pi D x_m}{(a_p)^4} (r^*)^2, \quad (2.13b)$$

$$\tau = \frac{2}{\pi Z^2 \beta^*}. \quad (2.13c)$$

In these equations V_a^p is the atomic volume of the nucleus, r^* the critical radius of nucleation, γ the particle/matrix interface energy, D the bulk diffusion coefficient of the solute, calculated with the Arrhenius relation, x_m the atomic fraction of solute in the matrix and a_p the lattice constant of the precipitate. In this chapter solute refers to one of the chemical species within the modelled alloy, often chosen as the slowest diffusing element.

In the classical nucleation theory, the free energy change due to a homogeneous-nucleation event, ΔG , is assumed [Porter and Easterling, 1992] to be of the form

$$\Delta G = \frac{4}{3} \pi r^3 (\Delta g_v + \Delta g_s^m) + 4\pi r^2 \gamma, \quad (2.14)$$

for spherical particles, of which the derivative with respect to r is equated to zero and solved for r to find the critical radius r^* and the corresponding free energy barrier for homogeneous nucleation ΔG^* . In the above equation it is defined that Δg_v has a negative sign for an over-saturated matrix and a positive sign for an under-saturated matrix, as originally derived in Aaronson et al. [1970], and Δg_s^m has a positive sign. We adapt this equation by assuming that the free energy due to homogeneous nucleation of a precipitate with radius r is reduced due to the release of elastic strain energy due to elastic stress in the matrix. Assuming the elastic strain energy density Δg_s^{el} to be known using the model described in the previous section (see Equation (2.10)), the free energy ΔG can be described by:

$$\Delta G = \frac{4}{3} \pi r^3 (\Delta g_v + \Delta g_s^m - \Delta g_s^{el}) + 4\pi r^2 \gamma. \quad (2.15)$$

Differentiation with respect to r and equating to zero gives the modified critical radius

$$r^* = \frac{-2\gamma}{\Delta g_v + \Delta g_s^m - \Delta g_s^{el}}, \quad (2.16)$$

with the corresponding homogeneous nucleation energy barrier

$$\Delta G^* = \frac{4}{3}\pi\gamma(r^*)^2. \quad (2.17)$$

Following Aaronson et al. [1970] and assuming a dilute solution approximation, the volume free energy density can be expressed by [Dutta et al., 2001]

$$\Delta g_v = -\frac{RT}{V_m^p} \sum_{i=1}^n x_i^p \ln \left(\frac{x_i^m}{x_i^e} \right), \quad (2.18)$$

where V_m^p is the molar volume of the precipitate, x_i^p the molar fraction of element i in the precipitate, x_i^m the molar fraction of element i in the matrix, x_i^e the equilibrium molar fraction of element i in the matrix and R the gas constant and n total number of elements, including the solvent. The equilibrium molar fractions and related weight percentages are determined using a known solubility product and an equilibrium mass balance, also known as the lever rule. Note that the original derivation of Equation (2.18) by Aaronson et al. [1970] is based on a binary system. Investigation of the change in x_i^e due to an increase of the Gibbs energy of the matrix by amounts similar as in Table 2.3 and the effect on the simulations have shown that x_i^e exhibits a relative change of $2 \cdot 10^{-3}$ and the simulation results are therefore not significantly affected. Obtaining the Gibbs energy is done by the use of the TCFE6 database of ThermoCalc Software AB [2010]. We conclude that the influence of Δg_s^{el} on the value of x_m^e is negligible for the application in this research.

The misfit strain energy density Δg_s^m is given by

$$\Delta g_s^m = 3\varepsilon_m^2 \delta_p \left[1 - \left(1 + \frac{\delta_m}{\delta_p} \left(\frac{3(1-\nu_m)}{1+\nu_m} - 1 \right) \right)^{-1} \right], \quad (2.19)$$

for a coherent spherical particle, following Barnett et al. [1974]. δ_m and δ_p are constants related to the Poisson's ratios ν_m, ν_p of the matrix and the precipitate and the shear modulus of the matrix μ_m and particle μ_p :

$$\delta_m = \mu_m \frac{1+\nu_m}{1-2\nu_m}, \quad \delta_p = \mu_p \frac{1+\nu_p}{1-2\nu_p}. \quad (2.20)$$

The misfit strain ε_m represents the linear strain due to the misfit between the lattices of the matrix and precipitate if a linear interface is assumed and can be expressed as [Ratel et al., 2006]

$$\varepsilon_m = \frac{a_p - a_m}{a_m}, \quad (2.21)$$

in which a_m and a_p are the lattice parameter of the matrix and the precipitate, respectively.

On the value of N_v , the number of potential homogeneous nucleation sites per unit volume, see Equation (2.12), various theories exist. One of the earliest theories by Russell [1970] proposed to use the total number of atoms per unit volume in the matrix. Robson [2004] suggests that using the number of solute atoms per unit volume in the matrix, i.e. the value from Russell [1970] multiplied by the molar fraction of solute, gives a better agreement between predicted and measured results. Robson

[2004] also suggests using the molar fraction of solute as an empirical parameter to match predicted and measured results. Instead of using the molar fraction as an empirical parameter, we suggest the following formula for the number of potential homogeneous sites N_v

$$N_v = \frac{N_v^R x_m}{N_a^*}, \quad (2.22)$$

where N_v^R is the total number of atoms per unit volume in the matrix and N_a^* the number of atoms in a critical particle. We motivate Equation (2.22) as follows. If N_v^R is the total number of atoms per cubic meter, $N_v^R x_m$ atoms of the solute are present within the matrix. Assuming a nucleus is located at the location of one solute atom, only one out of every N_a^* atoms can form the basis of a nucleus, as each nucleus contains N_a^* atoms. This leads to Equation (2.22). The value of N_a^* is approximated by calculating the number of unit cells of the particle phase that fit within a particle with critical radius r^* and subsequently by multiplying this quantity by the number of solute atoms within a unit cell of the particle phase. During simulations the number of potential homogeneous nucleation sites N_v initially has a value in the range of 10^{25} to 10^{26} m^{-3} which decreases down to zero due to depletion of solute atoms in the matrix at the end of the simulation and causes the critical radius to become zero.

Growth

In the previous section the nucleation rate I has been discussed, which is incorporated in the source function S of Equation (2.1). The other factor influencing the time evolution of the particle distribution is the growth rate v . Following Robson [2004], we set

$$v = \frac{D}{r} \frac{C_m - C_m^r}{C_p - C_m^r}, \quad (2.23)$$

in which C_m^r is the concentration of a growth driving solute in the matrix at the particle/matrix interface, C_m the mean concentration of this solute in the matrix and C_p the concentration of the solute in the precipitate, all in weight percentages. The value of the concentration C_m^r is modelled by the application of the Gibbs-Thomson equation

$$C_m^r = C_m^e \exp\left(\frac{2\gamma V_m^p}{RT} \frac{1}{r}\right). \quad (2.24)$$

At this moment we assume that the value of the particle/matrix interface energy γ is the same for both the growth of particles as the nucleation of particles, which is in line with Robson [2004].

If we set $v(r, t)$ equal to zero and solve for the radius r , we get the no-growth radius \hat{r}

$$\hat{r} = \frac{2\gamma V_m^p}{RT} \left[\ln\left(\frac{C_m}{C_m^e}\right) \right]^{-1}. \quad (2.25)$$

We state the following proposition:

Proposition 2.1. *If the system is not in equilibrium the no-growth radius \hat{r} is only equal to the critical radius for nucleation r^* under the following assumptions:*

- 2.1. The elements within the system are considered to be of equal molar mass, or equivalent that $x_m/x_m^e=C_m/C_m^e$ holds, in Equation (2.18);
- 2.2. The precipitates consist of a single solute element, that is $x_p \equiv 1$;
- 2.3. The free energy ΔG is solely influenced by the chemical volume free energy and the interface energy.

In all other cases $\hat{r} \neq r^*$ will hold.

The proof of this proposition can be found in Appendix A.

2.3 Numerical methods

2.3.1 Elastic stress

To solve the system in Equation (2.4), we apply the basic finite-element method on these equations, adapted to the cylindrical region. After eliminating the dependency on θ due to rotation symmetry, the (η, z) -domain is discretised using linear triangles and line elements. This method consists of multiplying Equations (2.4a) and (2.4b) by v_η and v_z , respectively, which are set equal to zero on Γ_1 and on Γ_2 , respectively, and integrating by parts to minimise the order of spatial derivatives over the domain Ω .

The resulting system can be cast in the form using Newton-Cotes integration and the divergence theorem

$$\begin{bmatrix} S_{\eta\eta} & S_{\eta z} \\ S_{z\eta} & S_{zz} \end{bmatrix} \begin{bmatrix} \mathbf{u}_\eta \\ \mathbf{u}_z \end{bmatrix} = \begin{bmatrix} \mathbf{q}_\eta \\ \mathbf{q}_z \end{bmatrix}, \quad (2.26)$$

from which the values of $\mathbf{u}_\eta, \mathbf{u}_z$ can be solved. Using the same finite-element approach on the definitions of the strains, Equation (2.7), the system

$$\begin{bmatrix} \Lambda & & & \\ & \Lambda & & \\ & & \Lambda & \\ & & & \Lambda \end{bmatrix} \begin{bmatrix} \boldsymbol{\varepsilon}_{\eta\eta} \\ \boldsymbol{\varepsilon}_{\theta\theta} \\ \boldsymbol{\varepsilon}_{zz} \\ \boldsymbol{\varepsilon}_{\eta z} \end{bmatrix} = \begin{bmatrix} 2U_\eta & \\ U_\theta & \\ & 2U_z \\ U_z & U_\eta \end{bmatrix} \begin{bmatrix} \mathbf{u}_\eta \\ \mathbf{u}_z \end{bmatrix}, \quad (2.27)$$

can be derived. After solving this system, the elastic stresses can be calculated using Equation (2.5) and subsequently the elastic strain energy density Δg_s^{el} using Equation (2.10). The symbols $S_{[.]}, \mathbf{q}_{[.]}, \Lambda$ and $U_{[.]}$ are matrices which result from the application of the the finite-element method.

2.3.2 Nucleation and growth of precipitates

As mentioned in Section 2.2, the differential equation (2.1) is discretised using the first order upwind method in the particle radius domain. If a number of n_n points is chosen in the particle radius domain, let \mathbf{N} be a column vector containing the n_n unknowns, then Equation (2.1) is transformed into

$$\frac{\partial \mathbf{N}}{\partial t} = \mathbf{A}\mathbf{N} + \mathbf{S}. \quad (2.28)$$

The $n_n \times n_n$ matrix A , which is a nonlinear function of \mathbf{N} , and column vector \mathbf{S} of length n_n , which is a nonlinear function of r , t and \mathbf{N} , are defined as:

$$A_{i,i-1}(\mathbf{N}) = \frac{1}{\Delta r_i} v_{i-1/2}^+(\mathbf{N}) \quad \text{for } i = 2, \dots, n_n, \quad (2.29a)$$

$$A_{ii}(\mathbf{N}) = -\frac{1}{\Delta r_i} v_{i-1/2}^-(\mathbf{N}) - \frac{1}{\Delta r_i} v_{i+1/2}^+(\mathbf{N}) \quad \text{for } i = 1, \dots, n_n, \quad (2.29b)$$

$$A_{i,i+1}(\mathbf{N}) = \frac{1}{\Delta r_i} v_{i+1/2}^-(\mathbf{N}) \quad \text{for } i = 1, \dots, n_n - 1, \quad (2.29c)$$

$$S_i(r, t, \mathbf{N}) = S(r_i, t, \mathbf{N}) \quad \text{for } i = 1, \dots, n_n. \quad (2.29d)$$

In these equations the plus and minus signs refer, respectively, to the positive the negative part of a number. The positive part and negative part of a number a are defined as

$$a^+ = \max(a, 0), \quad a^- = -\min(a, 0). \quad (2.30)$$

In this study we use a third order time integration method from Nørsett and Thomsen [1984], similar to Robson [2004], although Robson [2004] does not specify which method is used. The method we apply is an Embedded Singly Diagonally Implicit Runge-Kutta (ESDIRK) method. This method is best described by using a Butcher tableau [see Hundsdorfer and Verwer, 2003], which can be found in Table 2.1. One time-step from t^n to t^{n+1} is performed by solving the three systems

$$\begin{aligned} \mathbf{k}_i = A \left[\mathbf{N}^n + \sum_{j=1}^{i-1} a_{ij} \Delta t \mathbf{k}_j \right] \cdot \left(\mathbf{N}^n + \sum_{j=1}^i a_{ij} \Delta t \mathbf{k}_j \right) \\ + \mathbf{S} \left[t^n + \sum_{j=2}^3 \delta_{ij} c_{j-1} \Delta t, \mathbf{N}^n + \sum_{j=1}^{i-1} a_{ij} \Delta t \mathbf{k}_j \right] \end{aligned} \quad (2.31)$$

for $i = 1, 2, 3$,

in which $A[\cdot]$ and $\mathbf{S}[\cdot, \cdot]$ are the functions as defined in Equation (2.29). The three solutions \mathbf{k}_i , $i=1, 2, 3$ are then substituted into

$$\mathbf{N}^{n+1} = \mathbf{N}^n + \sum_{i=1}^3 b_i \Delta t \mathbf{k}_i, \quad (2.32a)$$

$$\tilde{\mathbf{N}}^{n+1} = \mathbf{N}^n + \sum_{i=1}^3 e_i \Delta t \mathbf{k}_i \quad (2.32b)$$

giving a third and a fourth order accurate solution.

From the vectors \mathbf{N}^{n+1} , $\tilde{\mathbf{N}}^{n+1}$ an approximation of the local truncation error can be computed:

$$\tau^{n+1} = \|\mathbf{N}^{n+1} - \tilde{\mathbf{N}}^{n+1}\|_{\infty}. \quad (2.33)$$

This approximation is used to determine whether \mathbf{N}^{n+1} is accepted or rejected by comparison with a tolerance parameter TOL defined as:

$$\text{TOL} = \text{percentage} \cdot \|\mathbf{N}^{n+1}\|_{\infty}. \quad (2.34)$$

		a		
	$\frac{5}{6}$	$\frac{5}{6}$	0	0
c	$\frac{29}{108}$	$-\frac{61}{108}$	$\frac{5}{6}$	0
	$\frac{1}{6}$	$-\frac{23}{183}$	$-\frac{33}{61}$	$\frac{5}{6}$
	b	$\frac{25}{61}$	$\frac{36}{61}$	0
	e	$\frac{26}{61}$	$\frac{324}{671}$	$\frac{1}{11}$

Table 2.1: *Butcher tableau of the used ESDIRK-method.*

In the first case the time step is increased and we advance to the next iteration, in the latter case the size of the time step is decreased and we recompute the last iteration. This method is summarised in Algorithm 2.1. The parameters α , β , `TOL`, `maxiter` and `startvalue` are set by the user.

In this chapter we only focus on the local influence of elastic stress on the nucleation and growth of precipitates, therefore no interpolation is performed over the computational domain. If this is preferred, other models should be incorporated which describe the spatial correlations due to diffusion of cobalt through the matrix. Instead we use Algorithm 2.1 with various values as input for Δg_s^{el} which are resulting from an application of the model for elastic stress.

To combine the two models, we propose a straightforward algorithm, to compute the effect of elastic stress on the process of nucleation and growth of particles. This algorithm determines the value of the elastic strain energy density throughout the entire domain and determines a predefined set of points. Then for each point the results of the process of nucleation and growth of precipitates are computed. This computation is an altered form of Algorithm 2.1, which computes the results at the discrete times resulting from an application of Algorithm 2.1 with no elastic stress.

The above used numerical methods are mass conserving up to an accuracy of tenths of percents of the initial mass of the system independent of the parameters used in Algorithm 2.1.

2.4 Results

This section presents the results of various simulations. First we compare the results from the present model with those obtained with the model by Robson [2004] in the absence of elastic stress. Next a tension test is simulated, from which the results are used in simulations to investigate the effects of elastic stress, changes in temperature and the interfacial energy. All of the above mentioned simulations are performed on a Cu-Co system. Finally we apply the model to a hypothetical HSLA steel containing NbC precipitates.

Algorithm 2.1 *Adaptive time step algorithm.*

```

1: Set iter=1;
2: Set  $\Delta t = \text{startvalue}$ ;
3: while iter < maxiter do
4:   Compute  $N^{n+1}$ ; See Equation (2.32a).
5:   Compute  $\tilde{N}^{n+1}$ ; See Equation (2.32b).
6:   Compute  $\tau^{n+1}$ ; See Equation (2.33).
7:   if  $\tau^{n+1} > \beta \cdot \text{TOL}$  then
8:     Reject  $N^{n+1}$ ;
9:     Set  $\Delta t = \Delta t/2$ ;
10:  else if  $\tau^{n+1} > \text{TOL}$  then
11:    Accept  $N^{n+1}$ ;
12:    Set  $\Delta t = \Delta t \cdot 0.9 \cdot (\text{TOL}/\tau^{n+1})^{1/2}$ ;
13:    Set iter = iter + 1;
14:  else if  $\tau^{n+1} > \text{TOL}/\alpha$  then
15:    Accept  $N^{n+1}$ ;
16:    Set iter = iter + 1;
17:  else
18:    Accept  $N^{n+1}$ ;
19:    Set  $\Delta t = \Delta t \cdot 0.9 \cdot (\text{TOL}/\tau^{n+1}/\alpha)^{1/2}$ ;
20:    Set iter = iter + 1;
21:  end if
22: end while

```

2.4.1 Application to the Cu-Co system

Reference simulation

To investigate the influence of elastic stress on the nucleation and growth of particles, first a reference situation should be provided in which no elastic stress is assumed. As reference results we use those of Robson [2004], but computed with our model. As the model by Robson [2004] does not incorporate the misfit strain energy density, the value for the interfacial energy, 0.219 J/m², in the model by Robson [2004] is higher than the value for the interfacial energy, 0.1841 J/m², used in our model. The value of 0.219 J/m² is derived in Stowell [2002] under the assumption that no misfit occurs. This gives that the derived value of 0.219 J/m² is higher due to compensation for the neglect of misfit, where the value 0.1841 J/m² includes no compensation for misfit strain energy, as misfit is directly taken into account in the present model.

The composition of the Cu-Co system simulated is 1.02 at% Co, or equivalent 0.95 wt% Co, with the remainder Cu and the simulation was performed using a temperature of 600 °C. The percentage used in the level of tolerance, see Equation (2.34), in the use of Algorithm 2.1 is taken as 10⁻⁵, the domain of the radii simulated runs from 10⁻¹⁰ to 4.98 · 10⁻⁸ meters, divided in size classes of 2 · 10⁻¹⁰ meters. The parameters α and β of Algorithm 2.1 are taken as 2 and 1.5.

The Poisson's ratio is assumed to be independent of temperature [Rolnick, 1930], whereas the bulk modulus is modelled with temperature dependence as $K_m = K_m^0 - K_m^1 T$ [Chang and Hultgren, 1965] under the assumption that the elastic properties of

Parameter	Value	Unit	Comments
a_m^0	$3.6027 \cdot 10^{-10}$	m	Hahn [1970] Straumanis and Yu [1969]
a_m^1	$1.5788 \cdot 10^{-15}$	m/K	Hahn [1970] Straumanis and Yu [1969]
a_m^2	$1.1854 \cdot 10^{-17}$	m/K ²	Hahn [1970] Straumanis and Yu [1969]
a_m^3	$-1.1977 \cdot 10^{-20}$	m/K ³	Hahn [1970] Straumanis and Yu [1969]
a_m^4	$5.3276 \cdot 10^{-24}$	m/K ⁴	Hahn [1970] Straumanis and Yu [1969]
a_p^0	$3.5249 \cdot 10^{-10}$	m	Owen and Madoc Jones [1954]
a_p^1	$3.9540 \cdot 10^{-15}$	m/K	Owen and Madoc Jones [1954]
a_p^2	$7.2209 \cdot 10^{-19}$	m/K ²	Owen and Madoc Jones [1954]
D_0	$4.3 \cdot 10^{-5}$	m ² /s	Döhl et al. [1984]
K_m^0	$1.4652 \cdot 10^{11}$	N/m ²	Chang and Hultgren [1965]
K_m^1	$4.0243 \cdot 10^7$	N/m ² K	Chang and Hultgren [1965]
μ_p^0	$9.3486 \cdot 10^{10}$	N/m ²	Betteridge [1980]
μ_p^1	$4 \cdot 10^7$	N/m ² K	Betteridge [1980]
ν_m	0.35		Rolnick [1930]
ν_p	0.32		Betteridge [1980]
p_0^e	2.853		Servi and Turnbull [1966]
p_1^e	2.875	K	Servi and Turnbull [1966]
Q_d	$214 \cdot 10^3$	J/mol	Döhl et al. [1984]
x_p	1		Assumed

Table 2.2: *Used parameter values.*

copper are representative for the entire specimen under elastic stress. The equilibrium concentration in wt% for cobalt in copper[†] are taken from Servi and Turnbull [1966], from which x_m^e can be determined. The shear modulus μ_p is modelled with a linear temperature dependence as $\mu_p = \mu_p^0 - \mu_p^1 T$ following data from Betteridge [1980]. The lattice parameter a_p is modelled using data from Owen and Madoc Jones [1954] as $a_p = a_p^0 + a_p^1 T + a_p^2 (T)^2$ and the lattice parameter a_m is modelled by combining data from Straumanis and Yu [1969] and Hahn [1970] as $a_m = a_m^0 + a_m^1 T + a_m^2 (T)^2 + a_m^3 (T)^3 + a_m^4 (T)^4$. The values for the parameters in this system are given in Table 2.2.

To depict the behaviour of N as a function of time we have taken snapshots of this distribution at times around 10^i , $i=2, 3, 4$ seconds, as seen in Figure 2.2. The plotted frequencies $f(x)$ fulfil the requirement

$$\int_0^\infty f(x) dx = 1, \quad (2.35)$$

where x is defined as r/\bar{r} . From these figures it appears that the qualitative and quantitative behaviour of the present model and the model by Robson [2004] are close to

[†] $\log_{10} C_m^e = p_0^e - p_1^e / T \cdot 10^3$

similar at these moments. The time development of some average properties for both simulations are shown in Figure 2.3. These pictures again show the same qualitative and quantitative behaviour, from which we can conclude that the neglect of the misfit strain energy density Δg_s^m and the use of the number of potential nucleation sites N_v in the model by Robson [2004] causes a higher value of the misfit strain energy to obtain correct results. As a consequence, the incorporation of the misfit strain energy and by not using the number of potential nucleation sites as a fitting parameter in the present model predict a more reasonable value for the interfacial energy. Furthermore, the present model is less prone to fitting problems, as the number of fitting parameters is restricted to a single one, namely the interfacial energy.

Figure 2.3 also shows that the process of nucleation, growth and coarsening of precipitates for this system can be divided into three distinct periods of time. The first period runs up to about 10^2 seconds and mainly contains nucleation of new precipitates. After this nucleation period, the nucleation rate drops to zero and a period of growth is achieved, which results in an increase of the mean particle radius and a constant particle number density. Subsequently a period of coarsening is achieved, which starts at about 10^3 seconds, causing at first a constant mean particle radius, but eventually the number of small particles decreases, whereas larger particles grow. This causes the particle number density to drop and the mean particle radius to increase.

Tensile test

To investigate the performance of our proposed model under elastic stress, we simulate a uni-axial tensile test on a specimen of the ASTM Standard E8M [2001e2], page 6, as in Figure 2.4(a) with a finite-element mesh as in Figure 2.4(b). This finite-element mesh is generated using the finite-element package SEPRAN [Segal, 2010]. The specimen is assumed to be clamped on both ends over the full range. The clamps are pulled upward and downward with the same displacements, these displacements are assumed to be constant over the clamped regions. The surface of the specimen can be divided into three regions:

$$\Gamma_a = \text{Top of the specimen} \quad (2.36a)$$

$$\Gamma_b = \text{Clamped region} \quad (2.36b)$$

$$\Gamma_c = \text{Indented region.} \quad (2.36c)$$

Let the boundary Γ_d be defined as:

$$\Gamma_d = \{(\eta, z) | z = 0\}, \quad (2.36d)$$

and the boundary Γ_e be defined as:

$$\Gamma_e = \{(\eta, z) | \eta = 0\}, \quad (2.36e)$$

which arise from the symmetrical pulling upward and downward and the boundary condition from the assumption of rotation symmetry. These five boundaries are depicted in Figure 2.4(c). The essential and natural boundaries from Equation (2.9) are

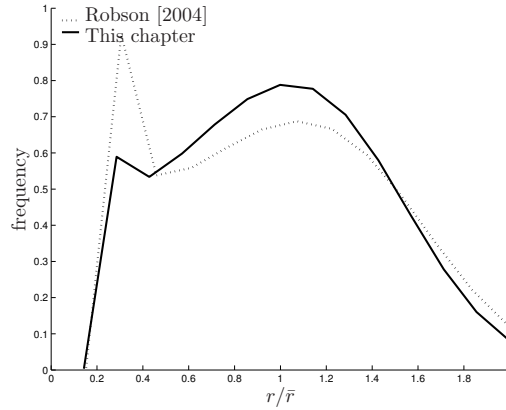
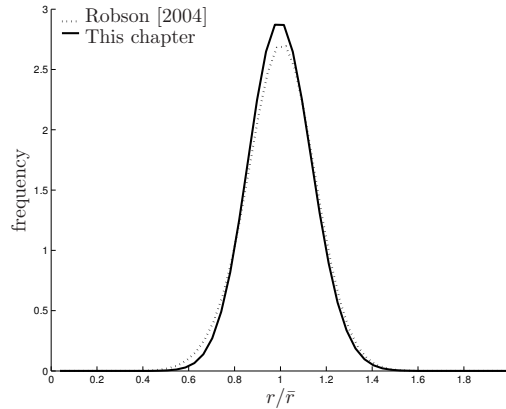
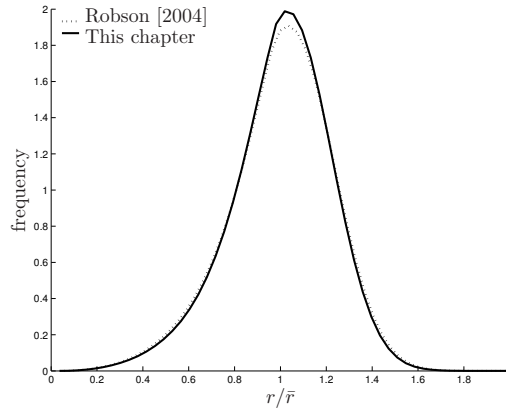
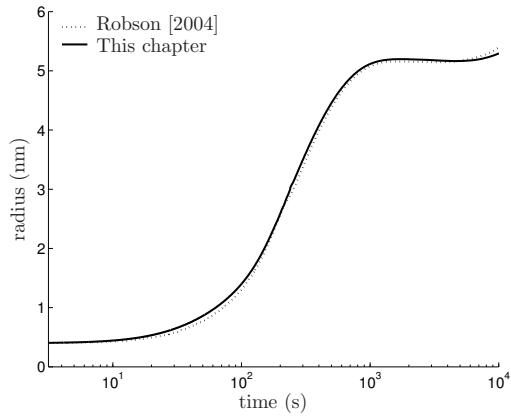
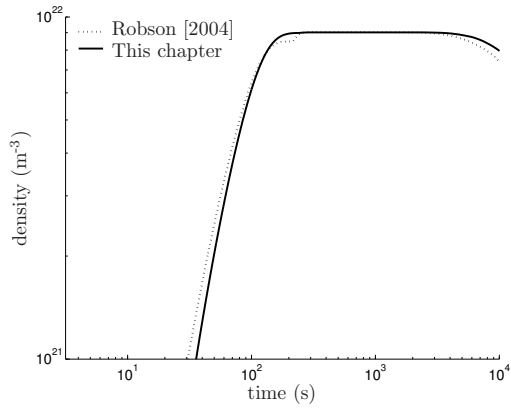
(a) $t \approx 10^2$ s, $\bar{r} \approx 1.4$ nm(b) $t \approx 10^3$ s, $\bar{r} \approx 5.1$ nm(c) $t \approx 10^4$ s, $\bar{r} \approx 5.3$ nm

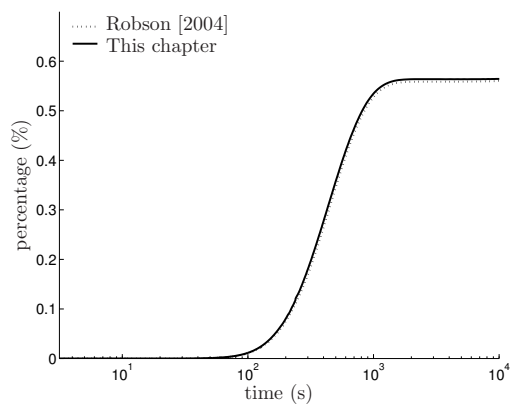
Figure 2.2: Sample particle size frequency distributions both for our model and for the model proposed by Robson [2004] for Cu-0.95 wt% Co at 600 °C.



(a) Mean particle radius.



(b) Particle number density.



(c) Particle volume fraction.

Figure 2.3: Comparison simulations for Cu-0.95 wt% Co at 600°C .

given by

$$\Gamma_{\text{ess},\eta} = \Gamma_b \cup \Gamma_e \quad (2.37a)$$

$$\Gamma_{\text{nat},\eta} = \Gamma_a \cup \Gamma_c \cup \Gamma_d \quad (2.37b)$$

$$\Gamma_{\text{ess},z} = \Gamma_b \cup \Gamma_d \quad (2.37c)$$

$$\Gamma_{\text{nat},z} = \Gamma_a \cup \Gamma_c \cup \Gamma_e. \quad (2.37d)$$

Furthermore the value of f_η is zero at $\Gamma_{\text{nat},\eta}$, f_z is zero at $\Gamma_{\text{nat},z}$. The value of u_η^* from Equation (2.9) is taken zero along $\Gamma_{\text{ess},\eta}$. The value of u_z^* is taken as zero along $\Gamma_{\text{ess},z}$, except for points belonging to Γ_b , where the value

$$u_z^* = 2 \cdot 10^{-4} \text{ m}, \quad (2.38)$$

is used, which results in Von Mises stresses below 550 MPa in the material following the Von Mises yield criterion [see Dieter, 1976, Chapter 3]. A typical set of displacements and resulting strain energy density can be seen in Figure 2.5. We stress that the resulting displacements, strains and stresses are likely beyond the elastic region of the copper-system, but they remain relevant if one considers a general mechanical energy density due to external stresses. If we assume that all elastic energy from Figure 2.5(c) is converted to energy stored in dislocations, a simple calculation shows that at most a dislocation density of 10^{15} per cubic meter is achieved. As this is a maximum, we can safely assume that the values obtained under continuous elasticity, are representative for mechanical energy due to external forces.

Influence of strain energy at a single temperature

To investigate the influence of the elastic strain energy density originating from the tensile test simulation on the model for nucleation and growth of precipitates at the constant temperature of 600 °C, the adapted form of Algorithm 2.1 is applied with the values taken as the 0th, 30th, 50th, 70th and 100th percentile[†] of the results from Figure 2.5, including the minimum and maximum of the elastic strain energy density. The grid points corresponding to these percentiles are marked in Figure 2.4(b) and the corresponding energy levels can be found in Table 2.3. The results depicting the time evolution of various variables as functions of various energy levels can be seen in Figures 2.6. These results are shown as the relative differences between the results from applying the specified amount of elastic energy and the results in the absence of elastic energy from Figure 2.3. If $f(\Delta g_s^{el}, T, \gamma)$ is a result of simulations at elastic strain energy density Δg_m^{el} , temperature T and interfacial energy γ , the relative differences for these results are defined as

$$\partial(f) = \frac{f(\Delta g_s^{el}, T, \gamma) - f(0, T, \gamma)}{f(0, T, \gamma)}. \quad (2.39)$$

From the results in Figure 2.6, we can see that the mean particle radius, the particle number density and the particle volume fraction show a clear correlation with the strain energy density as in Figure 2.5(c) and the used values in Table 2.3. We can also see that incorporating strain energy from elastic stress increases the

[†]The X^{th} percentile of a data set is defined as the value below which X percent of the data falls.

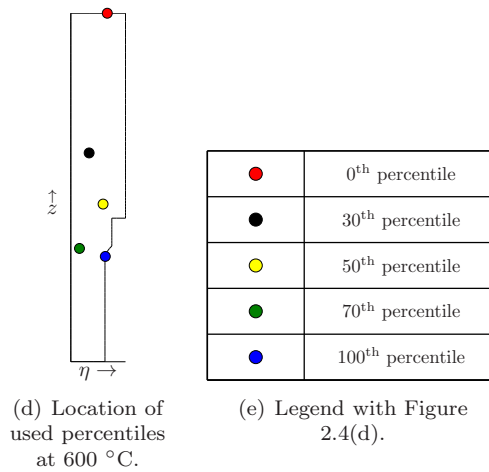
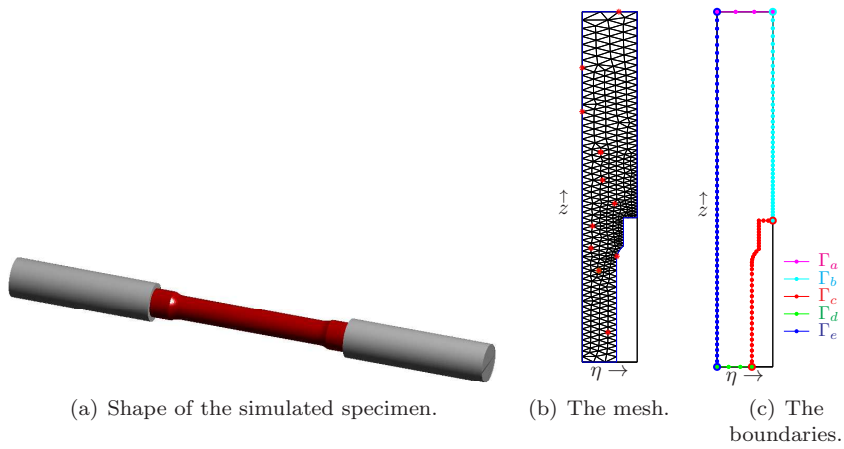


Figure 2.4: Orientation of the used finite-element mesh and corresponding elements.

Percentile	Energy density (J/m ³)
0 th	$2.5031 \cdot 10^{-4}$
30 th	$4.5796 \cdot 10^2$
50 th	$7.3062 \cdot 10^4$
70 th	$5.0720 \cdot 10^5$
100 th	$1.0734 \cdot 10^6$

Table 2.3: Used values for combined simulations.

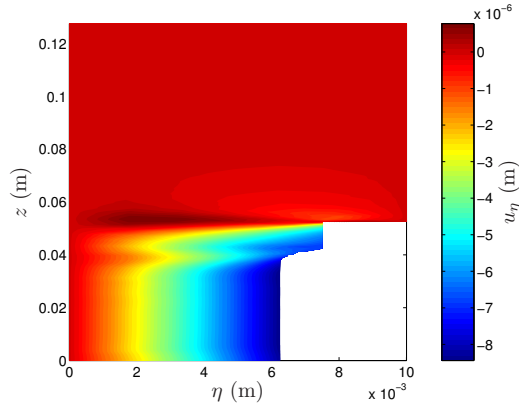
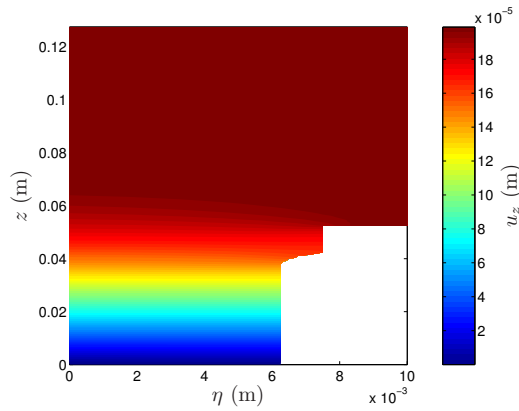
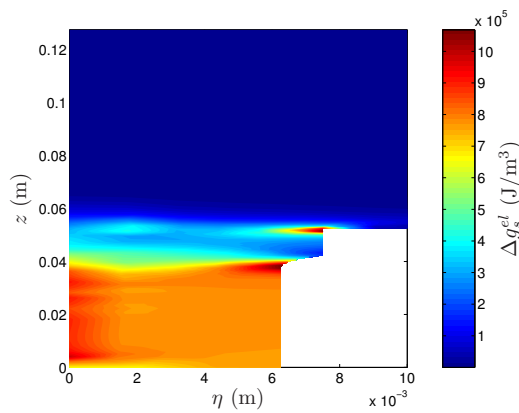
(a) Radial displacement u_η .(b) Axial displacement u_z .(c) Elastic strain energy density Δg_s^{el} .

Figure 2.5: Results of tensile test simulation of 550 MPa.

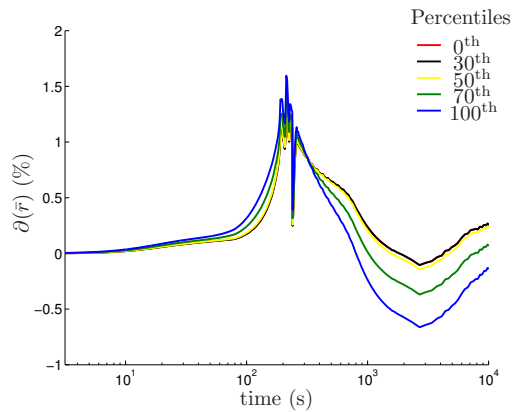
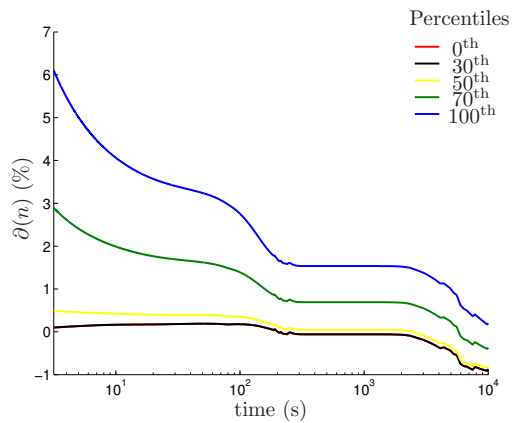
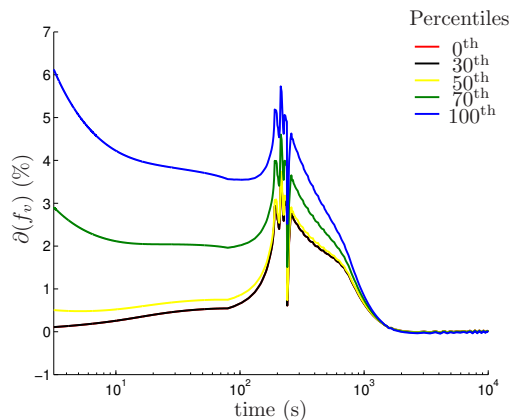
(a) Mean particle radius \bar{r} .(b) Particle number density n .(c) Particle volume fraction f_v .

Figure 2.6: Results of combined simulation. Results are percentual differences with results from absence of elastic stress. The value of the elastic strain energy density for each percentile can be found in Table 2.3.

Point	Temperature		
	575 °C	600 °C	625 °C
Min	$2.5257 \cdot 10^{-4}$	$2.5031 \cdot 10^{-4}$	$2.4805 \cdot 10^{-4}$
70 th	$5.0702 \cdot 10^5$	$5.0720 \cdot 10^5$	$4.9794 \cdot 10^5$
Max	$1.0831 \cdot 10^6$	$1.0734 \cdot 10^6$	$1.0637 \cdot 10^6$

Table 2.4: Used elastic strain energy density values (J/m^3) for temperature influence simulations.

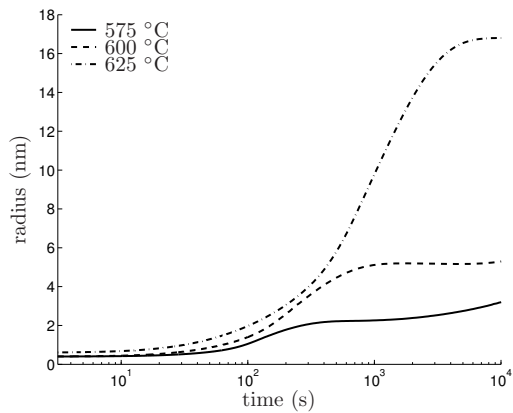
mean particle radius slightly and the particle number density significantly during the nucleation period, causing a larger particle volume fraction. This causes lower growth rates due to Equation (2.23) and as a result a decreasing mean particle radius during the growth period. Eventually the mean particle radius will increase due to coarsening of the precipitates, but will remain close to the mean particle radius in the absence of elastic stress. The influence of the incorporation of the elastic strain energy can also clearly be seen in the results from the particle number density. As this density is higher with respect to the reference results, see Figure 2.3(b), during the nucleation and growth period, at the onset of the coarsening period relatively more small precipitates will be present. This causes a quicker decrease in the number density in the coarsening period itself, with an eventual value close to the results from the reference simulation.

Influence of strain energy and temperature

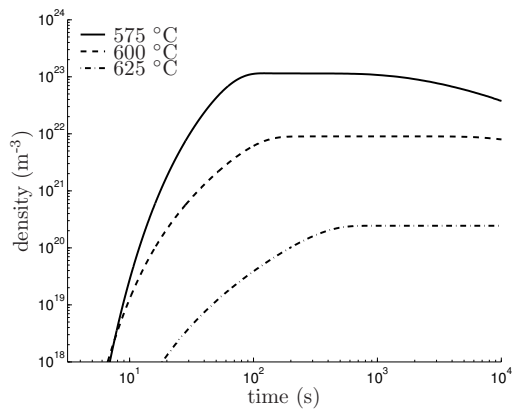
To investigate the influence of elastic strain energy at different temperatures, we first run Algorithm 2.1 at constant temperatures of 575, 600 and 625 °C, in the absence of elastic stress, using the values of all parameters as stated in Table 2.2 and previously. The results from these simulations can be seen in Figure 2.7.

From Figure 2.7, various effects of changing the temperature can be seen. The first effects are that at higher temperatures larger, but fewer precipitates are formed and the solubility of cobalt increases, as can be expected from the used exponential relationship between temperature and the equilibrium concentration of cobalt in Equation (2.24). A closer inspection of the results also shows that the length of the nucleation period and the length of the growth period increase with increasing temperature.

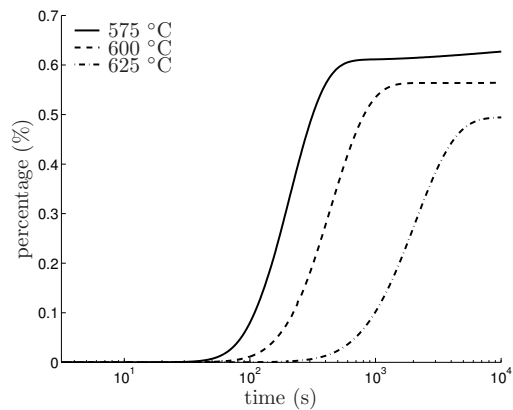
Next three points are taken from the finite-element grid as in Figure 2.4(d), for which at each temperature of the three temperatures the resulting elastic strains are calculated. These values can be found in Table 2.4. The three chosen points correspond to the minimum, the maximum and the 70th percentile of the elastic strain energy density from simulations at 600 °C. For these three points simulations are run at the three temperatures of 575, 600 and 625 °C. The results from these simulations are shown in Figure 2.8 for each temperature as the relative differences between the results from applying the specified amount of elastic energy and the results in the absence of elastic energy from Figure 2.7 at that temperature in percentages. The relative differences are defined as in Equation (2.39).



(a) Mean particle radius.



(b) Particle number density.



(c) Particle volume fraction.

Figure 2.7: Result of simulations for Cu-0.95 wt% Co at 575, 600 and 625 °C.

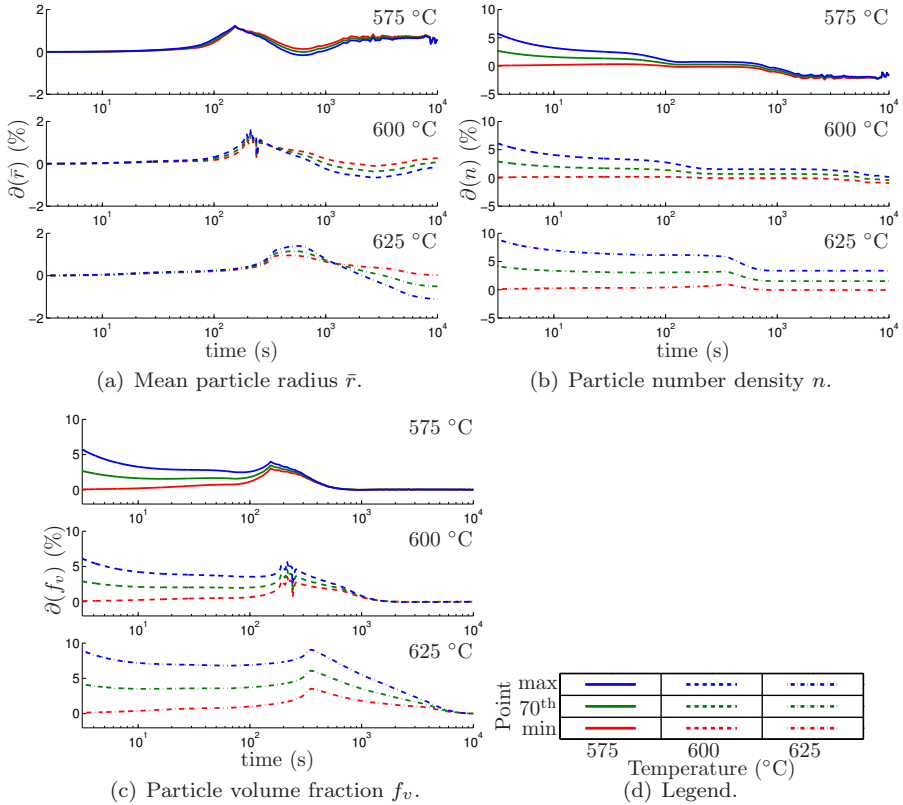


Figure 2.8: Result of simulations for Cu-0.95 wt% Co at 575, 600 and 625 °C for the elastic strain energy densities from Table 2.4.

The results in Figure 2.8 show that for each simulated temperature again the relative differences of the mean particle radius, particle number density and the particle volume fraction are closely related to the magnitude of the used elastic strain energy density. With respect to the dependency of the results on the temperature, we see that at each temperature the same qualitative behaviour is observed, but with a shift in the temporal domain. This shift can be explained by comparing the results in Figure 2.7 with those in Figure 2.8. From the particle number density we see for on increasing temperature a later start of the growth period and a longer growth period (Fig. 2.7(a)), which can also be seen in Figure 2.8 as a shift in the characteristics of the relative differences for each variable shown. Figure 2.8 shows that with increasing temperature the relative differences due to the elastic strain energy densities increases. We can conclude that the main differences between the results at various temperatures are mostly caused by changes in the behaviour of the system due to the temperature itself, although a slight increased effect of incorporating the elastic strain energy can be seen at higher temperatures.

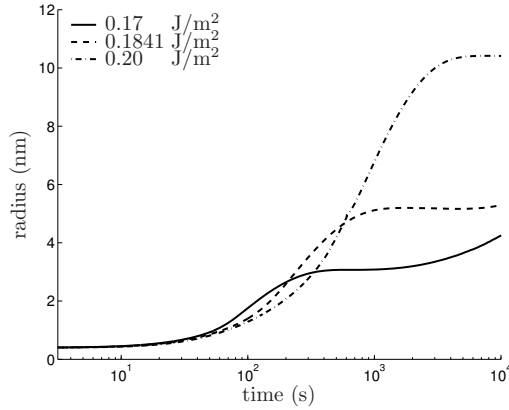
Influence of strain energy and interface energy

To investigate the influence of elastic strain energy at different values of the interface energy γ , we first run Algorithm 2.1 at a constant temperature of 600 °C with the fitted value of 0.1841 J/m² and the values of 0.17 and 0.20 J/m², in the absence of elastic stress, using the values of all other parameters as stated in Table 2.2 and previously. The results from these simulations can be seen in Figure 2.9.

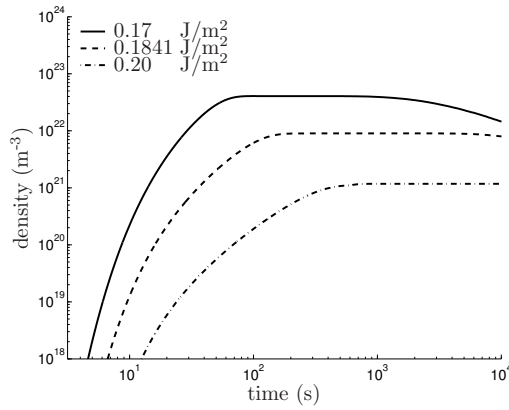
Although the results for different values of the interface energy (Figure 2.9) are similar in nature to the values obtained for multiple temperatures (Figure 2.7), at some points differences occur. One of these differences is the fact that increasing the interface energy does not influence the solubility. Hence the growth period remains the same, although the growth rates should be influenced by an increased interface energy. On inspection of the growth rates and its dependency on the interface energy, only a large positive influence of the growth rate is seen for small precipitates. As the system predicts on average larger precipitates due to an increase in interface energy, these higher growth rates are negligible.

Subsequently three points are taken from the finite-element grid as in Figure 2.4(d), for which the resulting elastic strains can be found in Table 2.3. The three chosen points correspond to the minimum, the maximum and the 70th percentile of the elastic strain energy density from the simulations at 600 °C. For these three points, simulations are performed with the values of 0.1841 J/m² and the values of 0.17 and 0.20 J/m² for the interface energy. The results from these simulations are shown in Figure 2.10 for each value of the interface energy as the relative differences between the results from applying the specified amount of elastic energy and the results in the absence of elastic energy from Figure 2.9 at that value of the interface energy. The relative differences are defined as in Equation (2.39).

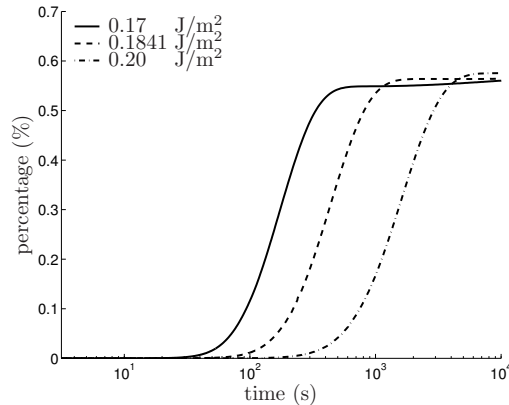
Similar to the results in Figure 2.8 for the various temperatures, the results in Figure 2.10 show a clear correlation with the value of the interface energy. The shift of the qualitative behaviour in the temporal domain is again present, and coincides with the effects of changing the value of the interface energy in the absence of elastic stress. We can conclude that the main differences between the results at various values



(a) Mean particle radius.



(b) Particle number density.



(c) Particle volume fraction.

Figure 2.9: Results of simulations for Cu-0.95 wt% Co at 600 °C with values of 0.17, 0.1841 and 0.20 J/m² for the interface energy.

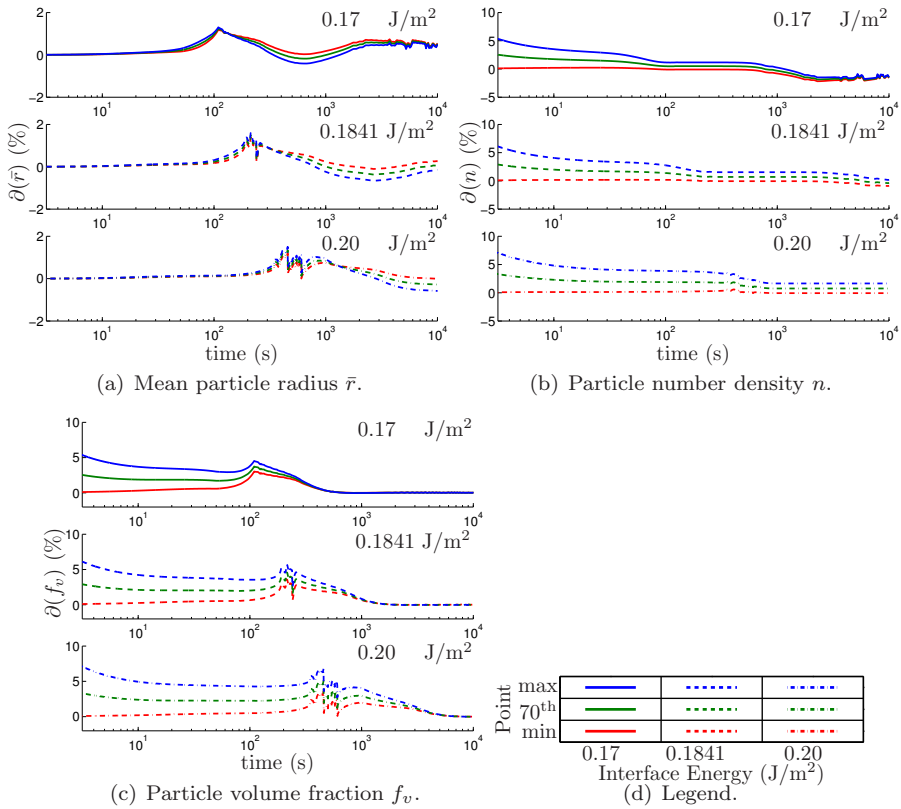


Figure 2.10: Results of simulations for Cu-0.95 wt% Co at 600 °C for three of the elastic strain energy densities from Table 2.3 with values of 0.17, 0.1841 and 0.20 J/m^2 for the interface energy.

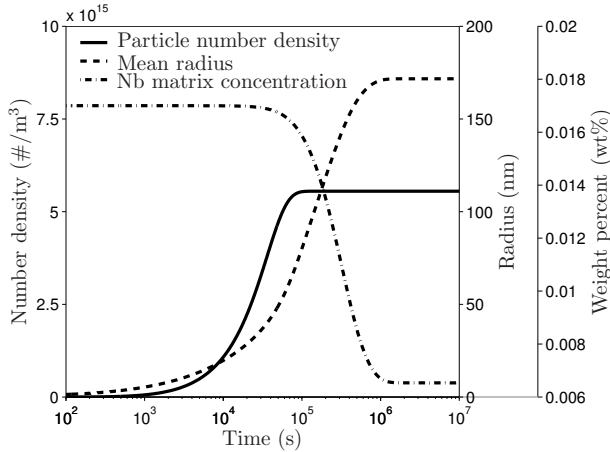


Figure 2.11: Particle number density, mean radius and Nb-concentration in the matrix as function of time at zero stress.

of the interface energy are mostly caused by changes in the behaviour of the system due to the interface energy itself, although a slight increased effect of incorporating the elastic strain energy can be seen at higher values of the interface energy.

2.4.2 Application to a hypothetical HSLA steel

The above derived model is applied using standard available numerical methods to a hypothetical HSLA steel containing 0.017Nb, 0.06C and 0.25Mn (in wt%). It has been held at 1250 degrees Celsius for a long period of time to obtain a fully austenitic structure and then fast cooled to 950 degrees Celsius, at which the simulations start. It is assumed that only NbC precipitates can occur, no precipitates are initially present and Nb is the element driving growth of precipitates. Furthermore it is assumed that the interface energy γ has a value of 0.15 J/m². For the solubility product that we needed to obtain the equilibrium concentrations and the diffusivity of Nb in austenite we follow Dutta et al. [2001] giving

$$\log_{10} C_{Nb}^e C_C^e = 2.06 - \frac{6700}{T} \quad \text{and} \quad D_{Nb} = 1.4 \cdot 10^{-4} \exp\left(-\frac{270 \cdot 10^3}{RT}\right). \quad (2.40)$$

We also assume no misfit occurs between precipitate and matrix.

Figure 2.11 gives some results of the model when applied to the HSLA steel prior to deformation. These results show that initially small precipitates nucleate with an increasing nucleation rate, causing a rapid increase in the particle number density. The nucleated precipitates grow immediately after nucleation, causing a simultaneous increase in mean particle radius. After about $8 \cdot 10^4$ seconds the nucleation rate drops to almost zero, causing a stabilisation of the particle number density. As the system has not attained an equilibrium, which can be seen from the values of the Nb matrix concentration, the present precipitates will start to coarsen until the equilibrium is almost achieved. At this moment the Nb matrix concentration is close to the equilibrium value of 0.0065 wt%.

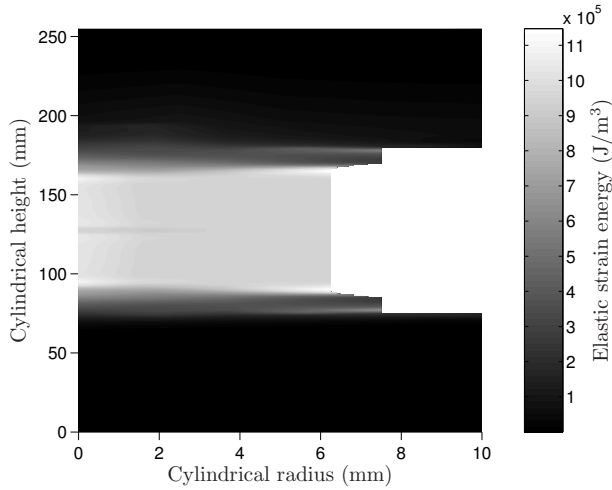


Figure 2.12: *Simulated elastic strain energy distribution on a cylindrical specimen during simulations.*

Figure 2.12 shows a typical elastic strain energy density distribution in a ASTM standard specimen following page 6 from ASTM Standard E8M [2001e2] during a tensile test. Simulating the nucleation and growth in the mentioned HSLA under deformation, the results in Figures 2.13, 2.14 and 2.15 are obtained. These results depict the results under elastic stress as percent differences with the results in Figure 2.11 at various moments during simulation. We interpolated the results from application of the model at several values of the strain energy spatially, ignoring any influence of diffusion through the specimen.

The results indicate that the introduction of elastic strain energy as proposed in the model causes a significant increase in the particle number density throughout the simulation with a clear spatial correlation with Figure 2.12. From Figure 2.14, we can derive that during the initial stages of the model larger particles nucleate with respect to the results without deformation, thereby increasing the mean particle radius. As soon as the particle number density stabilises, the precipitates will start to grow. Due to the higher particle number density with respect to the undeformed system, less niobium is present in the matrix to facilitate coarsening. This indicates that the precipitates can not become as large as in the undeformed system, causing a relative lower increase in the mean radius, which in turn leads to a relative lower mean radius. Due to the correlation between the particle number density (Fig. 2.13) and the strain energy (Fig. 2.12), the mean radius also shows a clear correlation with Figure 2.12. The results for both the mean particle radius and the particle number density indicate that the concentration of niobium in the matrix should be lower at the initial stages of the model, but this should eventually cancel out as the equilibrium is attained, which can be seen back in Figure 2.15.

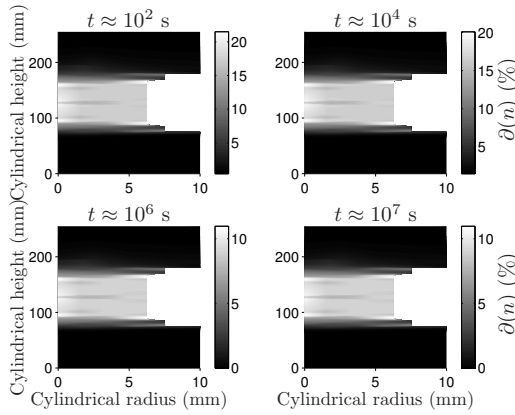


Figure 2.13: *Relative differences of the local particle number density n at zero and near 550 MPa stress.*

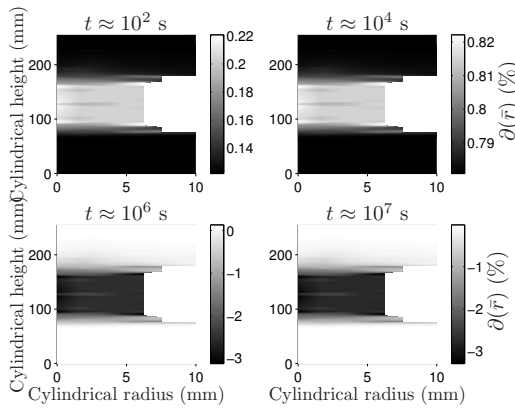


Figure 2.14: *Relative differences of the local mean particle radius \bar{r} at zero and near 550 MPa stress.*

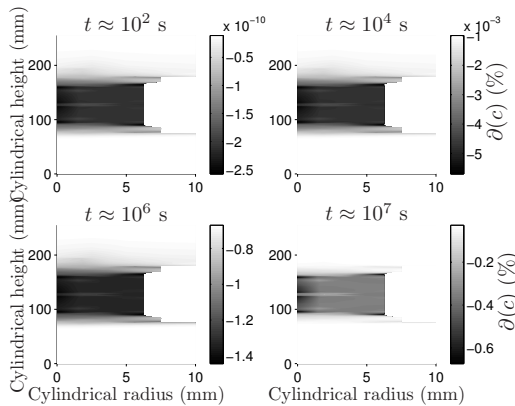


Figure 2.15: *Relative differences of the local Nb concentration c in the matrix at zero and near 550 MPa stress.*

2.5 Conclusions

In this chapter we have combined a model for the nucleation and growth of particles in a binary alloy with elastic stress from a uni-axial tensile test. This model has been implemented using both finite-volume and finite-element methods. The simulation concerns a binary copper-cobalt alloy at fixed temperatures during a hypothetical uni-axial tensile test. The results from the simulations show that incorporation of strain energy due to elastic stress slightly promotes the nucleation of precipitates with an initially larger mean radius, but an eventual smaller mean particle radius due to faster depletion of the matrix. The results from simulations at different temperatures and different values of the interface energy, show that the influence of elastic stress on the process of nucleation and growth of precipitates is mainly restricted to a quantitative effect, where the effect increases with increasing values of the elastic strain energy density. These results also show that both a higher (lower) temperature and interface energy cause larger (smaller) and more (less) precipitates during the initial stages of the process. The effect of a higher (lower) temperature will remain during the entire process as the solubility changes, where the effect of a higher (lower) interface energy decays as the solubility does not change.

We also simulated the effect of external elastic stress on the nucleation and growth of homogeneous NbC precipitates in an HSLA steel. The simulations show a successful introduction of the external elastic strain energy in the KWN-model and that this introduction can lead to significantly more and slightly larger NbC precipitates at the start of the process. During the process the number density remains higher, whereas the average size of the precipitates eventually becomes smaller in comparison with simulations ignoring the external elastic strain energy.

Bibliography

- H.I. Aaronson, K.R. Kinsman and K.C. Russel. The volume free energy change associated with precipitate nucleation. Scripta Metallurgica, 4(2):101–106, 1970.
- ASTM Standard E8M. Standard Test Methods for Tension Testing of Metallic Materials [Metric]. ASTM International, West Conshohocken, PA, United States of America, 2001e2.
- D.M. Barnett, J.K. Lee, H.I. Aaronson and G.F. Batalha. The strain energy of a coherent ellipsoidal precipitate. Scripta Metallurgica, 8(12):1447–1450, 1974.
- W. Betteridge. The properties of metallic cobalt. Progress in Materials Science, 24: 51–142, 1980.
- Y.A. Chang and R. Hultgren. The Dilation Contribution to the Heat Capacity of Copper and α -Brass at Elevated Temperatures. The Journal of Physical Chemistry, 69(12):4162–4165, 1965.
- K.T. Chau and X.X. Wei. Finite solid circular cylinders subjected to arbitrary surface load. part I – analytic solution. International Journal of Solids and Structures, 37 (40):5707–5732, 2000.

- G.E. Dieter. Mechanical metallurgy. McGraw-Hill, New York, NY, United States of America, 3rd edition, 1976.
- R. Döhl, M.-P. Macht and V. Naundorf. Measurement of the Diffusion Coefficient of Cobalt in Copper. Physica Status Solidi (a), 86:603–612, 1984.
- B. Dutta, J. Palmiere and C.M. Sellars. Modelling the kinetics of strain induced precipitation in Nb microalloyed steels. Acta Materialia, 49:785–794, 2001.
- T.A. Hahn. Thermal Expansion of Copper from 20 to 800 K – Standard Reference Material 736. Journal of Applied Physics, 41(13):5096–5101, 1970.
- W. Hundsdorfer and J.G. Verwer. Numerical Solution of Time-Dependent Advection-Diffusion-Reaction Equations, volume 33 of Springer Series in Computational Mathematics. Springer-Verlag, Berlin, Germany, 2003.
- J.C. Jaeger, N.G.W. Cook and R.W. Zimmerman. Fundamentals of rock mechanics. Wiley, Blackwell, United Kingdom of Great Britain and Northern Ireland, 2007.
- O.R. Myhr and Ø. Grong. Modelling of non-isothermal transformations in alloys containing a particle distribution. Acta Materialia, 48(7):1605–1615, 2000.
- S.P. Nørsett and P.G. Thomsen. Embedded SDIRK-methods of basic order three. BIT, 24:634–646, 1984.
- E.A. Owen and D. Madoc Jones. Effect of Grain Size on the Crystal Structure of Cobalt. Proceedings of the Physical Society. Section B, 67:456–466, 1954.
- D.A. Porter and K.E. Easterling. Phase Transformations in Metals and Alloys. Chapman & Hall, London, United Kingdom of Great Britain and Northern Ireland, 2nd edition, 1992.
- N. Ratel, G. Bruno, P. Bastie and T. Mori. Plastic strain-induced rafting of γ' precipitates in Ni superalloys: Elasticity analysis. Acta Materialia, 54(19):5087–5093, 2006.
- J.D. Robson. Modelling the evolution of particle size distribution during nucleation, growth and coarsening. Materials Science and Technology, 20:441–448, 2004.
- H. Rolnick. Tension Coefficient of Resistance of Metals. Physical Review, 36(3): 506–512, 1930.
- K.C. Russell. Phase transformations, page 219. American Society for Metals, Materials Park, OH, United States of America, 1970.
- G. Segal. SEPRAN manuals. Den Haag, The Netherlands, 2010.
- I.S. Servi and D. Turnbull. Thermodynamics and kinetics of precipitation in the copper-cobalt system. Acta Metallurgica, 14:161–169, 1966.
- M.J. Stowell. Precipitate nucleation: does capillarity theory work? Materials Science and Technology, 18:139–144, 2002.

M. E. Straumanis and L. S. Yu. Lattice parameters, densities, expansion coefficients and perfection of structure of Cu and of Cu-In α phase. Acta Crystallographica Section A, 25(6):676–682, 1969.

Thermo-Calc Software AB. TCS Steel and Fe-alloys Database, 2010. URL http://www.thermocalc.com/res/pdfDBD/DBD_TCFE6.pdf.

Chapter 3

The multi-component, multi-phase KWN-model

With an application to an HSLA steel

3.1 Introduction

The present chapter presents a novel extension of the Kampmann-Wagner-Numerical (KWN) model for nucleation and growth of precipitates by Robson's formalism [Robson, 2004], which incorporates multi-component precipitates of several secondary phases. This goal is achieved by extending the equations proposed by Robson [2004] such that they account for the presence of multiple elements and precipitates with varying stoichiometry. A new model for the frequency of the atomic attachment to a growing particle using Continuous-Time Markov-Chains is introduced. Furthermore a multi-component growth rate description is proposed. We remark that the present chapter has a theoretical and computational nature. Therefore, an experimental validation is not available at this stage, despite its importance on the longer term.

In the present chapter we describe the model for the nucleation and growth of precipitates. Subsequently, the model is discretised using finite-volume methods. The model and its new features are demonstrated and compared to other models by an application to an HSLA alloy.

This chapter is based on the article:

D. den Ouden, L. Zhao, C. Vuik, J. Sietsma and F.J. Vermolen. Modelling precipitate nucleation and growth with multiple precipitate species under isothermal conditions: Formulation and analysis. *Computational Materials Science*, 79:933–943, 2013b,

and additional work.

3.2 The model for multiple precipitate types, multiple elements

Nucleation and growth of precipitates can be modelled by the KWN model Robson [2004], which in the present chapter is extended in such a manner that all equations are based on the assumption that multiple elements influence the nucleation and growth of precipitates. The main features of the standard KWN model are:

- All precipitates are spherical and classified by their radius in meters (m).
- The number balance of the model is described by the partial differential equation due to Hulburt and Katz [1964], Samaras [2006]:

$$\frac{\partial \phi}{\partial t} = -\frac{\partial [v\phi]}{\partial r} + S, \quad (3.1)$$

in which $\phi \equiv \phi(r, t)$ in m^{-4} denotes the number density distribution of precipitates with radius r and at time t , $v \equiv v(r, t)$ in ms^{-1} represents the growth rate of precipitates with radius r and at time t . Further $S \equiv S(r, t)$ in $\text{m}^{-4}\text{s}^{-1}$ is a source function representing nucleation for the number density distribution of newly appearing precipitates with radius r at time t .

- The value of the source function S is calculated from classical nucleation theory (CNT) and is given by [Hulburt and Katz, 1964, Samaras, 2006],

$$S(r, t) = \delta(r - r^*(t))I(t). \quad (3.2)$$

Here $I(t)$ is the nucleation rate of the precipitates following from CNT, $r^*(t)$ the critical radius following from CNT and δ the Dirac delta function.

- The first-order upwind method, LeVeque [2002], is applied to Equation (3.1), combined with a time integration method [Hundsdoerfer and Verwer, 2003].

Note that the partial differential equation given in Myhr and Grong [2000], who were the first to apply the KWN-model to aluminium alloys, is given for the integrated quantity $N(r, t)$, where N represents the number density of precipitates with radius between $r - \Delta r/2$ and $r + \Delta r/2$ at time t . Myhr and Grong [2000] express the relation between N and ϕ as

$$N(r, t) = \phi(r, t)\Delta r, \quad (3.3)$$

with r being taken from a set of discrete points within the range $[0, \infty)$. The right-hand side of Equation (3.3) is an approximation to the integral

$$N(r, t) = \int_{r-\Delta r/2}^{r+\Delta r/2} \phi(\tilde{r}, t) d\tilde{r}. \quad (3.4)$$

Using Equation (3.3), N remains a discrete quantity, whereas ϕ remains continuous. This is why we have chosen to use Equation (3.1), which is more accurate than the partial differential equation in Myhr and Grong [2000]. The use of Equation (3.1) in combination with the source function in Equation (3.2) furthermore has the benefit that no artificial interval has to be defined in which the nucleating precipitates are added.

3.2.1 Extension to multiple precipitate types

In any steel, magnesium or aluminium alloy, various types of precipitates can occur (See for example Dijk et al. [2002]). Consider a set of precipitate types \mathbb{P} , where $p \in \mathbb{P}$ stands for a type of precipitate that can occur in a specific alloy. The classification of precipitate types is based on the (stoichiometric) precipitate compositions. Furthermore, let \mathbb{E} be the set of elements within the alloy, where $e \in \mathbb{E}$ denotes a chemical element that occurs within the alloy. Then we can define the following quantities:

Nominal concentration: The nominal concentration of an element does not depend on a precipitate type, we denote the nominal mole fraction for each element $e \in \mathbb{E}$ by $x_{0,e}$.

Mean concentration within the matrix: As the mean concentration of an element within the matrix depends on all precipitate types, we denote the mean mole fraction for each element $e \in \mathbb{E}$ by $x_{m,e}$.

Concentration within a precipitate: Within a single precipitate of type $p \in \mathbb{P}$, for each element $e \in \mathbb{E}$, $x_{p,e}$ denotes the mole fraction within the precipitate of type $p \in \mathbb{P}$. The related stoichiometric composition within the precipitate of type $p \in \mathbb{P}$ is denoted by $n_{p,e}$ for each element $e \in \mathbb{E}$. We stress that $x_{p,e}$ is assumed to be constant in time and position within a precipitate.

We assume that each precipitate of type $p \in \mathbb{P}$ is spherical and that it has a number density distribution $\phi_p(r, t)$. Therefore we have for each precipitate type $p \in \mathbb{P}$ a specific form of Equation (3.1):

$$\frac{\partial \phi_p}{\partial t} = -\frac{\partial [v_p \phi_p]}{\partial r} + S_p, \quad (3.5)$$

where S_p is a source function defined as:

$$S_p(r, t) = \delta(r - r_p^*(t)) I_p(t). \quad (3.6)$$

In the above equations the subscript p refers to the precipitate type p . The critical radius r_p^* and nucleation rate I_p will be defined in Section 3.2.2 and the growth rates v_p will be defined in Section 3.2.3.

3.2.2 Nucleation of precipitates

Following Robson [2004], we assume that the time-dependent nucleation rate I_p for precipitates of type $p \in \mathbb{P}$, as used in Equation (3.6), is given by

$$I_p = N_{v,p} Z_p \beta_p^* \exp \left[-\frac{\Delta G_p^*}{k_B T} \right] \exp \left[-\frac{\tau_p}{t} \right], \quad (3.7)$$

where k_B and T represent the Boltzmann constant and temperature. Furthermore, $N_{v,p}$ is the number density of potential nucleation sites for precipitate type p , Z_p the Zeldovich factor, β_p^* the frequency of atomic attachment to a growing precipitate and τ_p the incubation time for precipitation, all for precipitate type p . The term ΔG_p^* is

the free-energy barrier for nucleation which must be overcome before precipitation of type p occurs. The variable Z_p can be expressed by

$$Z_p = \frac{V_p^a \sqrt{\gamma_p}}{2\pi\sqrt{k_B T}} \left(\frac{1}{r_p^*} \right)^2, \quad (3.8)$$

which agrees with the equation given in Russell [1980] for spherical precipitates. In these equations V_p^a is the atomic volume of the precipitate type p , r_p^* the critical radius of precipitate type p and γ_p the effective precipitate/matrix interface energy for precipitate type p . The incubation time τ_p is given by [Russell, 1980]

$$\tau_p = \frac{1}{2Z_p^2\beta_p^*}. \quad (3.9)$$

In the classical nucleation theory, the free-energy change due to a nucleation event of an incoherent spherical precipitate of type p , ΔG_p , is assumed [Porter and Easterling, 1992] to be of the form

$$\Delta G_p = \frac{4}{3}\pi r^3 \Delta g_{v,p} + 4\pi r^2 \gamma_p. \quad (3.10)$$

In this equation, $\Delta g_{v,p}$ is the chemical free-energy change upon precipitation of precipitate type p , which has negative sign if the matrix is oversaturated. Differentiation with respect to r and equating to zero gives the critical radius

$$r_p^* = \frac{-2\gamma_p}{\Delta g_{v,p}}, \quad (3.11)$$

with the corresponding nucleation energy barrier

$$\Delta G_p^* = \frac{4}{3}\pi\gamma_p(r_p^*)^2. \quad (3.12)$$

Following Aaronson et al. [1970] and assuming a dilute solution approximation, the chemical free-energy change upon nucleation of precipitate type p can be expressed by Dutta et al. [2001]

$$\Delta g_{v,p} = -\frac{R_g T}{V_p^{\text{mole}}} \sum_{e \in \mathbb{E}_p} x_{p,e} \ln \left(\frac{x_{m,e}^{p/m}}{x_{m,e}^{p/m}} \right), \quad (3.13)$$

where V_p^{mole} is the molar volume of the precipitate, $x_{p,e}$ the mole fraction of element e in the precipitate, $x_{m,e}^{p/m}$ the equilibrium mole fraction of element e in the matrix at the precipitate/matrix interface and R_g the gas constant. Further, $\mathbb{E}_p \subset \mathbb{E}$ denotes the set of all chemical elements that are present in precipitate type p , that is:

$$\mathbb{E}_p = \{e \in \mathbb{E} | x_{p,e} > 0\}. \quad (3.14)$$

Appendix B shows the physical background of Equation (3.13), which is based on the original derivation in Aaronson et al. [1970] for binary systems. The mole fractions $x_{m,e}^{p/m}$ can be derived from the molar solubility product

$$\mathcal{K}_p(T) = \prod_{e \in \mathbb{E}_p} \left(x_{m,e}^{p/m} \right)^{x_{p,e}}, \quad (3.15)$$

which, in turn, is related to the commonly used solubility product

$$\mathcal{K}_p^w(T) = \prod_{e \in \mathbb{E}_p} [e]^{n_{p,e}}, \quad (3.16)$$

with $[e]$ the weight percent of element e in the matrix at equilibrium.

With respect to the value of $N_{v,p}$, the number density of potential nucleation sites for an incoherent precipitate type p , see Equation (3.7), various theories exist. One of the earliest theories by Russell [1970], uses the total number of atoms per unit volume in the matrix. In Robson [2004] it is suggested to use the number of solute atoms per unit volume in the matrix, i.e. the value from Russell [1970] multiplied by the mean mole fraction of solute in the matrix. The latter approach gives a better agreement between simulations and experiments [Robson, 2004]. In Robson [2004] it is also suggested to replace the mole fraction of solute with an empirical parameter to match predicted and measured results. Within the computational software MatCalc [2012], the number of substitutional atomic sites is used for the number density of potential nucleation sites, which is approximated by the number of substitutional sites within a matrix unit lattice cell divided by the volume of the matrix unit lattice cell. As we agree with the argument that a precipitate can nucleate at any substitutional site in the matrix lattice, we adopt the definition from MatCalc [2012].

The factor β^* is introduced by Robson [2004] as the frequency of atomic attachment to a growing precipitate for a binary alloy with a precipitate containing a single element using the equation

$$\beta^* = \frac{4\pi D x_m}{a_m^4} (r^*)^2, \quad (3.17)$$

where D equals the bulk diffusion coefficient of the element, x_m the atomic fraction of that element in the matrix and a_m the lattice constant of the matrix. The CNT is based on the principals of nucleation theory of liquid droplets forming from a gas solution, which defines β^* as the product of the area of a spherical nucleating droplet at critical radius r_p^* and the attachment frequency of a molecule per unit area of the droplet [Russell, 1980]. Based on this original definition, β_p^* for a spherical precipitate type p , has the form

$$\beta_p^* = 4\pi (r_p^*)^2 \lambda_p^a, \quad (3.18)$$

with λ_p^a the effective attachment frequency of a structural unit of precipitate type p per unit area. Assuming the effective attachment frequency of a precipitate structural unit to be given by λ_p^m , β_p^* can be reshaped to

$$\beta_p^* = \frac{4\pi (r_p^*)^2}{a_p^2} \lambda_p^m. \quad (3.19)$$

To be able to evaluate the latter equation, we need a definition for the effective frequency λ_p^m .

A first approach that often is employed, is to apply Equation (3.17) to the slowest diffusing element, indicating that λ_p^m is defined as

$$\lambda_p^m = \frac{D_f x_{m,f}}{a_m^2}, \quad (3.20)$$

where $f \in \mathbb{E}_p$ such that

$$D_f = \min_{e \in \mathbb{E}_p} D_e. \quad (3.21)$$

In Svoboda et al. [2004], a different approach is taken, in which λ_p^m is defined as

$$\lambda_p^m = \frac{1}{a_m^2 \Omega} \left[\sum_{e \in \mathbb{E}_p} \frac{(c_{ke} - c_{0e})^2}{c_{0e} D_e} \right]^{-1}, \quad (3.22)$$

where the c_{ke} and c_{0e} are concentrations and Ω is the partial molar volume[†]. This approach is based on the solution of their evolution equations dealing with the thermodynamic extremum principle (see Onsager [1931a,b]) and with the comparison of a dilute binary system with a unary precipitate to a multi-component system with a multi-component precipitate.

In the present chapter, we take an atomistic approach, which will reduce to Equation (3.17) for a binary system with a unary precipitate. Consider a precipitate type p which contains n elements, of which the first s elements are located on the substitutional lattice of the precipitate and the last $n - s$ elements are located on the interstitial lattice of the precipitate. We further assume that the ratio between substitutional and interstitial positions within the precipitate lattice equals one. To create an atomic unit on the surface of the precipitate, one atom of the substitutional set and one atom of the interstitial set should jump from their position in the matrix lattice to their position on the precipitate lattice. The presence of an atom of element e at a precipitate lattice position can be described by the state variable χ_e , which is given by

$$\chi_e = \begin{cases} 0 & \text{if atom type } e \text{ is not present,} \\ 1 & \text{if atom type } e \text{ is present,} \end{cases} \quad (3.23)$$

for $e = 1, \dots, n$. These variables are captured in the state vector

$$\chi = (\chi_1, \dots, \chi_s | \chi_{s+1}, \dots, \chi_n), \quad (3.24)$$

which can assume up to 2^n different values. We further assume that at any time, the presence of a single element type e can change, but not simultaneously with the change of another element type. This indicates that if the state χ of the system changes, only one χ_e changes from 0 to 1 or vice versa. If one of the s substitutional elements is present at a precipitate lattice position and simultaneously one of the $n - s$ interstitial elements is present at a precipitate lattice position, we assume that strong bonds are established and that both atoms cannot jump back to the matrix, and so the current state cannot be altered. It follows that χ can only assume $\mathbb{S} = (s + 1)(n - s + 1)$ different values under these assumptions.

To model the change in the state χ , we assign to each element type e a change of energy ΔU_e when χ_e changes from 0 to 1:

$$\Delta U_e = x_{p,e} \Delta g_{v,p} V_p^{\text{mole}}. \quad (3.25)$$

[†]We refer to Svoboda et al. [2004] for the definitions.

These energies are based on Equation (3.13). Now the total energy $U(\chi)$ of the state χ can be calculated as

$$U(\chi) = U_0 + \sum_{e=1}^n \chi_e \Delta U_e, \quad (3.26)$$

where U_0 is the energy of the state $(0, \dots, 0|0, \dots, 0)$. The energy difference due to the transfer from state χ to state ς can now be calculated as

$$\Delta U_\chi^\varsigma = U(\varsigma) - U(\chi) = \sum_{e=1}^n (\varsigma_e - \chi_e) \Delta U_e. \quad (3.27)$$

If the system is in a given state χ , we assume that it can transfer to a state ς within time t_χ^ς , which is exponentially distributed with rate parameter k_χ^ς if only a single element changes from 0 to 1 or vice versa. Following Bos et al. [2005], we assign to such elementary state changes from χ to ς a change rate k_χ^ς given by

$$k_\chi^\varsigma = \psi(f) \nu_\chi^\varsigma \frac{z}{6} \exp\left(-\frac{Q_\chi^\varsigma + \max(\Delta U_\chi^\varsigma, 0)}{R_g T}\right), \quad (3.28)$$

where f is the element that changed from 0 to 1 or vice versa and Q_χ^ς is the activation energy for atomic jumps. The function $\psi(f)$ is given by

$$\psi(f) = \frac{1}{2} (x_{m,f} u_{p,f} - 1) (\varsigma_f - \chi_f) + \frac{1}{2} (x_{m,f} u_{p,f} + 1). \quad (3.29)$$

Note that

$$\psi(f) = \begin{cases} x_{m,f} u_{p,f} & \text{if } \varsigma_f - \chi_f = 1, \\ 1 & \text{if } \varsigma_f - \chi_f = -1. \end{cases} \quad (3.30)$$

The variable $u_{p,f}$ is defined as the relative particle-lattice molar fraction of element f , given by

$$u_{p,f} = \begin{cases} \frac{x_{p,f}}{\sum_{e=1}^s x_{p,e}} & \text{if } 1 \leq f \leq s, \\ \frac{x_{p,f}}{\sum_{e=s+1}^n x_{p,e}} & \text{if } s+1 \leq f \leq n. \end{cases} \quad (3.31)$$

We included the function $\psi(f)$ in the change rate to account for the amount of element f present in both the matrix and the precipitate. The pre-exponential frequency ν_χ^ς , the vacancy concentration z , the activation energy for atomic jumps Q_χ^ς and the average inter-atomic spacing α are related to the diffusion coefficient D_f via the approximation [Porter and Easterling, 1992]

$$\nu_\chi^\varsigma \frac{z}{6} \exp\left(-\frac{Q_\chi^\varsigma}{R_g T}\right) \approx \frac{D_f}{\alpha^2}. \quad (3.32)$$

The description of the jump process fits the definition of a Continuous-Time Markov Chain [Ross, 1996], with transition rates from Equation (3.28). A graphical representation of this process for $n = 3$ and $s = 1$ is given in Figure 3.1. The

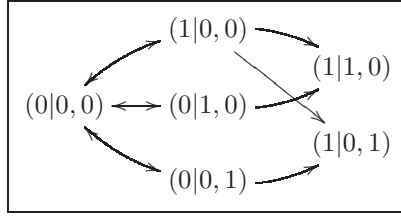


Figure 3.1: A graphical representation of the Continuous-Time Markov chain with $n = 3$ and $s = 1$ as discussed in Section 3.2.2.

entire process can be captured by a transition rate matrix Q , if we assign to each state χ a state number

$$\sigma(\chi) = (i + 1) \sum_{e=1}^s \chi_e e + \sum_{e=s+1}^n \chi_e (e - s) + 1. \quad (3.33)$$

For two different states χ and ς and associated state numbers $\sigma(\chi)$ and $\sigma(\varsigma)$, the transition matrix Q has at position $(\sigma(\chi), \sigma(\varsigma))$ the value

$$\begin{cases} k_\chi^\varsigma & \text{if } \chi \rightarrow \varsigma \text{ is possible,} \\ 0 & \text{if } \chi \rightarrow \varsigma \text{ is not possible.} \end{cases} \quad (3.34)$$

The diagonal of Q is such that the sum of each row of Q is zero.

Using this transition matrix Q , we can express the probabilities of being in state $i = 1, \dots, \mathbb{S}$ at time t with the vector $\mathbf{p}(t) = [p_1(t), p_2(t), \dots, p_{\mathbb{S}}(t)]$, which is given by the function

$$\mathbf{p}(t) = \mathbf{p}(0)e^{Qt}, \quad (3.35)$$

with $\mathbf{p}(0) = [1, 0, \dots, 0]$. We now approximate the effective attachment frequency λ_p^m by

$$\lambda_p^m = \frac{1}{t_p^*}, \quad (3.36)$$

where t_p^* is the expected time at which we are at any of the states that cannot be altered, i.e. both a substitutional and an interstitial element are present at their correct lattice positions. It can be shown that the value of t_p^* is given by

$$t_p^* = \int_0^\infty t \sum_{j \in \mathcal{T}} \frac{dp_j}{dt}(t) dt, \quad (3.37)$$

where \mathcal{T} is the set of states where one substitutional and one interstitial element are present. For a derivation of Equation (3.37) and how to calculate this integral, we refer to Appendix C. If $n = 1$, so a single element e within the precipitate, we can derive the following expressions for t_p^* and β_p^* :

$$t_p^* = \frac{\alpha^2}{D_e x_{m,e}}, \quad (3.38)$$

$$\beta_p^* = \frac{4\pi (r_p^*)^2 D_e x_{m,e}}{a_p^2 \alpha^2}, \quad (3.39)$$

which for $a_p = a_m$ and $\alpha \approx a_m$ gives the same values as Equation (3.17).

Comparison of Equation (3.22) to Equation (3.36), we see that, although both definitions use an effective frequency, the definition provided by Svoboda et al. [2004] uses an equation related to the harmonic mean, which is frequently used to determine average frequencies. Our formulation also takes into account the effects of atoms jumping back and forth between the two phases, which cannot be captured correctly by assuming an harmonic mean of jump frequencies.

3.2.3 Growth of precipitates

In the previous section, the nucleation rates I_p , which are incorporated in the source functions S_p of Equation (3.5), were discussed. The other factor influencing the time evolution of the precipitate distribution ϕ_p is the growth rate v_p of each precipitate with radius r . As we assume that a precipitate consists of multiple elements, we must have, following Zener [1949]

$$v_p = \frac{D_e C_{m,e} - C_{m,e}^{p/m,r}}{r C_{p,e} - C_{m,e}^{p/m,r}}, \quad \forall e \in \mathbb{E}_p, \quad (3.40)$$

in which $C_{m,e}^{p/m,r}$ is the concentration[†] of element e in the matrix at the precipitate/matrix interface for precipitate type p with radius r , $C_{m,e}$ the mean concentration[†] of element e in the matrix and $C_{p,e}$ the concentration[†] of element e in the precipitate. Since a single precipitate can only grow at one defined rate, we should have

$$\frac{D_e C_{m,e} - C_{m,e}^{p/m,r}}{r C_{p,e} - C_{m,e}^{p/m,r}} = \frac{D_f C_{m,f} - C_{m,f}^{p/m,r}}{r C_{p,f} - C_{m,f}^{p/m,r}}, \quad \forall (e, f) \in \mathbb{E}_p^2. \quad (3.41)$$

The above system contains $|\mathbb{E}_p| - 1$ unique nonlinear equations per precipitate type p , in which $C_{m,e}^{p/m,r}$, $e \in \mathbb{E}_p$ are the $|\mathbb{E}_p|$ unknowns and $|\mathbb{E}_p|$ is the number of elements in phase p . Given a growth rate v_p , we must also have

$$\frac{D_e C_{m,e} - C_{m,e}^{p/m,r}}{r - C_{m,e}^{p/m,r}} = v_p, \quad \forall e \in \mathbb{E} \setminus \mathbb{E}_p, \quad (3.42)$$

from which the concentration $C_{m,e}^{p/m,r}$ for an element e not present in the precipitate can be obtained. Define the mole fraction $x_{m,e}^{p/m,r}$ by

$$x_{m,e}^{p/m,r} = \frac{C_{m,e}^{p/m,r}}{\sum_{f \in \mathbb{E}} C_{m,f}^{p/m,r}} \quad \forall e \in \mathbb{E}. \quad (3.43)$$

If we assume that $C_{m,e}^{p/m,r}$ is influenced by surface effects, all $C_{m,e}^{p/m,r}$, $e \in \mathbb{E}_p$ are indirectly described by the Gibbs-Thomson effect

$$\frac{2\gamma_p V_p^a}{k_B T} \frac{1}{r} = \sum_{e \in \mathbb{E}_p} x_{p,e} \ln \left(\frac{x_{m,e}^{p/m,r}}{x_{m,e}^{p/m}} \right), \quad (3.44)$$

[†]In moles per cubic meter.

as was derived in Perez [2005]. Here $x_{m,e}^{p/m}$ is the local equilibrium concentration of element e in the matrix at the precipitate/matrix interface for precipitate type p . Equation (3.44) can be recast in the form

$$\prod_{e \in \mathbb{E}_p} \left(x_{m,e}^{p/m,r} \right)^{x_{p,e}} - \mathcal{K}_p(T) \exp \left(\frac{2\gamma_p V_p^a}{k_B T} \frac{1}{r} \right) = 0, \quad (3.45)$$

where we used Equation (3.15). The problem now reduces to finding $C_{m,e}^{p/m,r}$, $e \in \mathbb{E}_p$ such that Equations (3.41) and (3.45) hold for all $r \in [0, \infty)$ and $C_{m,e}^{p/m,r}$, $e \in \mathbb{E} \setminus \mathbb{E}_p$ are determined by Equation (3.42). After solving this nonlinear problem, we obtain the concentrations $x_{m,e}^{p/m,r}$ as functions of r , then we compute $v_p(r, t)$ for one of the elements $e \in \mathbb{E}_p$, which is now the unique growth rate of a precipitate of type p with radius r at time t .

3.2.4 Coupling of the multiple precipitate types

Although in Sections 3.2.2 and 3.2.3, nothing was said explicitly about the manner in which different precipitate types influence each other, the matrix mole fractions $x_{m,e}$ appear in Equations (3.13) and (3.29) and the matrix concentrations $C_{m,e}$ in Equations (3.40) and (3.42). The mole fraction within the matrix $x_{m,e}$ is related to the matrix concentrations $C_{m,e}$ by

$$x_{m,e} = \frac{C_{m,e}}{\sum_{f \in \mathbb{E}} C_{m,f}}. \quad (3.46)$$

Given the nominal molar fractions $x_{0,e}$, $e \in \mathbb{E}$, we can determine the nominal concentrations $C_{0,e}$, $e \in \mathbb{E}$ in moles per cubic meter by

$$C_{0,e} = \frac{x_{0,e}\rho}{\sum_{f \in \mathbb{E}} x_{0,f} M_f}, \quad (3.47)$$

with M_f the molar mass of element f and ρ the nominal density of the system. Then the matrix concentrations $C_{m,e}$ are given by

$$C_{m,e} = \frac{C_{0,e} - \sum_{p \in \mathbb{P}} C_{p,e} f_p^V}{1 - \sum_{p \in \mathbb{P}} f_p^V}, \quad (3.48)$$

with

$$f_p^V = \int_0^\infty \frac{4}{3} \pi r^3 \phi_p \, dr \quad \text{and} \quad C_{p,e} = \frac{n_{p,e}}{V_{\text{mole}}^p}. \quad (3.49)$$

3.3 Numerical methods

To be able to simulate the time evolution of the solution of Equation (3.5) for each precipitate type p , we discretise Equation (3.5) in the precipitate radius domain and integrate in time, respectively, with the finite-volume upwind method and the Euler Implicit scheme on a fixed set of size classes. Although these two methods are

theoretically first order in both time and place, we have chosen these methods as they are simple methods and they are known to preserve positivity and stability of the numerical solution unconditionally [Hundsdoerfer and Verwer, 2003]. We combine these methods with a variable time-step selection, of which the details can be found in Veldhuizen [2009]. The non-linear system of equations obtained by application of the upwind method and the Euler Implicit time integration are solved using Picard's Fixed Point method.

Each Picard step requires the determination of the growth rates of each precipitate. Since the growth of the precipitate should be defined by each chemical element that is present in the precipitate, we can use Equation (3.40) for each chemical element. This implies that Equation (3.41) should hold for each combination of chemical elements in the precipitate. Thereby, we can express all interfacial concentrations by choosing one of them and herewith by combining Equations (3.41), (3.42) and (3.43), we obtain Equation (3.45). Hence, Equation (3.45) is solved as a single nonlinear equation for one unknown using a quasi-Newton method.

Since we use a Picard method, combined with the aforementioned quasi-Newton method to solve the scalar Equation (3.45), to solve the multi-variate problem arising from discretisation of Equation (3.5) and an implicit time integration method, no numerical instabilities occurred. Furthermore, we observed good convergence for both the inner quasi-Newton method and the outer Picard method at each time-step.

In Myhr and Grong [2000], the size at which particles nucleate, which is the critical radius r_p^* , is increased by a small amount to $1.05r_p^*$, during the discretisation, to avoid numerical instability of the algorithm. A similar approach is taken within the software MatCalc [2012]. The increase is physically justified as a precipitate with radius r_p^* is unlikely to grow, so it will nucleate if it is slightly larger than r_p^* . In our opinion the value with which r_p^* is increased should tend to zero as the size class length tends to zero. To this end, we determine the size class $[r_{i^*-1/2}, r_{i^*+1/2}]$, in which r_p^* is located, and replace the source function in Equation (3.6) with

$$S_p(r, t) = \delta(r - r_{i^*+1})I_p(t), \quad (3.50)$$

where r_j represents the centre of the j^{th} size class. If we let the size class length tend to zero, the difference between the radii r_p^* and r_{i^*+1} will tend to zero, indicating that the solution of the discrete system will tend to the solution of Equation (3.5) with the source function from Equation (3.6). For the simulations in this chapter we use a geometric mesh containing 200 size classes between the lattice parameter of each precipitate and $0.1 \mu\text{m}$, i.e. $\Delta r_i = (1 + \epsilon)\Delta r_{i-1}$, $i = 2, \dots, 200$ with $\epsilon > 0$.

3.4 Results

In this section we simulate the precipitation kinetics in an industrial HSLA steel, of which the composition can be found in Table 3.1. Using the Thermo-Calc Software AB [2010] and restricting ourselves to the temperature $900 \text{ }^\circ\text{C}$, we see that the primary phase is austenite and three types of precipitates occur in this steel. The precipitate types are niobium-carbonitride, aluminium-nitride and manganese-sulphide. The mole fraction for niobium in the Nb(C,N)-precipitates is given by Thermo-Calc Software AB [2010] as 0.5, for carbon as 0.466 and for nitrogen as 0.034. The mole

Element	C	Nb	N	Al	Mn	S
wt%	0.06	0.017	0.004	0.03	0.25	0.005

Table 3.1: *The composition of the HSLA steel in weight percent used in this chapter.*

fraction for aluminium and nitrogen in the AlN-precipitates as well as the mole fractions for manganese and sulphur in the MnS-precipitates are taken as 0.5. We note that $x_{\text{Nb(C,N),C}}$ depends on the solute content. However, since we were not able to couple our code to thermodynamic databases, we take $x_{\text{Nb(C,N),C}}$ constant under isothermal conditions.

The solubility of each precipitate type is modelled using solubility products Hudd et al. [1971], Houghton [1993], Cheng [1999], Sun et al. [1992]:

$$\mathcal{K}_{\text{Nb(C,N)}}^w = (x\mathcal{K}_{\text{NbC}}^w)^x ((1-x)\mathcal{K}_{\text{NbN}}^w)^{1-x}, \quad (3.51)$$

$$\log_{10} \mathcal{K}_{\text{NbC}}^w = 3.2 - \frac{7690}{T}, \quad (3.52)$$

$$\log_{10} \mathcal{K}_{\text{NbN}}^w = 3.57 - \frac{9660}{T}, \quad (3.53)$$

$$\log_{10} \mathcal{K}_{\text{AlN}}^w = 1.03 - \frac{6770}{T}, \quad (3.54)$$

$$\ln \mathcal{K}_{\text{MnS}} = -0.01 - \frac{1}{2} \log(2) - \frac{11282.5}{T}, \quad (3.55)$$

where $x = 2x_{\text{Nb(C,N),C}} = 0.932$, the fraction of carbon on the interstitial lattice. We choose the effective interfacial energies of the precipitate types as $\gamma_{\text{Nb(C,N)}} = 0.19$ J/m², $\gamma_{\text{AlN}} = 0.20$ J/m² and $\gamma_{\text{MnS}} = 0.33$ J/m². These values differ from the ones found in literature [Banks et al., 2000, Furuhashi et al., 2003, Kozeschnik et al., 1999], however, they fall within the range as specified in Porter and Easterling [1992], and are chosen such that the simulations show the qualitative aspects of our model.

The main new features of our model are the multi-component definition of the frequency of atomic attachment, the multi-component growth rates and the coupling between the various precipitate types. A minor feature is the replacement of a fixed particle radius interval for nucleation with an interval length of the order of the local mesh width to mimic the formal use of the Dirac delta distribution in Equation (3.50). This minor detail allows a more rigorous convergence analysis. First we focus on the value of β_p^* for various approaches. Thereafter we show the results obtained for the multi-component growth rates, in comparison with the other used growth rates (see for example Robson [2004]). Finally, results from full simulations at 900 °C are shown and discussed.

3.4.1 Frequency of atomic attachment

Given the composition of the steel, the solubility product and the effective interfacial energy for Nb(C,N)-precipitates, we have computed the effective frequency λ_p^m for an NbC_xN_{1-x}-precipitate at 900 °C, where the amount of carbon x in the precipitate is varied from zero to one. Figure 3.2 shows the results of these computations, where the horizontal axis represents the fraction of carbon on the interstitial lattice and the

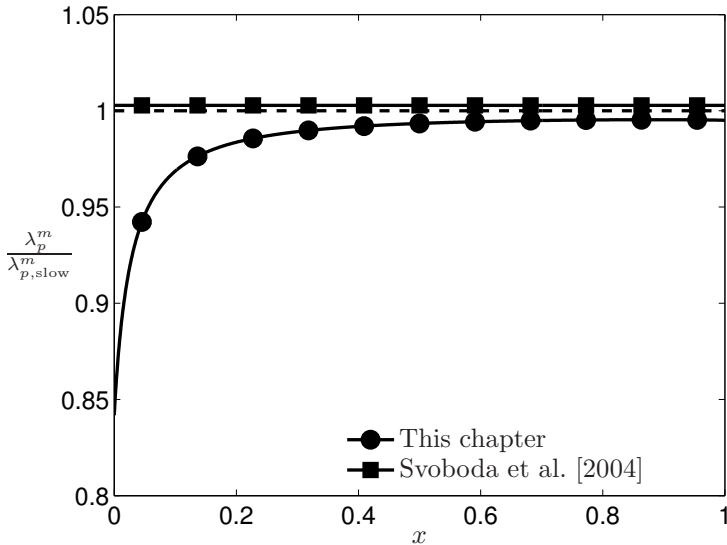


Figure 3.2: Comparison of the effective frequencies defined by Equations (3.36) and (3.22) relative to Equation (3.20) for a precipitate with stoichiometry NbC_xN_{1-x} for variable $x \in [0, 1]$.

vertical axis the ratio between the computed effective frequencies, Equations (3.36) and (3.22), and the effective frequency defined by the slowest element, i.e. niobium in this example, Equation (3.20). The approach in Equation (3.20) is referred to as the “single element approach”.

From Figure 3.2, one can see that the effective frequencies defined by Svoboda et al. [2004] and defined in this chapter are close to the “single element approach” which uses the slowest diffusing element, Equation (3.20). The effective frequency calculated by the model in Svoboda et al. [2004] is slightly higher than the “single element approach”, whereas our approach stays below the value obtained with the single element approach. The effective frequency in Svoboda et al. [2004] unexpectedly depends less strongly on the parameter x , whereas for lower values of x , i.e. nitrogen being the more abundant element, we have a relative reduction between 5 and 15 percent with respect to Equation (3.20). It is the authors’ believe that the presence of any other element besides the slowest diffusing element in a precipitate should reduce the effective frequency of Equation (3.20) to some degree, since each element influences the effective attachment frequency of a growing precipitate. The results obtained with Equation (3.36) reflect this property, whereas Equation (3.22) does not. As $x \rightarrow 0^+$ and $x \rightarrow 1^-$, we should arrive at two different limits, which is not reflected by applying Equations (3.22) and (3.20).

Since our value for x equals 0.932, the various models for β_p^* will not differ more than two percent, as can be concluded from Figure 3.2. Any simulation using these values will approximately yield the same quantitative results. Our model, however, has a richer theory than the two previously published models, which could be impor-

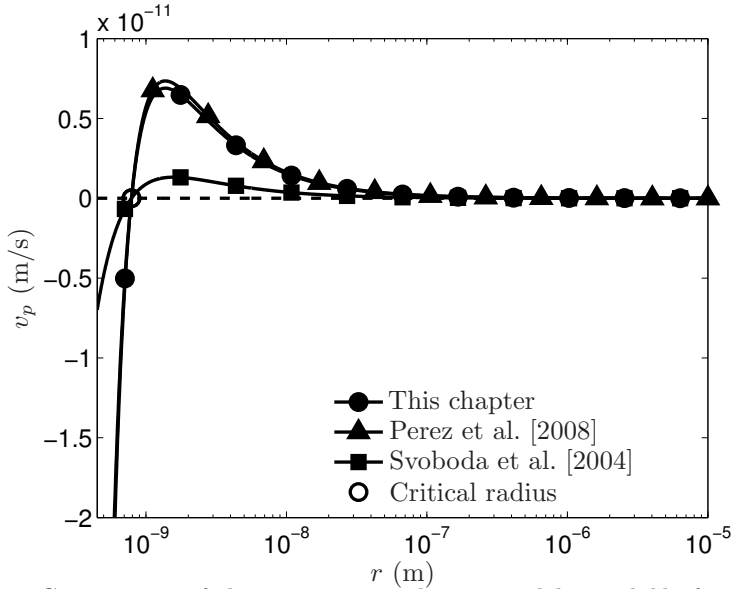


Figure 3.3: Comparison of the various growth rate models available for an Nb(C,N)-precipitate at 900 °C.

tant in some applications.

3.4.2 Multi-component growth

Our multi-component model for precipitate growth differs from the ones found recently in literature, see Perez et al. [2008] and Svoboda et al. [2004]. The model in Perez et al. [2008] uses Equations (3.40) and (3.45), but has replaced the concentrations in Equation (3.40) by mole fractions with appropriate weight factors for the conversions. In this model the mole fractions are the unknowns, but do not cause a reduction in the number of unknowns. A drawback is the possibility that due to numerical errors the calculated mole fractions can be larger than one, leading to nonphysical results. In our model we only have a non-negativity constraint on the unknowns, the mole fractions will always be between zero and one at all times and the sum of mole fractions equals unity at all times. The model in Svoboda et al. [2004] is based on solving their evolution equations, which are based on the thermodynamic extremum principle Onsager [1931a,b]. Their model has an analytical solution for precipitates with a constant composition, for which we refer to Svoboda et al. [2004].

Figure 3.3 shows for an Nb(C,N)-precipitate the obtained growth rates as a function of the radius at 900 °C. In this figure also the critical radius r_p^* is indicated. As one can see all three models provide graphs with the same shape, which all intersect the zero-growth axis at the critical radius, coinciding with the theory. The model of Svoboda et al. [2004] provides a significantly lower absolute value for the growth rate in comparison with our model and the model by Perez et al. [2008] up to a radius of approximately 0.1 μm . The model due to Perez et al. [2008] shows a slightly

higher value compared to our model, indicating that the model by Perez et al. [2008] is a good approximation of our model, under the assumption that the approximation given in Zener [1949] holds. From Figure 3.3, it is expected that the mean radii of a simulation with our model and the model of Perez et al. [2008] increase faster in time than the mean radius obtained with the model from Svoboda et al. [2004] due to the higher growth rates.

In Figure 3.4, some results from a simulation at 900 °C for an Nb(C,N)-precipitate are shown for all three growth models. Figure 3.4(a) shows, as expected, that the mean radius of the precipitates increases faster for our model and the model by Perez et al. [2008] than for the model due to Svoboda et al. [2004]. The values, however, have the same order of magnitude and show the same qualitative behaviour. Due to the lower growth rates in the model by Svoboda et al. [2004], more solute remains available for nucleation, which causes a longer increase in the number of precipitates, as can be seen from Figure 3.4(b). The lower growth rates cause the volume fraction to achieve its equilibrium value of $1.4088 \cdot 10^{-4}$ at a later time with respect to the other two models, Figure 3.4(c). All three models show nonetheless the same overall qualitative behaviour.

3.4.3 Interaction of multiple phases

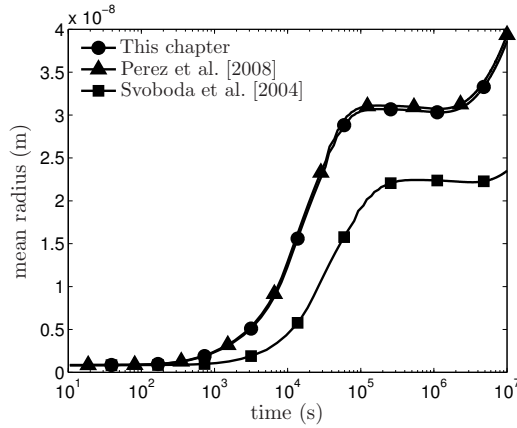
Due to the presence of nitrogen in both the Nb(C,N)-precipitates and in the AlN-precipitates and as a result of the natural nonlinear coupling between these precipitate types as discussed in Section 3.2.4, we expect some differences to occur in the nucleation and growth behaviour of the Nb(C,N)-precipitates and the AlN-precipitate, however not in the behaviour of the MnS-precipitates. To investigate these expected differences, we performed four simulations at 900 °C for the chosen HSLA steel, where three of them simulate the nucleation and growth of each precipitate type separately and in an uncoupled manner, and where the last one simulates the nucleation and growth of all three precipitate types simultaneously and in a coupled way. Some of the results of these simulations are shown in Figures 3.5 and 3.6. Figure 3.5 shows the saturation level S_p of the matrix with respect to a precipitate type p , defined by

$$S_p = \frac{\prod_{e \in \mathbb{E}_p} (x_{m,e})^{x_{p,e}}}{\mathcal{K}_p(T)}. \quad (3.56)$$

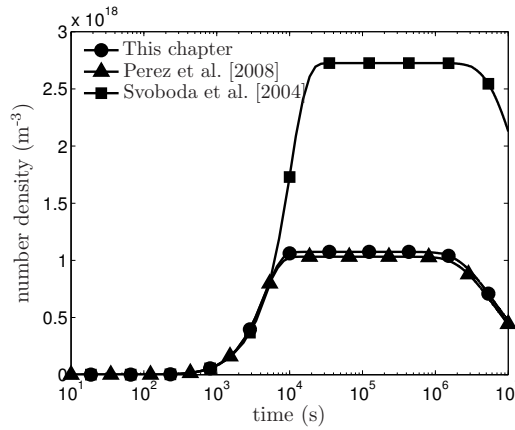
Figure 3.6 depicts the time-evolution of the volume fraction of each precipitate type.

The results in Figures 3.5 and 3.6 visualise the interaction between the various modelled precipitate types. The volume fraction and saturation of the Nb(C,N)-precipitates are slowed down upon incorporation of the interaction between the various precipitate types with respect to the single-precipitate formalism. The AlN-precipitates show a slight difference due the presence of the other precipitate types with respect to the single-precipitate formalism. The MnS-precipitates, however, show no major changes with respect to the single-precipitate formalism. To investigate these effects further, Figure 3.7 shows some results obtained for the Nb(C,N)-precipitates.

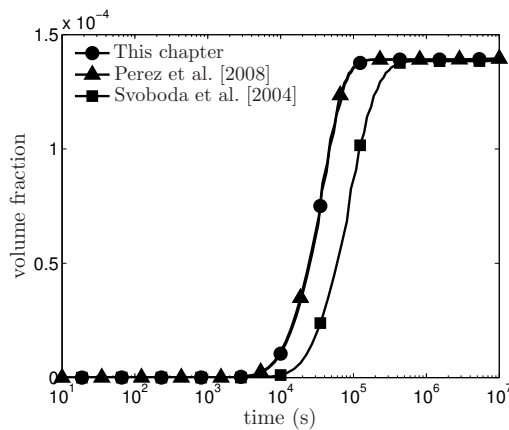
From Figure 3.7(a) we can clearly see that although nucleation of Nb(C,N)-precipitates starts at approximately 100 seconds in both simulations, the maximum nucleation rate is reduced to about a third in the coupled approach. This reduction is



(a) The mean radius as a function of time.



(b) The total number density as a function of time.



(c) The volume fraction as a function of time.

Figure 3.4: Comparison of simulation results at 900 °C between our model and the models from Perez et al. [2008] and Svoboda et al. [2004].

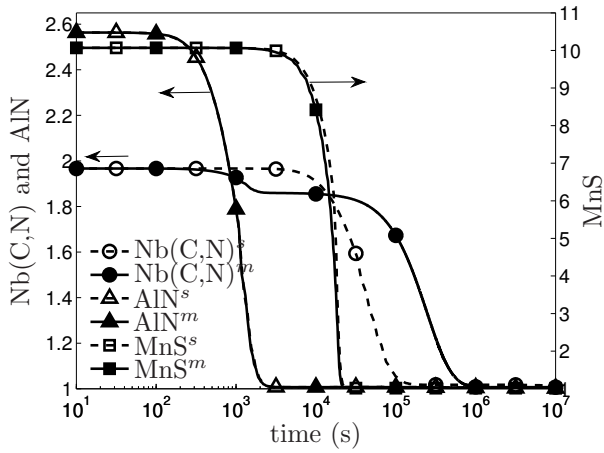


Figure 3.5: The saturation as a function of time at 900 °C. A superscript *s* refers to the single-precipitate formalism, a superscript *m* to the multi-precipitate formalism. On the vertical axis the species for which this axis holds is given.

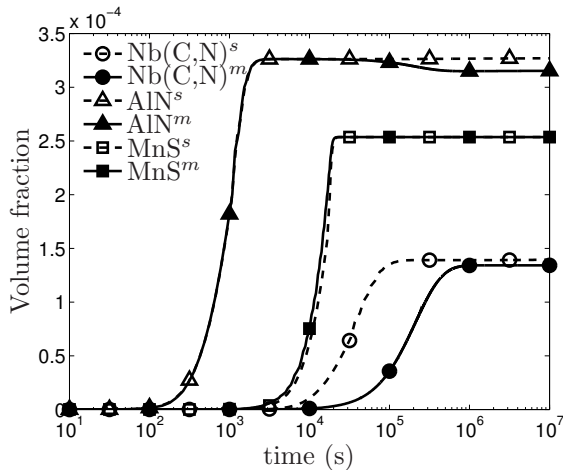
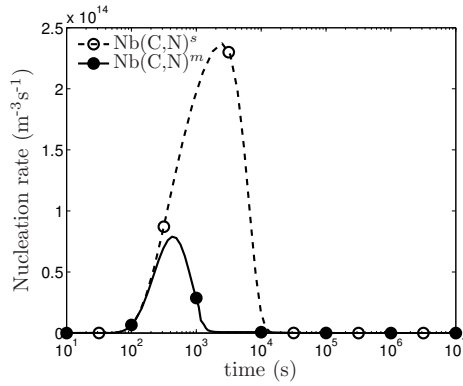
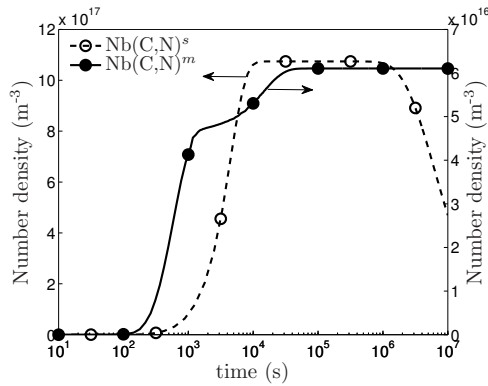


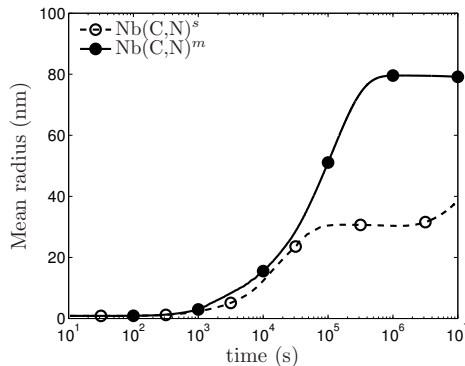
Figure 3.6: The volume fractions as a function of time at 900 °C. A superscript *s* refers to a single-precipitate formalism, a superscript *m* to the multi-precipitate formalism.



(a) The nucleation rate as a function of time.



(b) The total number density as a function of time.



(c) The mean precipitate radius as a function of time.

Figure 3.7: Comparison of simulation results at 900 °C for the $\text{Nb}(\text{C},\text{N})$ -precipitates. A superscript s refers to a single-precipitate formalism, a superscript m to the multi-precipitate formalism.

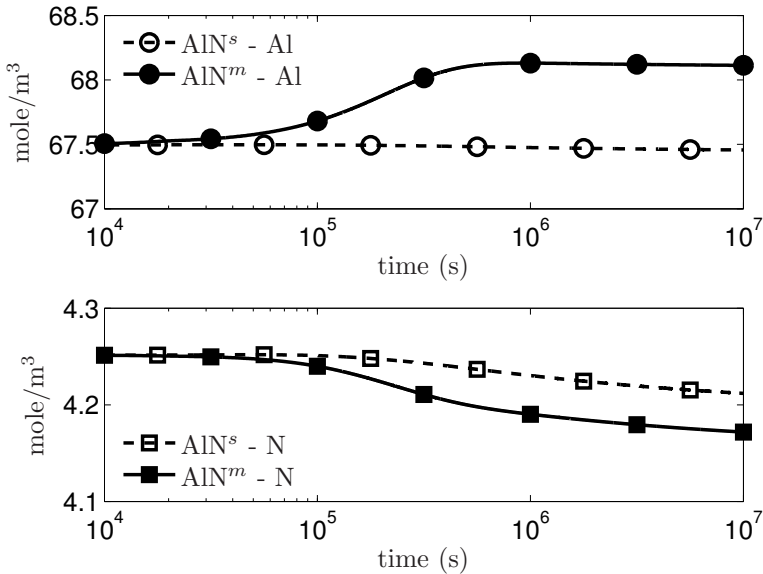


Figure 3.8: *The concentrations of aluminium and nitrogen as a function of time at 900 °C. A superscript s refers to a single-precipitate formalism, a superscript m to the multi-precipitate formalism.*

caused by the decrease of nitrogen in the matrix due to the nucleated AlN-precipitates. Close inspection of the curve for the coupled simulation also shows a slight decrease in the time-derivative of the nucleation rate at about 1,000 seconds. This decrease causes the number density of precipitates, see Figure 3.7(b), to continue to increase longer, although a lower total number density is achieved. Due to the lower number density of precipitates, the growth of precipitates is favoured, leading to a higher mean radius, Figure 3.7(c). We can also see that due to the longer nucleation period, no coarsening has started in the coupled simulation.

Figure 3.6 also shows a decrease of the volume fraction of AlN after 10,000 seconds in the coupled simulation, which coincides with the time at which a significant fraction Nb(C,N) has been formed, Figure 3.7(b). Inspection of Figure 3.8 shows that at 10,000 seconds the matrix concentration of aluminium increases, whereas the concentration of nitrogen in the matrix decreases. The increase of the aluminium concentration can only be caused by a dissolution of AlN-precipitates, which is consistent with the decrease in the volume fraction of the AlN-precipitates. Due to the rise of the aluminium concentration in the matrix the concentration of nitrogen in the matrix must decrease to keep the saturation with respect to AlN-precipitates at equilibrium. Since the Nb(C,N)-precipitates have not yet reached equilibrium, see Figure 3.5, but nucleation has stopped, see Figure 3.7(a), this decrease in nitrogen is balanced by a faster growth of the Nb(C,N)-precipitates, see Figure 3.7(c).

From the results presented in Figures 3.5 to 3.8 and the above discussion, we conclude that the simultaneous simulation of multiple precipitate types can reveal the nucleation behaviour that would not have been observed if each precipitate type would

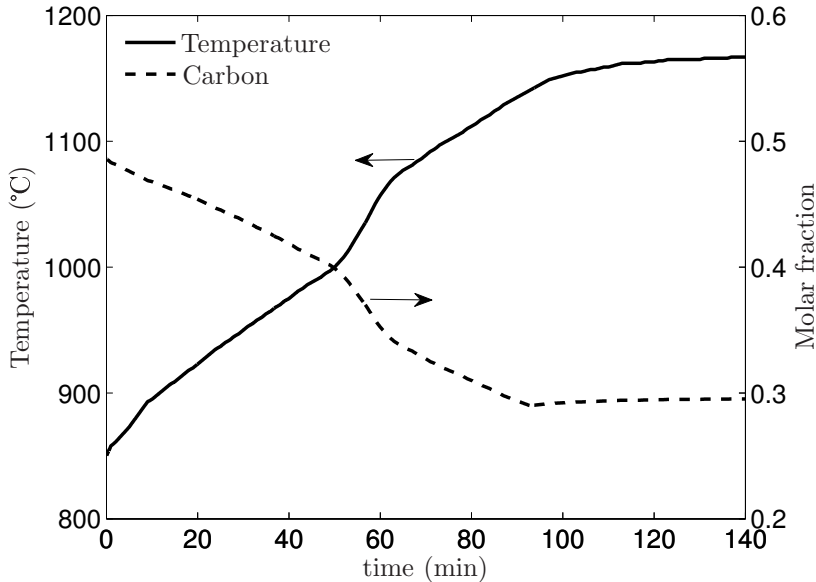


Figure 3.9: *The temperature profile and carbon mole fraction in Nb(C,N) used for the simulations in Section 3.4.4. This temperature profile represents the typical average temperature obtained during heating in an industrial oven.*

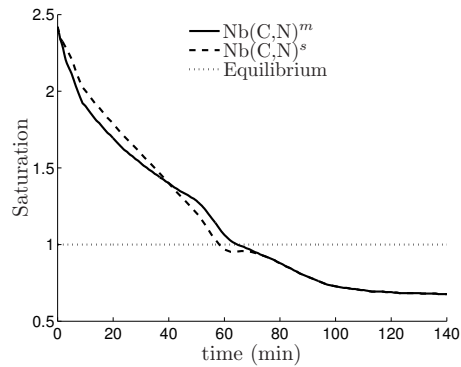
have been simulated separately. Furthermore, the coupling based on the elements present within the entire system between the various precipitate types has to be taken into account.

3.4.4 Application to heating

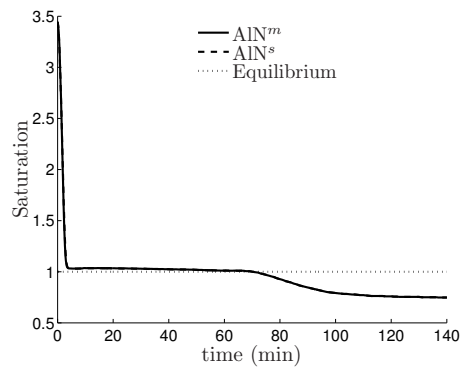
To show the versatility of the model we simulate precipitate nucleation and growth during heating of the steel in Table 3.1 using the temperature profile in Figure 3.9. We assume that initially no precipitates are present. Using Thermo-Calc Software AB [2010] we computed the equilibrium molar fraction of carbon in Nb(C,N) as a function of time, which is also shown in Figure 3.9. All other variables are taken similar to the previous values. Figures 3.10 and 3.11 show some of the results obtained for this simulation. To illustrate the impact of our new multi-species formalism, we also included the results for the uncoupled simulations of each precipitate type, similar to the previous section.

The AlN-precipitates attain the equilibrium volume fraction after 5 minutes, but as temperature increases, the matrix becomes undersaturated with respect to the AlN-precipitates at 70 minutes, causing dissolution and a decrease in volume fraction, reducing the volume fraction to zero after 80 minutes. No remarkable difference can be seen between the simulation with all precipitate-types and the simulation with only AlN-precipitates.

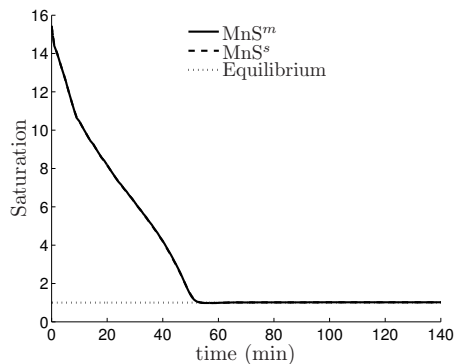
The MnS-precipitates attain the equilibrium volume fraction after 60 minutes, which is maintained further during the simulation. The decrease in the volume frac-



(a) Results for Nb(C,N).

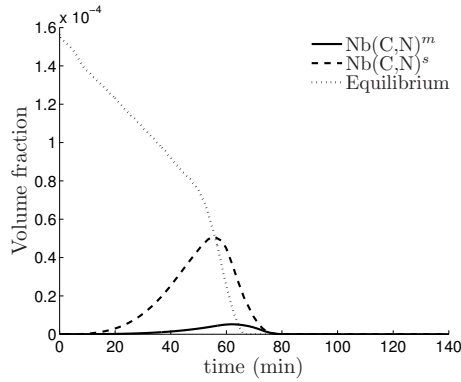


(b) Results for AlN.

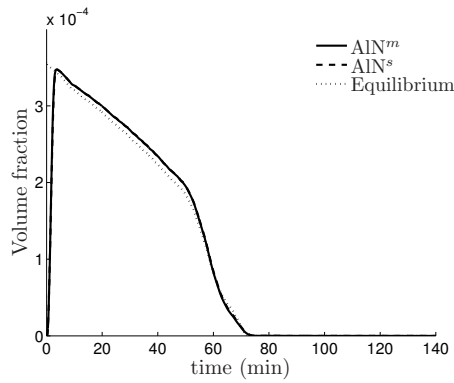


(c) Results for MnS.

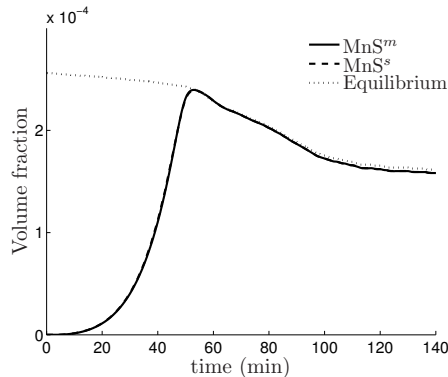
Figure 3.10: Comparison of simulation results for the saturation, see Equation (3.56), for the temperature profile in Figure 3.9. A superscript s refers to a single-precipitate formalism, a superscript m to the multi-precipitate formalism.



(a) Results for Nb(C,N).



(b) Results for AlN.



(c) Results for MnS.

Figure 3.11: Comparison of simulation results for the volume fraction for the temperature profile in Figure 3.9. A superscript s refers to a single-precipitate formalism, a superscript m to the multi-precipitate formalism.

tion of MnS-precipitates is due to an increase in the solubility product as a function of time, which indicates MnS-precipitates should dissolve to maintain at optimal saturation. No remarkable difference can be seen between the simulation with all precipitate-types and the simulation with only MnS-precipitates.

The Nb(C,N)-precipitates show, similarly to the previous section, a large difference between the simulation with all precipitate-types and the simulation with only Nb(C,N)-precipitates, indicating that the AlN-precipitates have a large influence on the nucleation and growth behaviour of Nb(C,N)-precipitates. Due to the rapid nucleation of AlN, the saturation of the Nb(C,N)-precipitates drops. This in turn reduces the driving force for nucleation, leading to fewer Nb(C,N)-precipitates and a lower attained volume fraction. Although the Nb(C,N)-precipitates are under-saturated after 60 minutes, a slight increase in saturation can be seen around 70 minutes. This small, and temporary, increase is an effect of the dissolution of AlN-precipitates at 70 minutes, leading to more nitrogen in solid solution, which directly influences the saturation of Nb(C,N)-precipitates. This is consistent with Equation (3.56). The effect of MnS-precipitates on the nucleation and growth of Nb(C,N) precipitates is small, as there is no large and direct influence of MnS-precipitates on the saturation of the matrix with respect to the Nb(C,N) precipitates. Simulations with only the nucleation and growth of Nb(C,N)- and MnS-precipitates have supported this conclusion.

A useful result from the simulations with the temperature profile from Figure 3.9, is the nucleation and subsequent full dissolution of both the AlN- and Nb(C,N)-precipitates. As we have started the simulations with no precipitates present, this indicates that even if we would have started with an initial distribution of any of these precipitate-types, full dissolution would still have been achieved. The MnS-precipitates, however, do not fully dissolve, indicating that if any precipitates are present initially, then some MnS-precipitates will remain present at the end of the heating period.

3.5 Conclusions

In this chapter, we extended the binary KWN-model [Kampmann and Wagner, 1991] for the nucleation and growth of precipitates to a model which describes nucleation and growth of multiple secondary phases, using nucleation and growth formulae depending on all elements present within the matrix and the precipitates. The time behaviour of the number density distribution has been described using a partial differential equation, where the nucleation of precipitates is given by a mathematical rigorous Dirac delta distribution function.

To incorporate a stronger dependence on the stoichiometry of the frequency of atomic attachment to a growing precipitate, we proposed a theoretical Continuous-Time Markov-Chain based model. Moreover, the model has been applied successfully to the nucleation of complex precipitates in an HSLA steel. We also note that different precipitate phases interact, which is accounted for in our model.

An improved model for the growth of precipitates has been proposed based on a molar balance on all alloying elements using the concentration in mole/m³ and the Gibbs-Thomson effect [Perez, 2005]. Use of the concentrations in mole/m³ rather than the mole fractions as in Perez et al. [2008] in the definition of the growth rates

leads to a more accurate model, as no artificial limits on the mole fractions have to be imposed during the calculations.

We, furthermore, analysed the influence of the introduced natural coupling between multiple precipitate types by application to an HSLA steel containing Nb(C,N)-, AlN- and MnS-precipitates. This analysis has shown that the coupling of the multiple phases is of importance during modelling and simulating of multiple secondary phases, as the simulations indicate that there is a mutual influence between the secondary phases during several stages of the nucleation and growth of secondary phases, both for isothermal and non-isothermal simulations.

Bibliography

- H.I. Aaronson, K.R. Kinsman and K.C. Russel. The volume free energy change associated with precipitate nucleation. Scripta Metallurgica, 4(2):101–106, 1970.
- K.M. Banks, A.P. Bentley and A. Koursaris. A precipitation model for predicting hot ductility behaviour in microalloyed steels. In 42nd Mechanical Working and Steel Processing Conference, pages 329–340, 2000.
- C. Bos, F. Sommer and E.J. Mittemeijer. An atomistic analysis of the interface mobility in a massive transformation. Acta Materialia, 53(20):5333 – 5341, 2005.
- L.M.L. Cheng. Study of the Kinetics of Precipitation, Dissolution and Coarsening of Aluminum Nitride in Low Carbon Steels. PhD thesis, The University of British Columbia, Vancouver, Canada, 1999.
- N.H. van Dijk, S.E. Offerman, W.G. Bouwman, M.Th. Rekveldt, J. Sietsma, S. van der Zwaag, A. Bodin and R.K. Heenan. High temperature SANS experiments on Nb(C,N) and MnS precipitates in HSLA steel. Metallurgical and Materials Transactions A, 33:1883 – 1891, 2002.
- B. Dutta, J. Palmiere and C.M. Sellars. Modelling the kinetics of strain induced precipitation in Nb microalloyed steels. Acta Materialia, 49:785–794, 2001.
- T. Furuhashi, J. Yamaguchi, N. Sugita, G. Miyamoto and T. Maki. Nucleation of proeutectoid ferrite on complex precipitates in austenite. ISIJ International, 43(10):1630–1639, 2003.
- D.C. Houghton. Equilibrium solubility and composition of mixed carbonitrides in microalloyed austenite. Acta Metallurgica et Materialia, 41(10):2993 – 3006, 1993.
- R.C. Hudd, A. Jones and M.N. Kale. Method for calculating the solubility and composition of carbonitride precipitates in steel with particular reference to niobium carbonitride. Journal of the Iron and Steel Institute, 209:121 – 125, 1971.
- H.M. Hulburt and S. Katz. Some problems in particle technology: A statistical mechanical formulation. Chemical Engineering Science, 19(8):555–574, 1964.
- W. Hundsdorfer and J.G. Verwer. Numerical Solution of Time-Dependent Advection-Diffusion-Reaction Equations, volume 33 of Springer Series in Computational Mathematics. Springer-Verlag, Berlin, Germany, 2003.

- R. Kampmann and R. Wagner. Materials Science and Technology - A Comprehensive Treatment, volume 5. VCH, Weinheim, Germany, 1991.
- E. Kozeschnik, V. Pletenev, N. Zolotarevsky and B. Buchmayr. Aluminum nitride precipitation and texture development in batch-annealed bake-hardening steel. Metallurgical and Materials Transactions A, 30(6):1663–1673, 1999. ISSN 1073-5623.
- R.J. LeVeque. Finite Volume Methods for Hyperbolic Problems (Cambridge Texts in Applied Mathematics). Cambridge University Press, United Kingdom of Great Britain and Northern Ireland, 2002.
- MatCalc. Institut für Werkstoffwissenschaft und Werkstofftechnologie, 2012. URL <http://matcalc.tuwien.ac.at>.
- O.R. Myhr and Ø. Grong. Modelling of non-isothermal transformations in alloys containing a particle distribution. Acta Materialia, 48(7):1605–1615, 2000.
- L. Onsager. Reciprocal relations in irreversible processes. i. Phys. Rev., 37:405–426, Feb 1931a.
- L. Onsager. Reciprocal Relations in irreversible processes. ii. Phys. Rev., 38:2265–2279, Dec 1931b.
- M. Perez. Gibbs-Thomson effects in phase transformations. Scripta Materialia, 52(8):709–712, 2005.
- M. Perez, M. Dumont and D. Acevedo-Reyes. Implementation of classical nucleation and growth theories for precipitation. Acta Materialia, 56(9):2119–2132, 2008.
- D.A. Porter and K.E. Easterling. Phase Transformations in Metals and Alloys. Chapman & Hall, London, United Kingdom of Great Britain and Northern Ireland, 2nd edition, 1992.
- J.D. Robson. Modelling the evolution of particle size distribution during nucleation, growth and coarsening. Materials Science and Technology, 20:441–448, 2004.
- S.M. Ross. Stochastic Processes. Probability and Mathematical Statistics. Wiley, New York, NY, United States of America, 1996.
- K.C. Russell. Phase transformations, page 219. American Society for Metals, Materials Park, OH, United States of America, 1970.
- K.C. Russell. Nucleation in solids: The induction and steady state effects. Advances in Colloid and Interface Science, 13(3 – 4):205 – 318, 1980.
- S.N. Samaras. Modelling of microstructure evolution during precipitation processes: a population balance approach of the KWN model. Modelling and Simulation in Materials Science and Engineering, 14(8):1271–1293, 2006.
- W. Sun, M. Militzer and J. Jonas. Strain-induced nucleation of MnS in electrical steels. Metallurgical and Materials Transactions A, 23:821 – 830, 1992.

- J. Svoboda, F.D. Fischer, P. Fratzl and E. Kozeschnik. Modelling of kinetics in multi-component multi-phase systems with spherical precipitates: I: Theory. Materials Science and Engineering: A, 385(1-2):166–174, 2004.
- Thermo-Calc Software AB. TCS Steel and Fe-alloys Database, 2010. URL http://www.thermocalc.com/res/pdfDBD/DBD_TCFE6.pdf.
- S. van Veldhuizen. Efficient numerical methods for the instationary solution of laminar reacting gas flow problems. PhD thesis, Delft University of Technology, The Netherlands, 2009.
- C. Zener. Theory of growth of spherical precipitates from solid solution. Journal of Applied Physics, 20(10):950–953, 1949.

Chapter 4

Modelling the evolution of multiple hardening mechanisms

Application to Fe-C-Mn-Ti martensite during tempering

4.1 Introduction

Tempered martensitic steel is the most commonly used material for high-strength fasteners in mass-produced car engines today [ISO 898-1, 2013]. These steels fulfil the typical requirements for the service conditions of fasteners used in current passenger cars: ultimate tensile strengths up to 1200 MPa and a recommended service temperature of 150-300 °C. However, the ongoing trend of engine down-sizing in order to reduce weight and CO₂-emissions results in higher mechanical and thermal loading of the engines. Stronger and yet tough steels are now required for engine fasteners. An important boundary condition for fastener steels is a low concentration of alloying elements that are abundantly available in order to assure cost efficiency and suitability of the steel for cold forging.

The strength of martensite originates from multiple strengthening mechanisms: 1) elements in solid solution, 2) grain boundaries, 3) dislocations, and 4) precipitates [Krauss, 1999]. The strength of martensite is therefore a complicated function of the martensite micro-structure as this evolves during tempering of the martensite. The micro-structure of martensite consists of the parent austenite grain structure which is sub-divided into packets. Each packet is divided into blocks and each block consists of parallel laths which are divided by walls of dislocations (lath boundaries) [Morito

This chapter is based on the article:

C.E.I.C. Öhlund, D. den Ouden, J. Weidow, M. Thuvander and S.E. Offerman. Modelling the evolution of multiple hardness components during tempering of Fe-C-Mn-Ti martensite. ISIJ International, 2015. ACCEPTED FOR PUBLICATION.

et al., 2006]. Moreover, the micro-structure of martensite consists of free dislocations, carbides, carbon atoms and other alloy atoms in solid solution. The carbon atoms are present in solid solution, as atoms segregated into lattice defects such as dislocations and/or as part of the different carbides. Substitutional alloying elements such as Ti are present in solid solution or in carbides.

The traditional fastener steels with strength levels up to 1200 MPa, such as 33B2 and 34Cr4, are essentially based on the first three strengthening mechanisms mentioned above. New steels for stronger fasteners have now been developed with additional strengthening from precipitates according to similar principles as used in HSLA steels [Baker, 2009]. Precipitates of V- and Ti-carbides are used to increase the strength to levels higher than 1200 MPa [Namimura et al., 2003]. The tempering temperature which is required for the nucleation and growth of secondary V or Ti-containing precipitates is above 500 °C, which fits with the requirements of the fastener standard ISO 898-1 [2013] and the low alloy additions enable the steel to be suitable for cold forming. More importantly, TiC-precipitates have the potential to act as hydrogen traps and improve the resistance to hydrogen-induced damage [Wei et al., 2003] during processing and service of the fastener. In addition to enhancing strength, thermally stable precipitates are also known to improve the temperature resistance of steels, by acting as pinning points for movement of dislocations [Abe et al., 2007]. The high thermal stability of TiC precipitates [Taneike et al., 2004] therefore makes medium-carbon steel with a small addition of Ti an interesting candidate for high-strength engine fasteners intended for service temperatures which exceed the current limit of 300 °C. The mechanical properties of such fasteners will be directly related to the martensite micro-structure with precipitates. Fundamental understanding of the evolution of the micro-structure and the resulting hardness during tempering of martensite with small additions of Ti is required to optimise the heat treatment process and the mechanical properties of the fastener.

The aim of this study is to model the evolution of the multiple hardening mechanisms during tempering of Fe-C-Mn-Ti martensite. We simulate the hardness evolution of martensite via linear addition of the hardening mechanisms. This hardness model is combined with a micro-structural multi-component and multi-phase Kampmann-Wagner-Numerical (KWN) model as developed by Ouden et al. [2013], for the simulation of TiC-precipitate nucleation and growth during tempering. The KWN-model takes into account the distribution of carbon atoms between phase fractions of TiC- and Fe₃C-precipitates. Moreover, the model simulates the evolution of recovery in order to estimate the effective diffusivity of Ti-atoms and in order to estimate the number of available nucleation sites for TiC-precipitates. The combined models are fitted to the experimental work of Öhlund et al. [2014].

4.2 Modelling the evolution of multiple hardness components during tempering

We assume that the separate hardening mechanisms due to grain size (gb), solid solution (ss), precipitates (P) and dislocations (d) can be added linearly, in agreement with Krauss [1999]:

$$\sigma_{\text{tot}} = \sigma_{\text{gb}} + \Delta\sigma_{\text{ss,C}} + \Delta\sigma_{\text{ss,Mn}} + \Delta\sigma_{\text{ss,Ti}} + \Delta\sigma_{\text{P,Fe}_3\text{C}} + \Delta\sigma_{\text{P,TiC}} + \Delta\sigma_{\text{d}}. \quad (4.1)$$

The total yield strength can thereafter be converted to hardness according to Hutchinson et al. [2011]:

$$HV = \frac{1}{3}\sigma_{\text{tot}}. \quad (4.2)$$

The Hall-Petch relationship is used to model the lattice friction and the grain boundary strengthening [Friedman and Chrzan, 1998]:

$$\sigma_{\text{gb}} = \sigma_1 + \frac{k_{\text{gb}}}{\sqrt{D}}, \quad (4.3)$$

where σ_1 is the lattice friction, k_{gb} the Hall-Petch factor and D the average diameter of the martensite grains. D is a function of time if grain coarsening takes place.

The effective grain size of martensite is reported to be the block size [Ohmura et al., 2001]. A Hall-Petch term has also been suggested for the lath sub-structure within the block, but we choose to include this effect in the term for dislocation density contribution [Nordström, 1976], because a lath boundary can be described by a stack of dislocations.

The increase in yield strength due to elements in solid solution, i.e. Ti and Mn, is simulated by the general form [Olson and Owen, 1992]:

$$\Delta\sigma_{\text{ss},i} = K_i c_i^{n_i}, \quad (4.4)$$

where K_i is a constant for alloy element i , ($i = \text{Ti}$ and Mn , respectively), c_i is the concentration of element i in weight percentages and n_i is a constant that can vary from 0.5 to 2 depending on the alloying element [Olson and Owen, 1992]. The concentrations of C, Ti and Mn in the matrix are functions of time, due to redistribution of Ti and Mn into Fe_3C and/or TiC. We set $n_{\text{Mn}} = 1$ in agreement with Nordström [1976] and we assume that $n_{\text{Ti}} = 1$ as both Mn and Ti are substitutional atoms. We do not include the effect of carbon atoms in solid solution in Equation (4.4). Literature reports that the strengthening effect of carbon atoms in solid solution in martensite is associated with an increase of dislocation density strengthening, caused by a higher carbon content [Nordström, 1976, Baker, 2009]. The carbon atoms diffuse to Cottrell atmospheres during quenching and therefore a higher dislocation density is maintained, as recovery is hindered via pinning of dislocations by the segregated carbon atoms.

The increase in strength due to precipitates is calculated according to the Orowan-Ashby equation [Gladman, 1997]:

$$\Delta\sigma_{\text{P},j} = \frac{0.538Gb\sqrt{f_j}}{2r_j} \log\left(\frac{r_j}{b}\right), \quad (4.5)$$

where G is the shear modulus of the matrix (calculated to be 80.4 GPa by a linear interpolation between the systems of Fe and Fe-1C at a concentration of 0.4 wt% C [Speich et al., 1972], b is the length of the Burgers vector (0.248 nm [Han et al., 2011]), f_j is the volume fraction of precipitate phase j and r_j is the average precipitate radius of phase j (TiC and Fe_3C). f_j and r_j are functions of time due to the nucleation and growth of Fe_3C - and TiC-precipitates.

The increase in yield strength by dislocations is calculated according to [Zurob et al., 2002]

$$\Delta\sigma_{\text{d}} = M\alpha Gb\sqrt{\rho}, \quad (4.6)$$

where $M=2.733$ (the Taylor factor) [Rosenberg and Piehler, 1971] and α (an empirical parameter) are constants. The dislocation density, ρ , is a function of time due to recovery. Recovery is in turn affected by the number density of precipitates present in the material, as precipitates pin dislocations. The effect of precipitates on the recovery kinetics can be described according to Zurob et al. [2002] by

$$\frac{d(\Delta\sigma_d)}{dt} = \begin{cases} \frac{-64(\Delta\sigma_d)^2\nu_d}{9M^3\alpha^2E} \exp\left(\frac{-U_\alpha}{k_B T}\right) \cdot \sinh\left(\frac{\Delta\sigma_d V_\alpha}{k_B T}\right) \left(1 - \frac{N(t)}{N_c(t)}\right) & \text{if } \frac{N(t)}{N_c(t)} \leq 1, \\ 0 & \text{otherwise,} \end{cases} \quad (4.7)$$

where ν_d and E are the Debye frequency and Young's modulus, respectively, and α has the same meaning as in Equation (4.6). U_α and V_α are the activation energy and activation volume for recovery, respectively, $N(t)$ is the number density of TiC precipitates, and $N_c(t)$ is the total number density of dislocation nodes. We use the same approximation as Zurob et al. [2002] for the number of dislocation nodes: $N_c(t) = \frac{1}{2}\rho(t)\sqrt{\rho(t)}$. Similar to Zurob et al. [2002], we also approximate ν_d and u_α using the self-diffusivity of iron in martensite [Shima et al., 2002] and the lattice parameter of martensite [Cheng et al., 1988]. V_α is assumed to be temperature independent. The parameters α and V_α are assumed unknown and will be fitted to the experimental data. We use Equation (4.7) to model the evolution of $\Delta\sigma_d$ as a function of time, and we thereafter calculate $\rho(t)$ via Equation (4.6). We assume that the micro-structure in the as-quenched state corresponds to 0% recovery and the dislocation density ρ_{AsQ} in the as-quenched state is $14.2 \times 10^{14} \text{ m}^{-2}$, as found in the literature [Morito et al., 2003].

The unknown parameters in the hardness model are σ_0 , K_{Mn} , K_{Ti} , α and V_α . The values for $f_{\text{Fe}_3\text{C}}$ and $r_{\text{Fe}_3\text{C}}$ are obtained from the experimental measurements presented in later sections. The values for f_{TiC} and r_{TiC} are obtained from simulations with the multi-component KWN model which is discussed in the next section. The concentrations of C, Ti and Mn in solid solution can be obtained from the measured and simulated data.

4.3 Modelling the nucleation and growth of TiC-precipitates during tempering

Literature reports that TiC precipitates in steel nucleate near dislocations [Wang et al., 2011] and that the nucleation rate of TiC is high, followed by slower growth and coarsening [Sawahata et al., 2008]. Studies have furthermore shown that both TiC nucleation and growth is enhanced by the presence of dislocations [Öhlund et al., 2014]. Literature furthermore reports that the presence of TiC precipitates in martensite affects the evolution of the dislocation density in steel during the heat treatment [Öhlund et al., 2014, Han et al., 2011]. The modelling of TiC nucleation and growth in martensite must therefore be linked to dislocation density and recovery in martensite during tempering.

4.3.1 Nucleation of TiC

We assume that the barrier for TiC nucleation in martensite is lowered via interactions between the strain field surrounding the dislocation and the nuclei, without annihilation of the dislocation core, in agreement with Xiao and Haasen [1989] and Hu and Chen [2001]. We furthermore assume that at the moment of nucleation the TiC precipitates are coherent with the matrix in three dimensions, which implies a cubic nucleus shape.

The classical nucleation theory describes the change in Gibbs free energy associated with a nucleation event of one such cubic nucleus as:

$$\Delta G = l^3 (\Delta g_v + \Delta g_s) + 6l^2 \gamma_{\text{eff}}, \quad (4.8)$$

where l is the length of the sides of the cubic nuclei, Δg_v is the chemical free energy change due to the formation of the precipitate phase (also called the driving force for nucleation), which has a negative sign in case of an oversaturated matrix, Δg_s is the misfit strain energy due to the formation of the precipitate in the host lattice and γ_{eff} is the effective interface energy of a precipitate which interacts with a nearby dislocation strain field. The effective interface energy is calculated according to Aaronson et al. [2010]:

$$\gamma_{\text{eff}} = \gamma - \sqrt[3]{\frac{\pi G b (1 + \nu)}{6 \cdot 3\pi (1 - \nu)}} e^T, \quad (4.9)$$

where γ is the interface energy between TiC and ferrite (0.339 Jm^{-2}) [Jang et al., 2012], G is the shear modulus of the matrix, b the Burgers vector of the dislocation, ν the Poisson's ratio of the matrix (calculated to be 0.286 by the same approach as for the value of G [Speich et al., 1972]) and e^T is the relative lattice misfit (6% according to Jang et al. [2012]).

The driving force for TiC-nucleation, Δg_v , is calculated by assuming a dilute solution approximation according to Ouden et al. [2013]:

$$\Delta g_v = -\frac{RT}{V_{\text{TiC}}^{\text{mole}}} \sum_i x_{\text{TiC},i} \log \left(\frac{x_{m,i}}{x_{m,i}^{\text{TiC}/m}} \right), \quad (4.10)$$

where $V_{\text{TiC}}^{\text{mole}}$ is the molar volume of TiC, $x_{\text{TiC},i}$ is the mole fraction of element i in the TiC precipitate, $x_{m,i}$ the mole fraction of element i in the matrix, $x_{m,i}^{\text{TiC}/m}$ the equilibrium mole fraction of element i in the matrix at the TiC/matrix interface and R is the gas constant.

The smallest possible nucleus of TiC is assumed to consist of one unit cell of TiC, corresponding to 14 titanium atoms, when all titanium atoms on the surface are counted as whole atoms. The minimum length of the cubic-shaped nucleus is therefore:

$$l_{\min} = \sqrt[3]{\frac{7}{2}} a_{\text{TiC}}, \quad (4.11)$$

where $a_{\text{TiC}} = 4.33 \text{ \AA}$ is the lattice parameter of TiC [Teresiak and Kubsch, 1995].

The critical nucleus size l^* is thereafter expressed by differentiation of Equation (4.8) with respect to l , equating to zero and solving for l :

$$l^* = \frac{-\gamma_{\text{eff}}}{\Delta h_v + \Delta g_s}. \quad (4.12)$$

The time dependent nucleation rate of TiC precipitates, I_{TiC} , is expressed as [Cahn, 1956]:

$$I_{\text{TiC}} = N_{v,\text{TiC}} Z \beta^* \exp\left(\frac{-\Delta G^*}{k_B T}\right) \exp\left(\frac{-\tau}{t}\right), \quad (4.13)$$

where k_B is the Boltzmann constant, T is temperature, $N_{v,\text{TiC}}$ is the number density of potential nuclei sites for TiC, Z is the Zeldovich factor, β^* is the frequency of atomic attachment to the growing precipitate and τ is the incubation time.

The number density of possible nucleation sites is as assumed to be all substitutional atomic sites within the capture radius of the dislocation:

$$N_{v,\text{TiC}} = \pi r_c^2 \rho(t) N_{v,0}. \quad (4.14)$$

We use the same $\rho(t)$ as modelled according to Equations (4.6) and (4.7). $N_{v,0}$ is the number density of substitutional atomic sites per m^3 and r_c is the capture radius of each dislocation. The capture radius of the dislocations is calculated according to [Wang and Shiflet, 1998]:

$$r_c = \frac{Gb(1+\nu)\Delta v}{12\pi(1-\nu)k_B T} \exp(0.577), \quad (4.15)$$

where Δv is the volume difference between matrix and solute atoms [Wang and Shiflet, 1998]. We calculate the volume difference between matrix and solute atoms by comparing the volume of one single Fe atom in a BCC unit cell of iron with the volume of one single Ti atom in a BCC unit cell of Ti using the lattice parameters as reported by Rickerby [1982]. The capture radius as calculated from Equation (4.15) is 8.7 Å at 550 °C.

The Zeldovich factor is described according to Ouden et al. [2013]:

$$Z = \sqrt{\frac{2\gamma_{\text{eff}}}{3k_B T}} V_{\text{TiC}}^{\text{atom}} \left(\frac{1}{l^*}\right)^2, \quad (4.16)$$

where $V_{\text{TiC}}^{\text{atom}}$ is the atomic volume of TiC. The frequency of atomic attachment to the growing sub-critical nucleus is expressed as [Ouden et al., 2013]

$$\beta^* = \frac{6(l^*)^2}{a_{\text{TiC}}^2} \lambda_{\text{TiC}}^m, \quad (4.17)$$

where λ_{TiC}^m is the effective attachment frequency of a TiC structural unit, modelled as in Ouden et al. [2013]. The incubation time is given by

$$\tau = \frac{1}{2Z^2\beta^*}. \quad (4.18)$$

4.3.2 Growth of TiC

The shape of the critical nucleus is converted from a cubical to a spherical nucleus, while keeping the precipitate volume and the total Gibbs free energy constant. This

leads to a critical nucleus radius r^* and an effective spherical interface energy γ_r with equations:

$$r^* = \sqrt[3]{\frac{3}{4\pi}} l^*, \quad (4.19)$$

$$\gamma_r = \sqrt[3]{\frac{6}{\pi}} \gamma_{\text{eff}}. \quad (4.20)$$

The growth of all precipitates is thereafter modelled using a Zener approach for spherical precipitates, where the growth rate, v_{TiC} , of each precipitate with radius r is expressed as [Zener, 1949]:

$$v_{\text{TiC}} = \frac{D_i}{r} \frac{c_{m,i} - c_{m,i}^{\text{TiC}/m}}{c_{\text{TiC},i} - c_{m,i}^{\text{TiC}/m}}, \quad (4.21)$$

where D_i is the effective diffusivity of element i in martensite, $c_{m,i}$ is the concentration of element i in the matrix, $c_{\text{TiC},i}$ is the concentration of element i in the precipitate and $c_{m,i}^{\text{TiC}/m}$ is the concentration of element i in the matrix at the precipitate/matrix interface. All concentrations are in the units moles per m^3 . The above equation must be true for each of the elements C, Ti and Mn, which leads to three equations with the four unknowns v_{TiC} , $c_{m,\text{C}}^{\text{TiC}/m}$, $c_{m,\text{Ti}}^{\text{TiC}/m}$ and $c_{m,\text{Mn}}^{\text{TiC}/m}$. The concentrations for iron are obtained by a mole balance.

The fourth equation needed to solve for the four unknowns is given by an adjusted form of the Gibbs-Thomson effect, which includes the effects of misfit strain energy:

$$\sum_i x_{\text{TiC},i} \log \left(\frac{x_{m,i}^{\text{TiC}/m,r}}{x_{m,i}^{\text{TiC}/m,\infty}} \right) = \frac{V_{\text{TiC}}^{\text{atom}} \gamma_r}{k_B T} \frac{2}{r} + \frac{V_{\text{TiC}}^{\text{atom}}}{k_B T} \Delta g_s. \quad (4.22)$$

This equation can be derived similar to the procedure given in Perez [2005]. We adjust the Gibbs-Thomson effect to account for the misfit strain energy to obtain consistency between the nucleation part of the model and the growth part of the model: if the Gibbs-Thomson effect is not adjusted for the effect of the misfit strain energy, a precipitate with zero growth rate, i.e. $v_{\text{TiC}} = 0$, will have a radius unequal to r^* , which is physically incorrect.

Earlier studies have shown that the high dislocation density of martensite increases the diffusion rate in martensite [Öhlund et al., 2014]. The effective diffusivities of C, Ti and Mn in martensite, D_C , D_{Ti} and D_{Mn} , are therefore taken as a balance between the lattice diffusivities, D_C^L , D_{Ti}^L and D_{Mn}^L , and the pipe diffusivities, D_C^P , D_{Ti}^P and D_{Mn}^P , on the format given by Porter and Easterling [1992] where we remove the cross section area for pipe diffusivity from the area of lattice diffusivity:

$$D_i = (1 - g(t)) D_C^L + g(t) D_C^P. \quad (4.23)$$

Here $g(t) = \pi b^2$ is the cross sectional area of dislocation pipe per unit area of matrix.

The pipe diffusivities for Ti and Mn are unknown, but under the assumption that the presence of a dislocation lowers the energy barrier for diffusion, it is reasonable to assume that the ratio between the bulk diffusivities and the pipe diffusivities of

the elements C, Ti and Mn is equal to the ratio between the bulk diffusivity and pipe diffusivity of Fe:

$$\frac{D_e^P}{D_e^L} = \frac{D_{Fe}^P}{D_{Fe}^L}, \quad (4.24)$$

where the last ratio is found in Shima et al. [2002]. The effective pipe radius of a dislocation is set equal to the Burgers vector, b , and the cross sectional area of dislocation per unit area of matrix is expressed as:

$$g(t) = \rho(t)\pi b^2. \quad (4.25)$$

The number balance of precipitates in the model is described according to [Ouden et al., 2013]

$$\frac{\partial \phi}{\partial t} = -\frac{\partial [v_{TiC}\phi]}{\partial r} + \delta(r - r_{k_B T}^*)I_{TiC}, \quad (4.26)$$

in which $\phi = \phi(r, t)$ in m^{-4} is the number density distribution of precipitates of radius r at time t and v_{TiC} in ms^{-1} represents the growth rate of precipitates of radius r at time t . The radius $r_{k_B T}^*$ is the radius for which the energy of nucleation is $k_B T$ less than the energy for r^* (assuming $r_{k_B T}^* > r^*$).

The key features of the model for TiC precipitation [Ouden et al., 2013] are the inclusion of multi-component and multi-phase effects within the model. In Ouden et al. [2013] it has been shown that the model is capable of dealing with the multiple secondary phases which compete for the same solid solution elements.

We choose a different numerical method than that from Ouden et al. [2013]. We use a combination of Strang splitting, first-order upwinding [LeVeque, 2002], Implicit and Explicit Euler time-integration and adaptive mesh techniques. The initial mesh contains 500 bins on a logarithmic scale, similar to Ouden et al. [2013]. The simulation is following the same temperature profile as applied directly after quenching during the experiments of Öhlund et al. [2014].

4.4 Experimental

We have published the experimental methods and results elsewhere before [see Öhlund et al., 2014]. The experimental results are now being used as input parameters and validation for the proposed model. Two high-purity Fe-C-Mn steels are investigated: one without Ti and one with the addition of 0.042 wt% Ti. The compositions of the steels are given in Table 4.1. The Ti-free steel is austenitised at 940 °C for 40 minutes and the Ti-containing steel is homogenised and austenitised at 1350 °C for 30 minutes. The austenisation temperature of 1350 °C is chosen to assure that all Ti atoms are in solid solution. The different austenisation times are chosen to obtain similar austenite grain sizes. Both steels are quenched to room temperature from their respective austenisation temperature, using He-gas followed by tempering treatments performed at 300 °C and 550 °C for 5, 10, 30 and 60 minutes. The heating time up to the full tempering temperature is 138 seconds. The tempering temperature of 300 °C is chosen to assure that all Ti atoms remain in solid solution, as nucleation of TiC does not take place during tempering at 300 °C [Wei et al., 2003]. The tempering level of 550 °C is chosen to assure that TiC nucleation and growth takes place during

Steel	C	Mn	Si	P	S	Al	Ti	Cu	Cr	O	V
Ti-free	0.39	0.8700	0.0035	0.0010	0.0007	0.0050	-	0.0012	0.0018	0.0080	0.0023
Ti-containing	0.39	0.8700	0.0040	0.0011	0.0007	0.0047	0.0420	0.0012	0.0022	0.0046	0.0022

Table 4.1: *Chemical composition of the examined steels in wt%.*

tempering, as literature reports that TiC nucleation takes place at temperatures near 550 °C Wei et al. [2003].

Micro-Vickers hardness (HV0.5) is used to study the evolution of macroscopic hardness. Scanning electron microscopy (SEM, JEOL JSM-6500F with field emission gun) is used to study the evolution of Fe₃C-particle size volume fraction. Electron back-scatter diffraction (EBSD with a Nordlys detector) is used to study the coarsening of martensite blocks and the evolution of recovery in the martensite lattice. The methodology to extract information about the recovery from the EBSD-measurements is explained in Öhlund et al. [2014]. Atom probe tomography is used to measure the concentration of carbon and titanium atoms in solid solution and the TiC-precipitate size in the Ti-containing martensite after 60 minutes of tempering at 550 °C.

4.5 Model fitting

4.5.1 Input parameters

The EBSD measurements in Öhlund et al. [2014] show that no grain coarsening takes place during tempering. Therefore, we take σ_{gb} in Equation (4.3) as a constant.

The SEM measurements of Fe₃C particle width, W , and length, L , are used to calculate the volume fraction of Fe₃C precipitates, as measured by SEM. We calculate the volume of each Fe₃C-particle that is measured within a square area of SEM images using

$$V = \pi \frac{W^2 L}{2}. \quad (4.27)$$

The total volume of all particles is summed within each sample. The volume fraction of Fe₃C-precipitates is thereafter determined for each sample, assuming a cubic measurement volume. We now use the APT measurements of carbon atoms in solid solution to estimate a control measurement of the volume fraction of formed Fe₃C in the Ti-containing steel after 60 minutes of tempering at 550 °C. The APT measurements show that the concentration of carbon atoms in solid solution is 35×10^{-3} at% C in the Ti-containing steel after 60 minutes of tempering at 550 °C. ThermoCalc simulations (TCFE6) of the Ti-containing steel show that the equilibrium concentration of C in solid solution in ferrite at 550 °C is 1.8×10^{-3} at%. We assume that carbon is distributed between TiC, Fe₃C and C in solid solution and derive that the volume fraction of formed Fe₃C is 0.057 (98% of the equilibrium volume fraction) after 60 minutes of isothermal tempering at 550 °C.

We note that the volume fraction of Fe₃C-precipitates in the Ti-containing steel after 60 minutes of isothermal tempering at 550 °C that is determined from SEM measurements is 0.087. The higher volume fraction we measure from SEM can be due to a slight overestimation of particle dimensions from SEM pictures and due to the assumption of an oval particle shape (Equation (4.27)). We therefore determine a

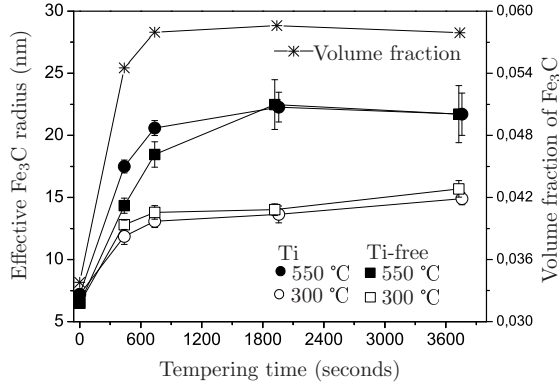


Figure 4.1: *Effective Fe_3C radius (nm) of Ti-free and Ti-containing martensite during annealing at 300 °C and 550 °C as a function of annealing time and the volume fraction of Fe_3C in the Ti-containing steel after annealing at 550 °C. Error bars represent 95% confidence intervals.*

scale factor from the relationship we find between the SEM and APT volume fraction results for the Ti-containing steel after 60 minutes of tempering at 550 °C. The total volume fraction of Fe_3C , as determined by SEM, is thereafter scaled for each examined specimen. The effective radius of the Fe_3C -particles in each specimen is calculated from the scaled SEM volume fraction of Fe_3C , by assuming spherical particles. We use scaled results of volume fraction and effective Fe_3C radius as input parameters to the model.

Figure 4.1 shows the effective Fe_3C radius and volume fraction of Fe_3C , as a function of tempering time, that are used as input parameters in the model. The four curves for volume fraction of Fe_3C are overlapping, and we therefore show only the Ti-containing steel at 550 °C. Both the effective precipitate size and the volume fraction of Fe_3C grow rapidly during the first 5 minutes of isothermal tempering. After 5 minutes of isothermal tempering the growth continues at a lower rate, and after 10 minutes the values stabilise. We note that the spread in cementite particle size increases with tempering time, during tempering at 550 °C, which is reflected by the increase in the size of the error bars for the average cementite particle size.

The small carbides which are observed in the as-quenched state could correspond to ϵ -carbides, based on their size and that they are present directly after quenching. In the present model, all the iron-carbides are modelled as Fe_3C -particles. The volume fraction of Fe_3C is used to calculate the input parameter of carbon concentration in solid solution to the model, as only one data point for the carbon concentration in solid-solution was measured by APT (at 60 minutes of isothermal tempering at 550 °C for the Ti-containing steel).

4.5.2 Fitting approach

The parameters σ_{gb} , K_{Mn} , K_{Ti} , α and V_α of the hardness model are currently unknown. Two of these parameters, α and V_α are also used within the KWN TiC

Parameter	Value	Unit
σ_0	340	MPa
K_{Mn}	0	MPa(wt%) ⁻¹
K_{Ti}	1679	MPa(wt%) ⁻¹
α	0.401	
V_α	16.99b ³	m ³
Δg_s	1.3359	GJ/m ³

Table 4.2: Results from least-squares fitting of Equations (4.1) and (4.2) to the measured hardness.

precipitation model, together with the misfit strain energy Δg_s for the TiC precipitates. We will use the following approach to obtain estimates of these parameters:

- σ_{gb} , K_{Mn} , K_{Ti} , α and V_α are fitted using least-squares techniques by minimising the residual between the predicted hardness given by Equations (4.1) and (4.2) of the model and the measured hardness from experiments. We simultaneously fit the model to the experimental data from the Ti containing steel at 300 °C and the Ti free steel at 300 °C and 550 °C at 0, 5, 10, 30 and 60 minutes of tempering. The Ti-containing steel heat-treated at 550 °C is excluded from the fitting of the above parameters in order to avoid the influence of TiC precipitates.
- Δg_s is obtained by using a least-squares techniques by minimising again the residual between the predicted hardness and the measured hardness, where the values for the parameters σ_{gb} , K_C , K_{Mn} , K_{Ti} , α and V_α from the previous step are used within the hardness model and the TiC precipitation model. Only the data for the Ti-containing steel during tempering at 550 °C after 0, 5, 10, 30 and 60 minutes is used to obtain the value of Δg_s .

4.6 Results and discussion

4.6.1 Fitting parameters

Figure 4.2 shows the measured hardness (symbols) and the fitted (lines) hardness as a function of annealing time of a) the Ti-free steel at 300 °C and °C and the Ti-containing steel at 300 °C and b) the Ti-containing steel at 550 °C. The comparison between the experiment and the model in Figure 4.2(a) is obtained for the values for the fitting parameters σ_{gb} , K_{Mn} , K_{Ti} , α and V_α . The comparison between the experiment and the model in Figure 4.2(b) is used to fit a value for the strain energy Δg_s . From Figure 4.2 it can be seen that the fitted model correctly describes the evolution of the hardness during tempering. The fitted parameters σ_{gb} , K_{Mn} , K_{Ti} , α , V_α and Δg_s are given in Table 4.2.

In the following section we compare the values of the fitted parameters to the values reported in literature. The σ_{gb} of our model is the combination of lattice friction and the hardness contribution of the martensite block structure (grain size hardening). The model predicts $\sigma_{gb} = 340$ MPa or 113 HV. This calculated value is lower than the value of 413 MPa which is given in literature [Krauss, 1999]. This

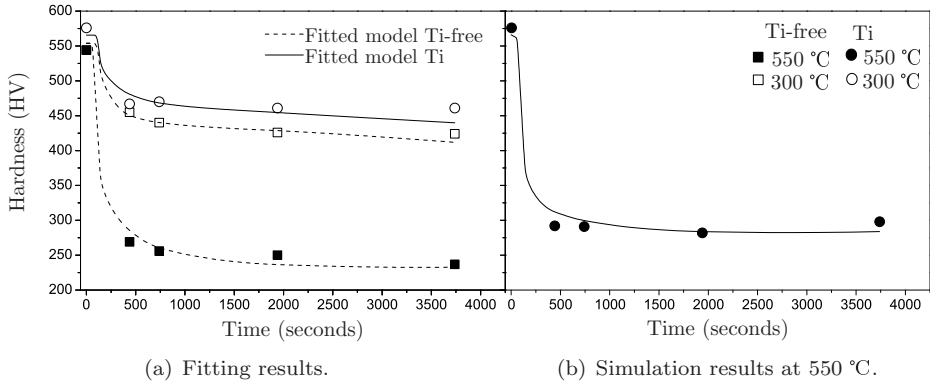


Figure 4.2: *The measured hardness (symbols) and the fitted hardness (lines) of (a) the Ti-free steel at 300 °C and 550 °C and the Ti-containing steel at 300 °C as a function of annealing time for the fitting of the hardness model and (b) the simulation of the Ti-containing steel at 550 °C. 95% confidence intervals are covered by the symbols.*

difference can be due to the difference in grain size that we use and the grain size that is used in literature. The literature value of 413 MPa is based on the grain size and the average lath width of 0.25 μm . This is smaller than the effective grain size (determined by the block boundaries) that we used in our model.

The value of 0.401 that we find for α is in good agreement with the literature reports on α , ranging from 0.24 to 1 [Han et al., 2011, Lagneborg and Bergman, 1976]. We note that the experimental work of Öhlund et al. [2014] shows that the concentration of carbon atoms in true solid solution (between laths) and the concentration of carbon atoms segregated to lath boundaries (high dislocation density) are 0.005 wt% and 0.045 wt%, respectively, after 60 minutes of tempering at 550C. This indicates that the majority of carbon atoms in the martensite have segregated to dislocations and that Equation (4.4) therefore covers the major influence of carbon atoms in solid solution on the martensite strength.

The activation volume of the recovery process in martensite, V_α , is compared to the literature value for the activation volume of the recovery process in BCC iron. Our model predicts a value of $17b^3$ or 0.26 nm^3 , which is in good agreement with the reported values of 0.1 to 0.6 nm^3 [Smith et al., 2004].

The fitted values of the K_{Mn} -parameter is zero, whereas literature reports a value of $K_{\text{Mn}} = 35 \text{ MPa}(\text{wt}\%)^{-1}$ [Nordström, 1976]. The difference between our fitted value of $K_{\text{Mn}} = 0$ and the literature value of $K_{\text{Mn}} = 35 \text{ MPa}(\text{wt}\%)^{-1}$, falls within the uncertainties of our experiments and the uncertainties of the experiments reported in literature. We estimate that Mn in solid solution contributes with a maximum of 10 HV to the total hardness in our system. Here we assume that the Mn-atoms do not have time to redistribute during the formation of cementite so that the overall manganese concentration in the matrix corresponds to the overall concentration of 0.87 wt% Mn in the steel. The strengthening effect of Mn in solid solution in the as-quenched martensite is therefore approx. 30 MPa (or 10 HV), in case we use the literature value for $K_{\text{Mn}} = 35 \text{ MPa}(\text{wt}\%)^{-1}$ and Equation (4.4). In case the Mn-atoms would redistribute into cementite, the Mn-concentration in the matrix would be even

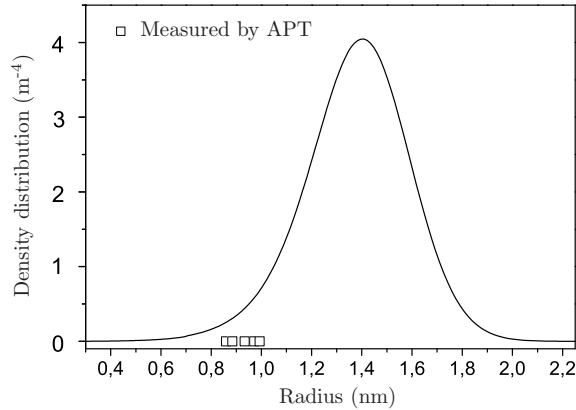


Figure 4.3: *The simulated TiC precipitate size distribution and the experimental precipitate sizes (symbols) as measured by APT.*

lower and subsequently the added strength. The error in our hardness measurements is approx. ± 5 HV. The steels used by Nordström [1976] contain sulphur, which may form MnS precipitates. The formation of MnS can influence the hardness by precipitate strengthening and the literature value of $35 \text{ MPa}(\text{wt}\%)^{-1}$ for K_{Mn} may therefore be biased.

There are not many reports in the literature about the strain energy Δg_s of TiC-precipitates in martensite. Jang et al. [2012] have used first principles calculations to estimate a value of 4.10 kJ/mol or 1.16 GJ/m³. This value corresponds well to our fitted value of 1.34 GJ/m³ or 4.74 kJ/mol.

4.6.2 TiC-precipitates and recovery

Figure 4.3 shows the calculated TiC precipitate size distribution together with the TiC precipitate sizes measured by Öhlund et al. [2014]. The precipitate size as measured by APT is based on the APT atom count for each precipitate[†]. The KWN model predicts that 0.27% of the equilibrium volume fraction of TiC forms and that the average TiC precipitate radius is 1.38 nm after 60 minutes of isothermal tempering at 550 °C. Furthermore, the model predicts that nucleation of TiC precipitates starts during the heating stage, 10 seconds before reaching the isothermal temperature of 550 °C and that the peak in number density of TiC-precipitates is reached after 385 seconds (after 4 minutes and 7 seconds of isothermal annealing). The predicted average radius and size distribution from the KWN model are slightly higher than the values measured by APT. However, the measured precipitates sizes fall within the nonzero part of the predicted distribution and is therefore in agreement with the model. The predicted volume fraction of formed TiC-precipitates is lower than what is measured by APT. This could be due to the small sample size inherent to APT.

[†]We convert the atom count to a radius, assuming spherical precipitates, by the volume estimated from the lattice parameter of TiC. We add the distance of one Ti atom radius to the calculated radius as the volume estimated by the lattice parameters only measure to the centre of the outer atoms.

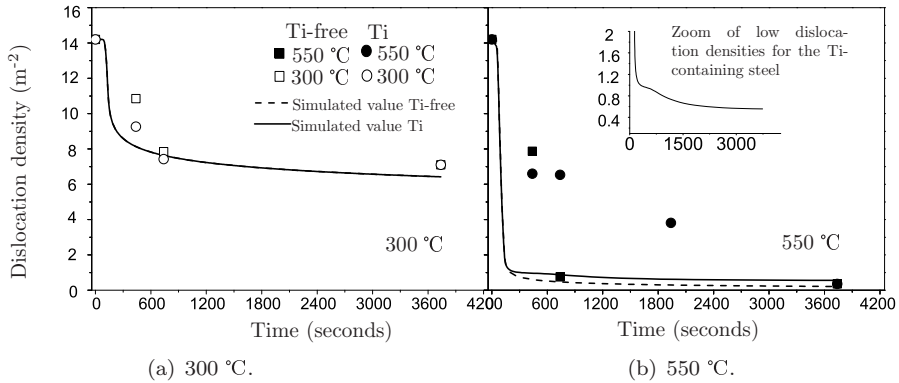


Figure 4.4: *The measured and the simulated dislocation density in Ti-free and Ti-containing steel as a function of annealing time during annealing at (a) 300 °C and (b) 550 °C.*

Figure 4.4 shows the dislocation density as a function of tempering time for Ti-free (precipitate free) and Ti-containing steel at different temperatures, as simulated via Equations (4.6) and (4.7) and as measured by EBSD experiments [Öhlund et al., 2014]. We use the simulated dislocation density as input to our model. The simulation of the evolution of the dislocation density does not take into consideration the pinning of dislocations by small iron carbides and cementite particles. We observe that these type of particles are present in the steels after quenching and at all annealing times. The pinning of dislocations by iron carbides is therefore expected to be approximately constant throughout the annealing of the steels and our simulation might overestimate the amount of recovery which has occurred at times between 5 to 60 minutes of isothermal tempering.

Figure 4.4(a) shows the dislocation density of Ti-free and Ti-containing martensite during tempering at 300 °C (where no TiC precipitates are present). We observe that the evolution of the recovery is slightly faster in the simulated values than in the experimental values and that the simulation slightly overestimates the degree of recovery. Figure 4.4(b) shows the dislocation density of Ti-free and Ti-containing martensite during tempering at 550 °C. We observe that the simulated and the experimental values do not correlate. The simulation of recovery in the Ti-containing steel shows faster recovery and a much higher degree of recovery than the measured values. However, we observe a recovery delay in the simulated values, with a maximum delay effect between 200 and 550 seconds of tempering. We note that the recovery delay of the simulated dislocation density and the recovery delay observed by experiments show a similar evolution in time (see the zoomed in panel). The recovery delay of the simulations of the Ti-containing steel at 550 °C results in a slightly higher dislocation density in the Ti-containing steel than in the Ti-free steel during isothermal annealing at 550 °C. This slightly higher dislocation density of the Ti-containing steel is not present in the experimental results.

The recovery delay of the simulated dislocation density is a result of the high number density of TiC precipitates which are present at that time. The KWN model predicts that the highest number of TiC precipitates, which can act as pinning points

spread in cementite particle size increases with annealing time (see Figure 4.1).

The strengthening effect of dislocations decreases very rapidly by approx. 200 HV during the 138 seconds of heating to the isothermal annealing temperature. This rapid decrease is a result of the rapid recovery which is shown in Figure 4.4(b). The strengthening effect of dislocations stabilises during tempering. Our hardness model predicts that the hardness contribution of dislocations is approximately stable at 54 HV from 10 to 60 minutes of isothermal tempering at 550 °C.

The micro-structural components which give minor direct contributions to the overall hardness of martensite are 1) Ti atoms in solid solution and 2) TiC, as shown in Figure 4.5.

The strengthening mechanism due to Ti in solid solution increases slightly during heating up and the first minutes of isothermal tempering at 550 °C and is thereafter stable. The hardness increases slightly due to a slight increase in the concentration of Ti atoms in the matrix as a result of formation of Fe₃C which redistributes a high number of Fe and C atoms from the matrix to Fe₃C. ThermoCalc simulations show that Ti does not dissolve in Fe₃C and is therefore remaining in the matrix. Our hardness model predicts that the hardness contribution due to Ti in solid solution is approximately 25 HV after 60 minutes of isothermal tempering at 550 °C.

The strengthening effect of TiC precipitates is zero during the majority of the heating up of the steel, and is thereafter increasing rapidly during the first 7 minutes of isothermal tempering at 550 °C. After 8 minutes of isothermal tempering the hardness increases slowly. The hardness model predicts that the strengthening effect due to precipitation strengthening of TiC is approximately 3.5 HV after 60 minutes of isothermal tempering at 550 °C. We note that the theoretical maximum precipitation strengthening effect of TiC is 42 HV.

The direct strengthening effect of Mn atoms in solid solution is zero during the entire process of tempering, as shown in Figure 4.5.

The micro-structural components which give combined contributions to the overall hardness of martensite are TiC precipitates combined with dislocations.

Our model predicts that the recovery process in the Ti containing steel is delayed during isothermal tempering at 550 °C as a result of TiC precipitates which pin dislocations (see Figure 4.4(b)). The resulting dislocation density of the Ti containing steel is therefore higher than the dislocation density of the Ti-free steel. This higher dislocation density contributes to a 20 HV higher hardness contribution in the Ti-containing steel after 60 minutes of isothermal tempering at 550 °C, as compared to the Ti-free steel. The total strength contribution due to formation of TiC in martensite is therefore the sum of the TiC precipitation strengthening effect, and the extra dislocation strengthening effect due to less recovery. Our hardness model predicts that this combined strengthening effect is 23.5 HV after 60 minutes of isothermal tempering at 550 °C.

The low strengthening effect of TiC-precipitates is a result of the low volume fraction of TiC-precipitates that is predicted by our model. We note that when the model is run for longer holding times at 550 °C, there is only a slight increase in the volume fraction of formed TiC-precipitates. The resulting hardness increase is small: 5.9 HV after three hours of isothermal annealing at 550 °C. An extended heat-treatment time will therefore not improve the properties of the martensite by much.

The low volume fraction of TiC-precipitates is related to the large misfit strain

Modified input parameter	$f_{\text{TiC}}/f_{\text{TiC}}^{\text{eq}}$	LSQ-error	Δg_s
None	0.27%	793	1.3359 GJ/m ³
Capture radius $2r_c$	0.28%	788	1.3347 GJ/m ³
Experimental dislocation density	0%	4.16×10^4	2.3189 GJ/m ³
$\Delta g_s=1.0019$ GJ/m ³	17%	973	-
Experimental dislocation density and $\Delta g_s=1.3359$ GJ/m ³	45%	1.34×10^9	-

Table 4.3: Results from least squares fitting of the model using modified input parameters after 60 minutes of tempering at 550 °C.

(1.3359 GJ/m³) that we find during fitting and the low density of potential nucleation sites (Equation (4.14)) that we use as input parameter to the model. Both factors reduce the nucleation rate. The low density of potential nucleation sites is a result of the rapid recovery of the simulated dislocation density which is used as an input to our model, and the calculated capture radius.

We investigate the influence of a higher number of available nucleation sites by repeating the fitting of our model to the measured hardness at 550 °C, using 1) an increased capture radius of $2r_c$, as calculated by Equation (4.15) and 2) a higher dislocation density within the martensite. To increase the dislocation density we use the experimental dislocation density as input to our model, instead of simulating the dislocation density. We also investigate the effect of lower misfit strain by setting a fixed value of the misfit strain (75% of the value predicted by our fit to the measured hardness) as input parameter to the model. We investigate the effect of a lower misfit strain energy combined with a higher number of available nucleation sites, by setting the misfit strain energy to 1.3359 GJ/m³ and using the experimental dislocation density as input parameters to the KWN model. The results from the repeated fit of our model and the accuracy of the simulated values to the measured hardness (given as the sum of squared errors) are given in Table 4.3, together with the values from our original fitting.

An increased capture radius does not generate a higher volume fraction of TiC-precipitates, but it slightly increases the fitting of the model. Increasing the dislocation density results in a higher value for the misfit strain energy after fitting. The model predicts that no nucleation of TiC-precipitates takes place. A reduction of the misfit strain energy results in a higher volume fraction of formed TiC, and a slight reduction of the accuracy of the fit. A reduction of the misfit strain energy and a higher dislocation density results in a significantly increased volume fraction of TiC-precipitates and a smaller average precipitate size. The latter results are more in agreement with the APT measurement. However, the model is no longer capable of fitting to the measured hardness.

4.7 Conclusions

We have quantified the evolution of the multiple hardness contributions to the overall hardness of martensite containing TiC-precipitates during isothermal annealing, by simulating the hardness of martensite as a linear addition of multiple hardening

mechanisms. This hardness model is combined with a micro-structural model based on the Kampmann-Wagner-Numerical (KWN) approach for a multi-component and multi-phase system to simulate the nucleation and growth of TiC-precipitates.

The two micro-structural components which contribute most to the overall hardness of the investigated Fe-C-Mn-Ti steel are Fe₃C precipitates (88 HV) and dislocations (54 HV). Both contributions decrease rapidly during initial stages of annealing and stabilise after 10 minutes of annealing. The addition of titanium to the steel gives a minor hardness contribution via Ti-atoms in solid solution and TiC precipitates. Ti atoms in solid solution give a hardness contribution which increases slightly during the first minutes of annealing and thereafter remains stable (at 25 HV). The direct contribution of TiC precipitates to the overall hardness is limited (3.5 HV). However, TiC-precipitates also contribute to the overall hardness by pinning of dislocations during the recovery that takes place during the tempering. The model predicts that only a small volume fraction of TiC-precipitates forms during isothermal annealing at 550 °C due to the large misfit strain (1.3359 GJ/m³) and the low density of potential nucleation sites.

Bibliography

- H.I. Aaronson, M. Enomoto and J.K. Lee. Mechanisms of Diffusional Phase Transformations in Metals and Alloys. CRC Press, Boca Raton, FL, United States of America, 2010.
- F. Abe, M. Taneike and K. Sawada. Alloy design of creep resistant 9Cr steel using a dispersion of nano-sized carbonitrides. International Journal of Pressure Vessels and Piping, 84(1–2):3–12, 2007.
- T. N. Baker. Processes, microstructure and properties of vanadium microalloyed steels. Materials Science and Technology, 25(9):1083–1107, 2009.
- J.W. Cahn. The kinetics of grain boundary nucleated reactions. Acta Metallurgica, 4(5):449–459, 1956.
- R.N. Caron and G. Krauss. The tempering of Fe-C lath martensite. Metallurgical Transactions, 3(9):2381–2389, 1972.
- L. Cheng, C.M. Brakman, B.M. Korevaar and E.J. Mittemeijer. The tempering of iron- carbon martensite; dilatometric and calorimetric analysis. Metallurgical Transactions A, 19(10):2415–2426, 1988.
- L.H. Friedman and D.C. Chrzan. Scaling Theory of the Hall-Petch Relation for Multilayers. Physical Review Letters, 81:2715–2718, 1998.
- T. Gladman. The Physical Metallurgy of Microalloyed Steels. Maney Publishing, 1997.
- Y. Han, J. Shi, L. Xu, W.Q. Cao and H. Dong. TiC precipitation induced effect on microstructure and mechanical properties in low carbon medium manganese steel. Materials Science and Engineering: A, 530(0):643–651, 2011.

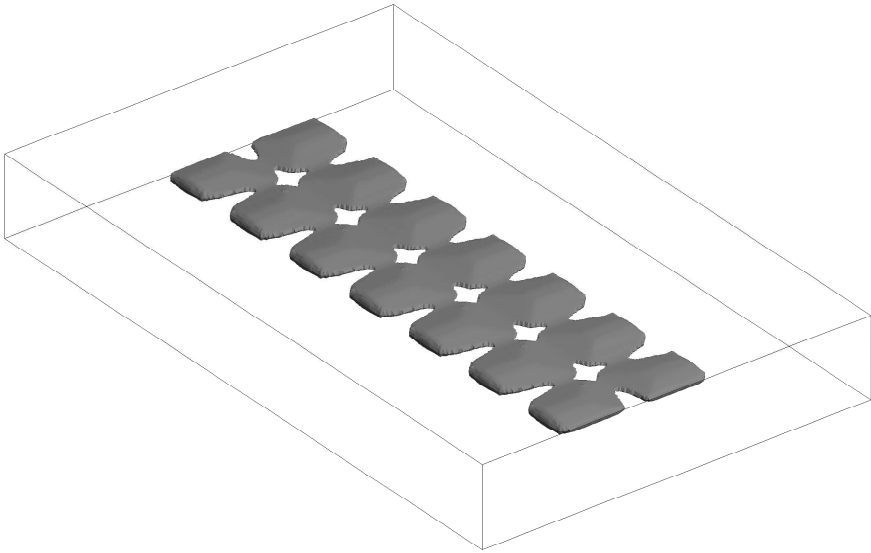
- S.Y. Hu and L.Q. Chen. Solute segregation and coherent nucleation and growth near a dislocation – a phase-field model integrating defect and phase microstructures. Acta Materialia, 49(3):463–472, 2001.
- B. Hutchinson, J. Hagström, O. Karlsson, D. Lindell, M. Tornberg, F. Lindberg and M. Thuvander. Microstructures and hardness of as-quenched martensites (0.1–0.5C). Acta Materialia, 59(14):5845–5858, 2011.
- ISO 898-1. Mechanical properties of fasteners made of carbon steel and alloy steel – Part 1: Bolts, screws and studs with specified property classes – Coarse thread and fine pitch thread. International Organization for Standardization, Geneva, Switzerland, 5th edition, 2013.
- J.H. Jang, C.-H. Lee, Y.-U. Heo and D.-W. Suh. Stability of (Ti,M)C (M=Nb, V, Mo and W) carbide in steels using first-principles calculations. Acta Materialia, 60(1):208–217, 2012.
- G. Krauss. Martensite in steel: strength and structure. Materials Science and Engineering: A, 273–275:40–57, 1999.
- R. Lagneborg and B. Bergman. The stress/creep rate behaviour of precipitation-hardened alloys. Metal Science, 10(1):20–28, 1976.
- R.J. LeVeque. Finite Volume Methods for Hyperbolic Problems (Cambridge Texts in Applied Mathematics). Cambridge University Press, United Kingdom of Great Britain and Northern Ireland, 2002.
- S. Morito, J. Nishikawa and T. Maki. Dislocation Density within Lath Martensite in Fe-C and Fe-Ni Alloys. ISIJ International, 43(9):1475–1477, 2003.
- S. Morito, X. Huang, T. Furuhashi, T. Maki and N. Hansen. The morphology and crystallography of lath martensite in alloy steels. Acta Materialia, 54(19):5323–5331, 2006.
- Y. Namimura, N. Ibaraki, W. Urushihara and T. Nakayama. Development of steels for high-strength bolts with excellent fracture resistance. Wire Journal International, 36:62–67, 2003.
- L.-Å. Nordström. On the Yield Strength of Quenched Low-Carbon Lath Martensite. Scandinavian Journal of Metallurgy, 5:159–165, 1976.
- C.E.I.C. Öhlund, J. Weidow, M. Thuvander and S.E. Offerman. Effect of Ti on evolution of microstructure and hardness of martensitic Fe-C-Mn steel during tempering. ISIJ International, 54, 2014. IN PRESS.
- T. Ohmura, K. Tsuzaki and S. Matsuoka. Nanohardness measurement of high-purity Fe-C martensite. Scripta Materialia, 45(8):889–894, 2001.
- G.B. Olson and W.S. Owen. Martensite. A Tribute to Morris Cohen. ASM International, 1992.

- D. den Ouden, L. Zhao, C. Vuik, J. Sietsma and F.J. Vermolen. Modelling precipitate nucleation and growth with multiple precipitate species under isothermal conditions: Formulation and analysis. Computational Materials Science, 79:933–943, 2013.
- M. Perez. Gibbs-Thomson effects in phase transformations. Scripta Materialia, 52(8):709–712, 2005.
- D.A. Porter and K.E. Easterling. Phase Transformations in Metals and Alloys. Chapman & Hall, London, United Kingdom of Great Britain and Northern Ireland, 2nd edition, 1992.
- D. S. Rickerby. Lattice parameters of iron-titanium solid solutions. Metal Science, 16(10):495–496, 1982.
- J.M. Rosenberg and H.R. Piehler. Calculation of the taylor factor and lattice rotations for bcc metals deforming by pencil glide. Metallurgical Transactions, 2(1):257–259, 1971.
- A. Sawahata, M. Enomoto, K. Okuda and T. Yamashita. Simulation of TiC Precipitation in Ti-added Low Carbon Steel. Tetsu-to-Hagane, 94(1):21–29, 2008.
- Y. Shima, Y. Ishikawa, H. Nitta, Y. Yamazaki, K. Mimura, M. Isshiki and Y. Iijima. Self-Diffusion along Dislocations in Ultra High Purity Iron. Material Transactions, 43(2):173–177, 2002.
- A. Smith, H. Luo, D.N. Hanlon, J. Sietsma and S. van der Zwaag. Recovery Processes in the Ferrite Phase in C-Mn Steel. ISIJ International, 44(7):1188–1194, 2004.
- G.R. Speich, A.J. Schwoeble and W.C. Leslie. Elastic constants of binary iron-base alloys. Metallurgical Transactions, 3(8):2031–2037, 1972.
- M. Taneike, N. Fujitsuna and F. Abe. Improvement of creep strength by fine distribution of TiC in 9Cr ferritic heat resistant steel. Materials Science and Technology, 20(11):1455–1461, 2004.
- A. Teresiak and H. Kubsch. X-ray investigations of high energy ball milled transition metal carbides. Nanostructured Materials, 6(5–8):671–674, 1995.
- Z. Wang, X. Mao, Z. Yang, X. Sun, Q. Yong, Z. Li and Y. Weng. Strain-induced precipitation in a Ti micro-alloyed {HSLA} steel. Materials Science and Engineering: A, 529:459–467, 2011.
- Z.M. Wang and G.J. Shiflet. Growth of δ' on dislocations in a dilute Al-Li alloy. Metallurgical and Materials Transactions A, 29(8):2073–2085, 1998.
- F.-G. Wei, T. Hara, T. Tsuchida and K. Tsuzaki. Hydrogen Trapping in Quenched and Tempered 0.42C-0.30Ti Steel Containing Bimodally Dispersed TiC Particles. ISIJ International, 43(4):539–547, 2003.
- S.Q. Xiao and P. Haasen. A model for the nucleation of a spherical coherent precipitate near an edge dislocation. Scripta Metallurgica, 23(3):365–370, 1989.

-
- C. Zener. Theory of growth of spherical precipitates from solid solution. Journal of Applied Physics, 20(10):950–953, 1949.
- H.S. Zurob, C.R. Hutchinson, Y. Brechet and G. Purdy. Modeling recrystallization of microalloyed austenite: effect of coupling recovery, precipitation and recrystallization. Acta Materialia, 50:3075–3092, 2002.

Part II

Interfaces



Chapter 5

A Fully Finite-Element Based Level-Set Method

5.1 Introduction

Several models that describe the nucleation and growth of precipitates in alloys have been proposed in the last decades, see for example Deschamps and Brechet [1999], Kampmann and Wagner [1991], Ouden et al. [2011], Robson [2004], Soisson et al. [1996], Vermolen et al. [2007]. A drawback of the majority of these models is the assumption of a predefined, such as spherical, shape for the precipitates. These precipitate geometries include cuboids, needles, plates and other shapes. Modelling the growth and dissolution of arbitrarily-shaped precipitates is the subject of this chapter. We also focus on the effect of various physical properties on the growth/dissolution process, such as interfacial tension and reaction and diffusion rates.

Various models exist in literature for the description of the growth of precipitates within a diffusive domain. The phase field method (See for example Hu and Henager Jr. [2009]) considers the interface between the two phases as a smooth interface, where the evolution of the interface is governed by the minimisation of the free energy of the entire system. The Kampmann-Wagner-Numerical method, introduced in Kampmann and Wagner [1991], models a complete statistical distribution of precipitates, in which the precipitates are assumed spherical and growth is modelled using a Zener approximation Zener [1949]. The Monte Carlo method has also been used to model the nucleation and growth of precipitates Soisson et al. [1996], in which the behaviour

This chapter is based on the article:

D. den Ouden, A. Segal, F.J. Vermolen, L. Zhao, C. Vuik and J. Sietsma. Application of the level-set method to a mixed-mode driven stefan problem in 2D and 3D. *Computing*, 95(1): 553–572, 2013a,

and additional work.

of the precipitates follows from the behaviour of single atoms. In Vermolen et al. [2007] the moving mesh method is used to model the topological changes associated with the growth and dissolution of precipitates using an explicit representation of the interface. Finally the level-set method Osher and Sethian [1988] has been applied, which uses a sharp interface representation and which can handle topological changes of the precipitate with ease.

In this chapter we first give a short overview of the moving boundary model used for the description of growth and dissolution of precipitates in a binary alloy. Subsequently, we discuss some numerical aspects of our approach and finally we discuss the results obtained with our method regarding convergence and the dependence of the model on the physical parameters.

5.2 The Stefan Problem

In this section, we describe the models used to simulate the dissolution and growth of a precipitate in a diffusive phase driven by a single chemical element. The level-set method introduced in Osher and Sethian [1988] is used for the description of the boundary, whereas diffusive and reactional fluxes physically determine the movement of the interface.

5.2.1 Evolution of the Concentration

Our model is based on the original Stefan problem described by Jožef Stefan in 1890 (see Vuik [2013]). Consider a diffusive phase $\Omega_D(t)$ in which a precipitate $\Omega_P(t)$ has nucleated at some point. Here $\Omega_D(t)$ and $\Omega_P(t)$ are open domains. Let $\Gamma(t)$ denote the interface between the two aforementioned phases, which represents the moving boundary in our model. Let the concentration c_p within the precipitate $\Omega_P(t)$ be fixed and assume the concentration $c(\mathbf{x}, t)$ within the diffusive phase $\Omega_D(t)$ to be described by the standard diffusion equation

$$\frac{\partial c}{\partial t}(\mathbf{x}, t) = \nabla \cdot (D(\mathbf{x}, t) \nabla c(\mathbf{x}, t)), \quad \text{for } \mathbf{x} \in \Omega_D(t), t > 0, \quad (5.1)$$

where D is the diffusivity of the diffusing chemical element. At the outer boundary of Ω_D , i.e. $\partial\Omega_D(t) \setminus \Gamma(t)$, we assume a no-flux condition, which results into a homogeneous Neumann boundary condition. Furthermore, let $\Omega(t)$ be the open domain defined by

$$\Omega(t) = \Omega_D(t) \cup \Omega_P(t) \cup \Gamma(t). \quad (5.2)$$

At the precipitate/matrix interface $\Gamma(t)$ three physical phenomena occur in sequence during dissolution:

1. Detachment of atoms from the lattice structure of the precipitate phase;
2. Crossing of atoms from within the precipitate into the matrix;
3. Long-distance diffusion of atoms into the matrix.

These phenomena occur during growth in the reverse order. In both cases all phenomena put restrictions on the speed at which the interface can move. Many models assume that the diffusive phenomenon is rate-limiting and hence neglect the possible influence of the reaction at the interface given by the first two phenomena. In Vermolen [2007] it has been shown for a plate-like precipitate that the interface reaction can have a significant impact on the dissolution kinetics. Similar to the model in Vermolen [2007], we model the flux of atoms $J_r(\mathbf{x}, t)$ across the interface by a first-order reaction:

$$J_r(\mathbf{x}, t) = K(\mathbf{x}, t) (c_s(\mathbf{x}, t) - c(\mathbf{x}, t)), \quad \text{for } \mathbf{x} \in \Gamma(t), t > 0. \quad (5.3)$$

The flux at the interface within the diffusive phase $\Omega_D(t)$ consists of two parts, the flux $J_m(\mathbf{x}, t)$ due to movement of the interface itself

$$J_m(\mathbf{x}, t) = c(\mathbf{x}, t)v_n(\mathbf{x}, t), \quad \text{for } \mathbf{x} \in \Gamma(t), t > 0, \quad (5.4)$$

and the diffusive flux $J_d(\mathbf{x}, t)$

$$J_d(\mathbf{x}, t) = D(\mathbf{x}, t) \frac{\partial c}{\partial n}(\mathbf{x}, t), \quad \text{for } \mathbf{x} \in \Gamma(t), t > 0. \quad (5.5)$$

In these definitions $K(\mathbf{x}, t)$ is the interface-reaction speed, $c_s(\mathbf{x}, t)$ the local equilibrium concentration and $v_n(\mathbf{x}, t)$ denotes the speed of the interface in the outward normal direction $\mathbf{n}(\mathbf{x}, t)$ from the domain $\Omega_D(t)$ at $\Gamma(t)$. Combining Equations (5.3), (5.4) and (5.5), we arrive at the flux boundary condition

$$K(\mathbf{x}, t) (c_s(\mathbf{x}, t) - c(\mathbf{x}, t)) = D(\mathbf{x}, t) \frac{\partial c}{\partial n}(\mathbf{x}, t) + c(\mathbf{x}, t)v_n(\mathbf{x}, t), \quad (5.6)$$

for $\mathbf{x} \in \Gamma(t), t > 0$.

As we have introduced a new unknown, the interface velocity $v_n(\mathbf{x}, t)$, we must complete our definition by another boundary condition on $\Gamma(t)$. Using a mass balance on a growing/dissolving precipitate, we arrive at the classical Stefan condition

$$c_p v_n(\mathbf{x}, t) = D \frac{\partial c}{\partial n}(\mathbf{x}, t) + c(\mathbf{x}, t)v_n(\mathbf{x}, t), \quad \text{for } \mathbf{x} \in \Gamma(t), t > 0. \quad (5.7)$$

By subtracting Equation (5.7) from Equation (5.6) we see that the interface velocity $v_n(\mathbf{x}, t)$ is given by

$$v_n(\mathbf{x}, t) = \frac{K(\mathbf{x}, t)}{c_p} (c_s(\mathbf{x}, t) - c(\mathbf{x}, t)), \quad \text{for } \mathbf{x} \in \Gamma(t), t > 0, \quad (5.8)$$

Substituting the above result in either Equation (5.6) or (5.7), yields that the normal diffusive flux at the interface is given by

$$D(\mathbf{x}, t) \frac{\partial c}{\partial n}(\mathbf{x}, t) = \frac{K(\mathbf{x}, t)}{c_p} (c_s(\mathbf{x}, t) - c(\mathbf{x}, t)) (c_p - c(\mathbf{x}, t)), \quad (5.9)$$

for $\mathbf{x} \in \Gamma(t), t > 0$.

From Equation (5.8), we see that the determination of the interface velocity does not involve computing the normal diffusive fluxes at the interface, as opposed to

the model used in for example Javierre [2006]. A drawback is the introduction of a nonlinear boundary condition on $\Gamma(t)$ for the diffusion problem, in contrast to the simpler Dirichlet condition

$$c(\mathbf{x}, t) = c_s(\mathbf{x}, t), \quad \text{for } \mathbf{x} \in \Gamma(t), t > 0, \quad (5.10)$$

used in for example Javierre [2006]. Inspection of Equation (5.8) shows that if the value of K is large, we will have fast dissolution/growth of the precipitate, indicating diffusion controlled kinetics, whereas a lower value of K leads to slow dissolution/growth, indicating reaction-controlled kinetics.

In this chapter we assume that the solubility of the considered element at the precipitate/matrix interface inside the diffusive phase, $c_s(\mathbf{x}, t)$, is known and modelled using the Gibbs-Thomson effect [Perez, 2005, Porter and Easterling, 1992]

$$c_s(\mathbf{x}, t) = c_s^\infty(t) \exp(\zeta \kappa(\mathbf{x}, t)), \quad (5.11)$$

where $c_s^\infty(t)$ is the solubility of the considered element, ζ a positive physical factor and $\kappa(\mathbf{x}, t)$ the sum of the principle curvatures of the interface $\Gamma(t)$. The solubility $c_s^\infty(t)$ can be derived from thermodynamic databases such as ThermoCalc [Andersson et al., 2002]. The parameter ζ is defined by

$$\zeta = \frac{\gamma V_m}{R_g T}, \quad (5.12)$$

with γ the interface energy, V_m the molar volume of the precipitate, R_g the gas constant and T the temperature. For a sphere the derivation of Equation (5.11) can be found in Perez [2005], leading to $\kappa=2/R$ where R is the radius of the sphere. By Equation (5.11) the equilibrium concentration c_s^∞ increases for locally convex interfaces, which have positive curvature, and decreases for locally concave interfaces, which have negative curvature. This amplification/dampening will cause the precipitate to grow/dissolve to the configuration with the lowest overall surface tension, i.e. the total energy of the system will be minimised [Mullins and Sekerka, 1963].

5.2.2 The Level-Set Method

In Osher and Sethian [1988] the level-set method was introduced, which captures the motion of an arbitrary interface using a signed-distance function. Since we are interested in the movement of the precipitate/matrix interface $\Gamma(t)$, we employ this method to describe the interface. Define the signed-distance function $\phi(\mathbf{x}, t)$ by

$$\phi(\mathbf{x}, t) = \begin{cases} + \min_{\mathbf{y} \in \Gamma(t)} \|\mathbf{y} - \mathbf{x}\|_2 & \text{if } \mathbf{x} \in \bar{\Omega}_P(t) \setminus \Gamma(t), \\ 0 & \text{if } \mathbf{x} \in \Gamma(t), \\ - \min_{\mathbf{y} \in \Gamma(t)} \|\mathbf{y} - \mathbf{x}\|_2 & \text{if } \mathbf{x} \in \bar{\Omega}_D(t) \setminus \Gamma(t). \end{cases} \quad (5.13)$$

Using this definition of $\phi(\mathbf{x}, t)$, the normal $\mathbf{n}(\mathbf{x}, t)$ of the interface $\Gamma(t)$ can be calculated directly from $\phi(\mathbf{x}, t)$ by

$$\mathbf{n}(\mathbf{x}, t) = \frac{\nabla \phi(\mathbf{x}, t)}{\|\nabla \phi(\mathbf{x}, t)\|_2}, \quad (5.14)$$

which points into $\Omega_P(t)$ and out of $\Omega_D(t)$ due to our chosen orientation of $\phi(\mathbf{x}, t)$. Equation (5.11) uses the sum of the principal curvatures $\kappa(\mathbf{x}, t)$, which can be derived from $\phi(\mathbf{x}, t)$, similar to the normal $\mathbf{n}(\mathbf{x}, t)$, using

$$\kappa(\mathbf{x}, t) = -\nabla \cdot \frac{\nabla \phi(\mathbf{x}, t)}{\|\nabla \phi(\mathbf{x}, t)\|_2}. \quad (5.15)$$

Note that we introduced a minus sign in the definition of $\kappa(\mathbf{x}, t)$ as opposed to the definition introduced in Osher and Sethian [1988] due to the sign of our signed-distance function $\phi(\mathbf{x}, t)$. The movement of the interface is captured by evolving the signed-distance function $\phi(\mathbf{x}, t)$ using the convection equation [Osher and Fedkiw, 2002]

$$\frac{\partial \phi}{\partial t}(\mathbf{x}, t) + v_n^{\text{ex}}(\mathbf{x}, t) \|\nabla \phi(\mathbf{x}, t)\|_2 = 0, \quad \text{for } \mathbf{x} \in \Omega, t > 0. \quad (5.16)$$

The velocity $v_n^{\text{ex}}(\mathbf{x}, t)$ in Equation (5.16) is an extension of the normal interface velocity $v_n(\mathbf{x}, t)$ given by Equation (5.8). Various approaches exist for this extension routine, see for example Chen et al. [1997], Osher and Fedkiw [2002], which are based on the evolution of convection equations in pseudo-time and a Dirichlet condition on the interface. We however choose to use a simpler approach to reduce the computational effort needed for this extension. We solve the Laplace equation

$$\Delta v_n^{\text{ex}}(\mathbf{x}, t) = 0, \quad \text{for } \mathbf{x} \in \Omega(t) \setminus \Gamma(t), t > 0, \quad (5.17)$$

with a homogeneous Neumann boundary condition on $\partial\Omega(t)$ and the Dirichlet condition

$$v_n^{\text{ex}}(\mathbf{x}, t) = v_n(\mathbf{x}, t), \quad \text{for } \mathbf{x} \in \Gamma(t), t > 0, \quad (5.18)$$

where $v_n(\mathbf{x}, t)$ is given by Equation (5.8).

In Sussman et al. [1994] it has been shown that advancing fronts are only captured correctly if the function $\phi(\mathbf{x}, t)$ remains a signed-distance function throughout the simulations. To enforce this constraint, we employ the technique of reinitialisation. Various reinitialisation techniques have been developed which either use a partial differential equation or a front marching technique (see for an overview Sethian [1999], Sussman et al. [1994]). In this chapter we will use another approach, which will be explained in the next section.

5.3 Numerical Methodology

Both Equation (5.1) and Equation (5.16) are solved using finite-element techniques. For Equation (5.1), we employ the standard Galerkin finite-element technique, whereas for Equation (5.16) we use a SUPG finite-element technique, which is in detail discussed in Tornberg and Engquist [2000]. We have chosen this SUPG stabilisation, as the stabilisation parameter is dependent on the time-step and the current convection speed and direction of ϕ . No artificial parameters need to be chosen in this SUPG technique. We combine this discretisation scheme with the Explicit-Euler

time-integration for the signed-distance function $\phi(\mathbf{x}, t)$ and the Implicit-Euler time-integration for the concentration $c(\mathbf{x}, t)$. The extension of the normal velocity with Equation (5.17) is done using the standard Galerkin finite-element technique. All finite-element techniques are applied on meshes with linear elements, of which the generation will be discussed next. After this we discuss the discretisation of Equation (5.1) and the reinitialisation of the level-set function ϕ in more detail. Finally an overview of the entire algorithm is presented.

5.3.1 Mesh Generation

To solve the problem formulated above, we generate several meshes in order to deal with the moving interface. The approach taken to construct these meshes in $2D$ is given here, but is readily extended to $3D$ (see for example Javierre [2006]). First we define a background mesh \mathcal{T} on which we assume that a finite-element approximation $\phi(t^n)$ at the discrete time t^n is known. Figure 5.1(a) shows such a $2D$ mesh including the zero-level of $\phi(t^n)$ and the classification of the domains. Let \mathcal{X} denote all points from the background mesh \mathcal{T} and \mathcal{E} the set of edges from \mathcal{T} .

Upon inspection of Equations (5.17) and (5.18), we see that in order to determine the velocity $\mathbf{v}_n^{ex}(t^n)$, a Dirichlet boundary condition must be applied on the interface $\Gamma(t^n)$, which is embedded in the domain $\Omega(t)$. Analysis of Equations (5.1) to (5.9) gives that a restriction of \mathcal{T} to $\Omega_D(t^n)$ and boundary elements that represent the interface $\Gamma(t^n)$ are needed. To introduce the restrictions, we introduce two new meshes, \mathcal{T}_E^n and \mathcal{T}_D^n . The background mesh \mathcal{T} is enriched with nodes on the interface $\Gamma(t^n)$ and explicitly contains edges on the interface $\Gamma(t^n)$, giving the enriched mesh \mathcal{T}_E^n . The mesh \mathcal{T}_D^n is based on the enriched mesh \mathcal{T}_E^n , and only contains those triangles that are located within $\Omega_D(t^n)$.

We introduce $\mathcal{E}^\pm \subset \mathcal{E}$ to represent the edges of the background mesh \mathcal{T} over which $\phi(t^n)$ changes sign, as the zero-level of $\phi(t^n)$, and consequently $\Gamma(t^n)$, must be located along such an edge. Using our linear approximation of the level-set function $\phi(\mathbf{x}, t^n)$ on each edge, we define the local variable τ^e for each edge $e \in \mathcal{E}^\pm$ as

$$\tau^e = \frac{-\phi_1^e(t^n)}{\phi_2^e(t^n) - \phi_1^e(t^n)}, \quad (5.19)$$

where $\phi_i^e(t^n)$, $i = 1, 2$ represent the values of the first and second point of the edge e over which $\phi(t^n)$ changes sign at t^n . Note that $\phi_1(t^n)\phi_2(t^n) < 0$. Using this variable we approximate the location \mathbf{x}^e of $\Gamma(t^n)$ along the edge e by

$$\mathbf{x}^e = (1 - \tau^e)\mathbf{x}_1^e + \tau^e\mathbf{x}_2^e, \quad (5.20)$$

with \mathbf{x}_i^e , $i = 1, 2$ the global locations of the first and second point of the edge e . If $\tau^e \in (\delta, 1 - \delta)$, where $0 \leq \delta \leq 1/2$, we add \mathbf{x}^e to the set \mathcal{X}^\pm , which represents the set[†] of points to be added to the mesh \mathcal{T} . If however $\tau^e \leq \delta$ we do not add \mathbf{x}^e to \mathcal{X}^\pm but set

$$\mathbf{x}_1^e = \mathbf{x}^e \quad \text{and} \quad \phi_1^e = 0, \quad (5.21)$$

[†]The \pm symbol represents the fact that the points in the set \mathcal{X}^\pm come from an edge over which $\phi(t^n)$ changes sign.

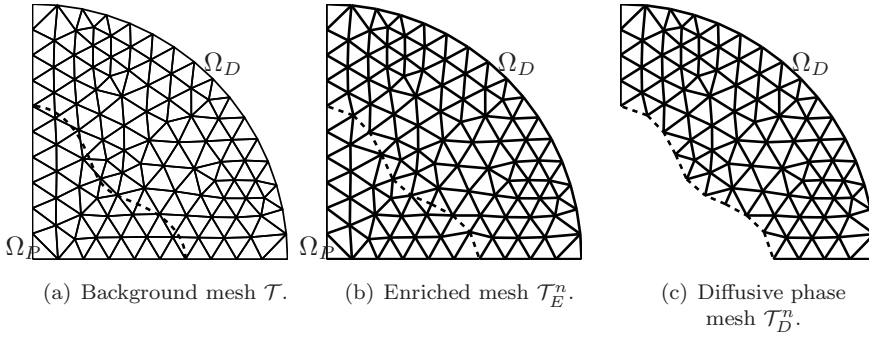


Figure 5.1: 2D examples of the generated meshes in our approach. The dashed curve corresponds to (a): the given/prescribed interface $\Gamma(t^n)$, (b),(c): the set of interface edges \mathcal{E}^0 . The value $\delta = 0.3$ has been used.

i.e. we shift an original mesh point of the background mesh to the interface $\Gamma(t^n)$, and if $\tau^e \geq 1 - \delta$, we apply the same principle by setting

$$\mathbf{x}_2^e = \mathbf{x}^e \quad \text{and} \quad \phi_2^e = 0. \quad (5.22)$$

If an original mesh point \mathbf{x} can be shifted to several locations, we choose the interface location \mathbf{x}^e closest to the mesh point \mathbf{x} . The next step in construction of the enriched mesh \mathcal{T}_E^n is the construction of the boundary elements. To this end, we define \mathcal{X}^0 as the union of all (possibly shifted) background points \mathcal{X} where $\phi(t^n) = 0$ and all points from \mathcal{X}^\pm . Next we construct a set of edges \mathcal{E}^0 through \mathcal{X}^0 , to approximate the interface $\Gamma(t^n)$. Finally we construct the enriched mesh \mathcal{T}_E^n on the union \mathcal{X}_E of the (possibly shifted) background points \mathcal{X} and the interface points \mathcal{X}^\pm , such that the set of edges \mathcal{E}^0 is present within the mesh. Figure 5.1(b) shows the enriched mesh \mathcal{T}_E^n with the edges \mathcal{E}^0 that results from applying this approach to the background mesh \mathcal{T} and interface $\Gamma(t^n)$ of Figure 5.1(a).

Construction of the mesh \mathcal{T}_D^n can easily be accomplished by noting that $\bar{\Omega}_D(t^n)$ can only contain those points where $\phi(t^n)$ is non-positive due to Equation (5.13). So after determination of those points in \mathcal{X}_E where $\phi(t^n)$ is positive, we delete any simplex from \mathcal{T}_E^n that uses at least one of those points. This leads to the diffusive phase mesh \mathcal{T}_D^n , which due to the derivation of the enriched mesh \mathcal{T}_E^n will contain boundary elements along $\Gamma(t^n)$. Figure 5.1(c) shows the diffusive phase mesh \mathcal{T}_D^n with the edges \mathcal{E}^0 that results from restricting the enriched mesh \mathcal{T}_E^n to $\bar{\Omega}_D(t^n)$. In this chapter we have chosen $\delta=0.3$.

5.3.2 Discretisation of Equation (5.1)

As mentioned above, we discretise Equation (5.1) combined with the boundary condition in Equation (5.9) using the standard Galerkin finite-element technique and Implicit-Euler time-integration. The finite-element technique transforms Equation (5.1) to a system of nonlinear ordinary differential equations

$$M(t) \frac{d\mathbf{c}(t)}{dt} = S(t, \mathbf{c}(t))\mathbf{c}(t) + \mathbf{f}(t, \mathbf{c}(t)), \quad (5.23)$$

where $\mathbf{c}(t)$ represents the finite-element approximation at time t . The mass matrix $M(t)$, the stiffness matrix $S(t, \mathbf{c}(t))$ and vector $\mathbf{f}(t, \mathbf{c}(t))$ contain integrals over the domain $\Omega_D(t)$ and the interface $\Gamma(t)$. Due to the non-linearity of Equation (5.9), which is used in the derivation of the weak formulation, we have a stiffness matrix $S(t, \mathbf{c}(t))$ and a vector $\mathbf{f}(t, \mathbf{c}(t))$ that depend on the solution vector $\mathbf{c}(t)$. The term

$$\frac{K(\mathbf{x}, t)}{c_p} (c_p - c(\mathbf{x}, t)), \quad (5.24)$$

of Equation (5.9) is incorporated in the matrix $S(t, \mathbf{c}(t))$ and the remaining term

$$-\frac{K(\mathbf{x}, t)}{c_p} (c_p - c(\mathbf{x}, t)) c_s(\mathbf{x}, t), \quad (5.25)$$

is incorporated in the vector $\mathbf{f}(t, \mathbf{c}(t))$.

Application of Implicit-Euler time-integration on Equation (5.23) leads to the matrix-vector equation

$$(M(t^{n+1}) - \Delta t S(t^{n+1}, \mathbf{c}^{n+1})) \mathbf{c}^{n+1} = M(t^{n+1}) \mathbf{c}^n + \Delta t \mathbf{f}(t^{n+1}, \mathbf{c}^{n+1}), \quad (5.26)$$

where the superscript n refers to the evaluation of the variable at the discrete time t^n and Δt is the chosen time step. Under the assumption that the diffusive phase mesh \mathcal{T}_D^n contains N^n points and since the time-consecutive meshes \mathcal{T}_D^n and \mathcal{T}_D^{n+1} can contain different numbers of points, i.e. $N^{n+1} \neq N^n$, we see a possible dimensional mismatch in the matrix-vector product between $M(t^{n+1})$ and \mathbf{c}^n .

To overcome this possible dimensional mismatch, we extend the solution \mathbf{c}^n from the mesh \mathcal{T}_D^n to the mesh \mathcal{T}_D^{n+1} . For any point $\mathbf{x}_i \in \mathcal{T}_D^{n+1}$, $i \in \{1, \dots, C^{n+1}\}$ we first find the point $\mathbf{y}_j \in \mathcal{T}_D^n$, $j \in \{1, \dots, C^n\}$ such that $\|\mathbf{x}_i - \mathbf{y}_j\|_2$ is minimal and define the index-to-index function $I : i \rightarrow j$. We then define the extended solution vector \mathbf{c}_{ex}^n of length C^{n+1} by setting

$$c_{\text{ex},i}^n = c_{I(i)}^n. \quad (5.27)$$

Note that if a point \mathbf{x}_i originates from the background mesh \mathcal{T} and has not been shifted in both diffusive phase meshes \mathcal{T}_D^n and \mathcal{T}_D^{n+1} , we have $\mathbf{x}_i = \mathbf{y}_{I(i)}$. Furthermore if $\mathcal{T}_D^{n+1} = \mathcal{T}_D^n$, we will have consistency as $\mathbf{x}_i = \mathbf{y}_{I(i)}$. Using the index-to-index function $I(i)$ we can also assign a mesh velocity $\mathbf{v}_i^{\text{mesh}}(t^{n+1})$ to each point $\mathbf{x}_i \in \mathcal{T}_D^{n+1}$, $i = 1, \dots, N^{n+1}$, which is given by the function

$$\mathbf{v}_i^{\text{mesh}}(t^{n+1}) = \frac{\mathbf{y}_{I(i)} - \mathbf{x}_i}{\Delta t}, \quad i = 1, \dots, N^{n+1}, \quad (5.28)$$

where $\mathbf{y}_{I(i)} \in \mathcal{T}_D^n$ for all i .

Using the above extension, we must replace the partial derivative with respect to time in Equation (5.1) with a material derivative. The material derivative is defined as

$$\frac{Dc}{Dt}(\mathbf{x}, t) = \frac{\partial c}{\partial t}(\mathbf{x}, t) + \frac{d\mathbf{x}}{dt}(t) \cdot \nabla c(\mathbf{x}, t), \quad (5.29)$$

which transforms Equation (5.1) to

$$\frac{Dc}{Dt}(\mathbf{x}, t) = \nabla \cdot (D(\mathbf{x}, t) \nabla c(\mathbf{x}, t)) + \frac{d\mathbf{x}}{dt}(t) \cdot \nabla c(\mathbf{x}, t), \quad (5.30)$$

for $\mathbf{x} \in \Omega_D(t)$, $t > 0$.

We approximate the velocity of a point $\mathrm{d}\mathbf{x}/\mathrm{d}t$ at time t^{n+1} with our derived mesh velocity of Equation (5.28) based on \mathcal{T}_D^n and \mathcal{T}_D^{n+1} . We note that this approach is similar to the approach used in Segal et al. [1998].

After application of the standard Galerkin finite-element technique and Implicit-Euler time-integration, we arrive at the natural fixed-point problem

$$\mathbf{c}^{n+1} = A(\mathbf{c}^{n+1})^{-1} \mathbf{g}(\mathbf{c}^{n+1}), \quad (5.31)$$

where the matrix A and vector g are defined by

$$A(\mathbf{q}) = M(t^{n+1}) - \Delta t S(t^{n+1}, \mathbf{q}), \quad (5.32)$$

$$\mathbf{g}(\mathbf{q}) = M(t^{n+1}) \mathbf{c}_{\mathrm{ex}}^n + \Delta t \mathbf{f}(t^{n+1}, \mathbf{q}), \quad (5.33)$$

and the matrix $S(t^{n+1}, \mathbf{q})$ now also contains the mesh velocity $\mathbf{v}^{\mathrm{mesh}}(t^{n+1})$. We solve this fixed-point problem using the fixed-point iteration

$$\begin{cases} \mathbf{c}_0^{n+1} &= \mathbf{c}_{\mathrm{ex}}^n, \\ \mathbf{c}_p^{n+1} &= A(\mathbf{c}_p^{n+1})^{-1} \mathbf{g}(\mathbf{c}_p^{n+1}), \quad p = 1, 2, 3, \dots \end{cases} \quad (5.34)$$

We iterate until the error ϵ has dropped below some predefined tolerance FPT , where the error ϵ is given by

$$\epsilon = \frac{\|\mathbf{c}_{p+1}^{n+1} - \mathbf{c}_p^{n+1}\|_\infty}{\|\mathbf{c}_{p+1}^{n+1}\|_\infty}. \quad (5.35)$$

In this chapter we have chosen $\mathrm{FPT} = 10^{-6}$. Using the fixed-point iterations we have observed a linear rate of convergence as expected.

Instead of the fixed-point problem in Equation (5.31) we could also have chosen to solve the equivalent root-finding problem

$$A(\mathbf{c}^{n+1}) \mathbf{c}^{n+1} - \mathbf{g}(\mathbf{c}^{n+1}) = 0, \quad (5.36)$$

with the same matrices and vectors. This problem can be solved by using for example a Newton-Raphson solver. We have not chosen for this approach, as it requires the determination of (an approximation of) the Jacobian, which for our model is complex or leads to multiple function evaluations per iteration, and thereby making each iteration more computationally expensive.

5.3.3 Reinitialisation

As shown in Sussman et al. [1994], it is necessary to maintain the signed-distance property of the level-set function $\phi(\mathbf{x}, t)$ during the computations. To this extent, the technique of reinitialisation has been introduced, which can be done in several ways Sethian [1999], Sussman et al. [1994]. We compared several methods and we have chosen to use an efficient direct approach in this research, which will be described next.

After obtaining the numerical solution $\tilde{\phi}^{n+1}$ on the enriched mesh \mathcal{T}_E^n by solving Equation (5.16), we map this solution back onto the background mesh \mathcal{T} . From this numerical solution we generate the enriched mesh \mathcal{T}_E^{n+1} , which will contain an explicit linear representation of the interface $\Gamma(t^{n+1})$ consisting of vertices and edges in $2D$

and vertices and triangles in $3D$. This representation can easily be used to recompute the distance between any point in the enriched mesh \mathcal{T}_E^{n+1} and the interface $\Gamma(t^{n+1})$. In the following paragraphs we assume that we are working in $3D$.

Denote by \mathcal{T}^0 the set of triangles describing the interface $\Gamma(t^n)$ through the interface points \mathcal{X}^0 and by \mathcal{E}^0 the edges defined by the triangulation \mathcal{T}^0 . For any point $\mathbf{x} \in \Omega$, the orthogonal projection on the plane defined by the triangle $\triangle ABC \in \mathcal{T}^0$ is given by

$$\mathbf{x}_{\triangle ABC}^p(\mathbf{x}) = \mathbf{x} - ((\mathbf{x} - \mathbf{x}_A) \cdot \mathbf{n}_{\triangle ABC}) \mathbf{n}_{\triangle ABC}, \quad (5.37)$$

with $\mathbf{n}_{\triangle ABC}$ a unit normal of the plane and \mathbf{x}_A the coordinates of point A . For the same point \mathbf{x} , the projection to the line defined by the edge $\overline{AB} \in \mathcal{E}^0$ is given by

$$\mathbf{x}_{\overline{AB}}^p(\mathbf{x}) = \mathbf{x}_A + (\mathbf{d}_{\overline{AB}} \cdot (\mathbf{x} - \mathbf{x}_A)) \mathbf{d}_{\overline{AB}}, \quad (5.38)$$

with $\mathbf{d}_{\overline{AB}}$ the unit direction vector of the line. The trivial projection of \mathbf{x} onto the point A is given by

$$\mathbf{x}_A^p(\mathbf{x}) = \mathbf{x}_A. \quad (5.39)$$

To find the minimal distance between the point $\mathbf{x}_i \in \mathcal{T}_E^{n+1}$ and the triangulated surface $\Gamma(t^{n+1})$, we project \mathbf{x}_i onto all triangles in \mathcal{T}^0 , all edges in \mathcal{E}^0 and all points \mathcal{X}^0 . We then obtain a set of projection points, of which we keep all projections that fall on the defining triangle, edge or point. We then set $|\phi_i^{n+1}|$ to the minimum of all absolute distances and let the sign of ϕ_i^{n+1} be determined by the previous value. This procedure can be described by the following set of equations:

$$\mathcal{T}_p^0 = \{t \in \mathcal{T}^0 \mid \mathbf{x}_t^p(\mathbf{x}_i) \in t\}, \quad \mathcal{E}_p^0 = \{e \in \mathcal{E}^0 \mid \mathbf{x}_e^p(\mathbf{x}_i) \in e\}, \quad (5.40)$$

$$d_\Delta = \min_{t \in \mathcal{T}_p^0} \|\mathbf{x}_i - \mathbf{x}_t^p(\mathbf{x}_i)\|_2, \quad d_j = \min_{e \in \mathcal{E}_p^0} \|\mathbf{x}_i - \mathbf{x}_e^p(\mathbf{x}_i)\|_2, \quad (5.41)$$

$$d_\bullet = \min_{\mathbf{y} \in \mathcal{X}^0} \|\mathbf{x}_i - \mathbf{y}\|_2, \quad \phi_i^{n+1} = \text{sgn}(\tilde{\phi}_i^{n+1}) \min \{d_\Delta, d_j, d_\bullet\}. \quad (5.42)$$

The values d_Δ , d_j and d_\bullet are the optima over, respectively, the triangles, the edges and the points within \mathcal{T}^0 . If \mathcal{T}_p^0 is equal to the empty set \emptyset , we set $d_\Delta = \infty$. Similarly, if $\mathcal{E}_p^0 = \emptyset$, we set $d_j = \infty$.

To reduce the computational effort of this approach, we only apply Equations (5.40) to (5.42) to all mesh points $\mathbf{x}_i \in \mathcal{X}$ up to the 2-th neighbour of \mathcal{X}^0 within \mathcal{T}_E^{n+1} . Further, we only apply the above algorithm on those triangles, edges and points of which the points lie at maximum a distance of $2.5h$ from \mathbf{x}_i , with h the average mesh coarseness. For $2D$ problems, the approach is similarly obtained by projection on all edges and points representing $\Gamma(t^{n+1})$, acceptance of all projections that fall on the defining edges and points and taking again the minimum over all the accepted distances.

The approach given by Equations (5.40) to (5.42) gives an exact value for ϕ^{n+1} if the interface $\Gamma(t^{n+1})$ is exactly described by a polyhedron in $3D$ or a polygon in $2D$. If, however, the surface is not captured exactly by a polyhedron/polygon, we obtain an experimental order of convergence with respect to h close to quadratic over the entire domain Ω . This approach is applicable since no reinitialisation over all of Ω is needed. A benefit is that no termination criterion based on the gradient of ϕ^{n+1} is introduced. A drawback of this approach is the computational effort needed to update ϕ^{n+1} , if one

would incorporate mesh points further away from the interface. This can be avoided by exploiting the fact that an update for a grid point is independent of all other grid points, which allows parallelisation of the approach. The computational cost per updated point is of $\mathcal{O}(1)$ in \mathbb{R}^d due to the restriction of the used triangles, edges and points in the update. Due to our limitation of the reinitialisation on a narrow band around the interface $\mathcal{O}(h^{1-d})$ points are updated, leading to an overall computational cost of $\mathcal{O}(h^{1-d})$, which is of lower order than the computational cost associated with the method in Sussman et al. [1994], which is based on the pseudo-time evolution of a partial differential equation over the entire domain of computation.

5.3.4 Calculation of the interface curvature

To obtain the solubility $c_s(\mathbf{x}, t^{n+1})$, defined by Equation (5.11), we need an approximation κ^{n+1} for the curvature $\kappa(\mathbf{x}, t^{n+1})$ on the boundary $\Gamma(t^{n+1})$, which is defined by Equation (5.15). To obtain this approximation of the curvature we introduce the auxiliary variable $\psi(\mathbf{x}, t)$, defined by

$$\psi(\mathbf{x}, t) = \nabla\phi(\mathbf{x}, t). \quad (5.43)$$

We obtain an approximation ψ^{n+1} of $\psi(\mathbf{x}, t)$ from ϕ^{n+1} on \mathcal{T}_E^{n+1} using the standard Galerkin finite-element technique. We then calculate the approximation \mathbf{n}^{n+1} of the normals $\mathbf{n}(\mathbf{x}, t^{n+1})$ in each mesh point \mathbf{x} of \mathcal{T}_E^{n+1} by the relation

$$\mathbf{n}(\mathbf{x}, t^{n+1}) = \frac{\psi(\mathbf{x}, t^{n+1})}{\|\psi(\mathbf{x}, t^{n+1})\|_2}. \quad (5.44)$$

Subsequently we construct a piecewise linear approximation κ^{n+1} of $\kappa(\mathbf{x}, t^{n+1})$ on \mathcal{T}_E^{n+1} by solving Equation (5.15) using the standard Galerkin finite-element technique, assuming $\mathbf{n}(\mathbf{x}, t^{n+1})$ is piecewise linear on \mathcal{T}_E^{n+1} . The value of $\kappa(\mathbf{x}, t^{n+1})$ on $\Gamma(t^{n+1})$ is subsequently easily derived.

In Chapter 6 we return to the calculation of the interface curvature in more detail.

5.3.5 The algorithm

In the previous sections we discussed three major aspects of our numerical solution technique. In Algorithm 5.1 the approach to solve the problem is given in pseudo-code. One can see at line 10 of Algorithm 5.1 that we have used the Courant-Friedrichs-Lewy condition (CFL) [Courant et al., 1928] to limit the time-step Δt . This limitation arises from the discretisation of Equation (5.16) with the SUPG finite-element and the application of the Explicit-Euler time-integration. In this chapter we used $\text{CFL} = 0.25$. This algorithm is implemented into the commercial software package SEPRAN [Segal, 2010].

Algorithm 5.1 *The algorithm in pseudo-code.*

- 1: Define background mesh \mathcal{T} with coarseness h ;
 - 2: Define initial level-set function ϕ^0 on \mathcal{T} ;
 - 3: Generate enriched mesh \mathcal{T}_E^0 ; See Section 5.3.1.
 - 4: Generate diffusive phase mesh \mathcal{T}_D^0 ; See Section 5.3.1.
 - 5: Define initial concentration \mathbf{c}^0 on \mathcal{T}_D^0 ;
 - 6: Calculate κ^0 . See Section 5.3.4.
 - 7: Calculate \mathbf{c}_s^0 . See Equation (5.11).
 - 8: Calculate \mathbf{v}_n^0 . See Equation (5.8).
 - 9: Set $t = 0$;
 - 10: Set $n = 0$;
 - 11: **while** $t < t_{\text{end}}$ **do**
 - 12: Calculate \mathbf{v}_n^{ex} on \mathcal{T}_E^n ; See Equation (5.17).
 - 13: Set $\Delta t = \text{CFL } h / \max \|\mathbf{v}_n^{\text{ex}}\|_{\infty}$;
 - 14: Calculate ϕ^{n+1} on \mathcal{T}_E^n ; See Equation (5.16).
 - 15: Map ϕ^{n+1} back to \mathcal{T} ;
 - 16: Generate enriched mesh \mathcal{T}_E^{n+1} ; See Section 5.3.1.
 - 17: Reinitialise ϕ^{n+1} on \mathcal{T}_E^{n+1} ; See Section 5.3.3.
 - 18: Generate diffusive phase mesh \mathcal{T}_D^{n+1} ; See Section 5.3.1.
 - 19: Calculate \mathbf{c}_{ex}^n ; See Equation (5.27).
 - 20: Calculate $\mathbf{v}_i^m, i = 1, \dots, C^{n+1}$; See Equation (5.28).
 - 21: Calculate κ^{n+1} . See Section 5.3.4.
 - 22: Calculate \mathbf{c}_s^{n+1} . See Equation (5.11).
 - 23: Set $p = 1$;
 - 24: Set $\mathbf{c}_p^{n+1} = \mathbf{c}_{\text{ex}}^n$;
 - 25: Set $\epsilon = \infty$;
 - 26: **while** $\epsilon \geq \text{FPT}$ **do**
 - 27: Calculate \mathbf{c}_{p+1}^{n+1} ; See Equation (5.34).
 - 28: Calculate ϵ ; See Equation (5.35).
 - 29: Set $p = p + 1$;
 - 30: **end while**
 - 31: Set $\mathbf{c}^{n+1} = \mathbf{c}_p^{n+1}$;
 - 32: Calculate \mathbf{v}_n^{n+1} . See Equation (5.8).
 - 33: Set $n = n + 1$;
 - 34: Set $t = t + \Delta t$;
 - 35: **end while**
-

5.4 Computer Simulations

5.4.1 The experimental accuracy: dissolution of planar and circular precipitates

To investigate the experimental accuracy of our method, we simulate the dissolution of a planar precipitate with initial width 0.615 in the computational domain $[0, 1]^n$ for $n = 2, 3$. Within the precipitate the concentration is given by $c_p = 0.45$, whereas the initial concentration in Ω_D is given by $c_0 = 0.3$ and the equilibrium concentration by $c_s^\infty = 0.33$. We take $\zeta=0$ to exclude curvature effects and assume $D = 1$ and $K = 10^3$, leading to diffusion-controlled dissolution. We take a regular background mesh \mathcal{T} with point spacing $h=1/N$ for several values of N . A simple mass balance gives that under the current settings the equilibrium width of the precipitate is given by 0.51875. We simulate until $t_{\text{end}} = 3$.

We also simulate the dissolution of a circular precipitate with initial radius 0.615 on the unit circle in $2D$. We take the same values for the physical and numerical constants as for the planar dissolution. We discretise the computation domain using linear triangles with coarseness $h = 1/N$ for several values of N . Under the assumption that the precipitate stays circular, a mass balance gives that the equilibrium radius equals 0.47200. We again simulate until $t_{\text{end}} = 3$.

Tables 5.1, 5.2 and 5.3 show the results obtained for the dissolution of the planar and circular precipitates. The mass error is defined as the error in the total mass at $t = t_{\text{end}}$ relative to the initial total mass. The width/radius error is defined as the error in the mean width/radius at $t = t_{\text{end}}$ relative to the equilibrium width/radius. The columns labelled “deviation” represent the standard deviation of the width/radius at $t = t_{\text{end}}$.

The errors in Tables 5.1, 5.2 and 5.3 indicate that Algorithm 5.1 is first-order accurate in h . This is supported by the notion that we have used first-order accurate time-integration techniques and that h and Δt are linearly coupled by the CFL condition. Furthermore, we see from the deviations given in Tables 5.1, 5.2 and 5.3 that for the planar precipitate there is a good convergence in the spread of the points around the mean width, indicating that the shape of the precipitate is correctly preserved. The last column of Table 5.2 gives the deviation of the radius of the circular precipitate. Here we see that we also have conservation of the the circular shape, although we do not obtain the same convergence as for the planar precipitates. We think that this originates from the use of an irregular mesh for the simulation of the circular particle, which decreases the control over the element size in the vicinity of the interface.

5.4.2 Mixed-mode dissolution

To investigate the balance between the reactive and diffusive fluxes, we simulate the dissolution of a square precipitate with initial diagonal 0.42 in the computational domain $[-1/2, 1/2]^2$. The centre of the precipitate is located at the origin $(0, 0)$ and is rotated over 45 degrees. Within the precipitate the concentration is given by $c_p = 0.45$, whereas the initial concentration in Ω_D is given by $c_0 = 0.3$ and the equilibrium concentration by $c_s^\infty = 0.35$. We take $\zeta = 0$ to exclude curvature effects and take $D = 1$. We take an irregular background mesh \mathcal{T} with element size $h = 1/64$.

N	Mass error	Width error	Deviation
16	$2.5187 \cdot 10^{-2}$	$1.5869 \cdot 10^{-1}$	$1.3010 \cdot 10^{-4}$
32	$1.4130 \cdot 10^{-2}$	$8.9000 \cdot 10^{-2}$	$8.1082 \cdot 10^{-5}$
64	$7.6502 \cdot 10^{-3}$	$4.8202 \cdot 10^{-2}$	$5.3468 \cdot 10^{-5}$
128	$4.2333 \cdot 10^{-3}$	$2.6672 \cdot 10^{-2}$	$1.8035 \cdot 10^{-5}$
256	$2.3582 \cdot 10^{-3}$	$1.4856 \cdot 10^{-2}$	$7.8939 \cdot 10^{-6}$
512	$1.2236 \cdot 10^{-3}$	$7.7096 \cdot 10^{-3}$	$3.5917 \cdot 10^{-6}$

Table 5.1: *Experimental accuracy of dissolving a planar precipitate in 2D.*

N	Mass error	Width error	Deviation
16	$2.9987 \cdot 10^{-2}$	$2.2515 \cdot 10^{-1}$	$1.9309 \cdot 10^{-3}$
32	$1.7354 \cdot 10^{-2}$	$1.2327 \cdot 10^{-1}$	$5.4712 \cdot 10^{-4}$
64	$9.4015 \cdot 10^{-3}$	$6.4816 \cdot 10^{-2}$	$1.9345 \cdot 10^{-4}$
128	$5.1214 \cdot 10^{-3}$	$3.4774 \cdot 10^{-2}$	$7.8181 \cdot 10^{-5}$
256	$2.8028 \cdot 10^{-3}$	$1.8861 \cdot 10^{-2}$	$1.3807 \cdot 10^{-5}$

Table 5.2: *Experimental accuracy of dissolving a circular precipitate in 2D.*

N	Mass error	Width error	Deviation
8	$4.3963 \cdot 10^{-2}$	$2.7683 \cdot 10^{-1}$	$1.3539 \cdot 10^{-3}$
16	$2.4420 \cdot 10^{-2}$	$1.5385 \cdot 10^{-1}$	$2.6967 \cdot 10^{-4}$
32	$1.4304 \cdot 10^{-2}$	$9.0121 \cdot 10^{-2}$	$6.2047 \cdot 10^{-5}$
64	$7.6492 \cdot 10^{-3}$	$4.8194 \cdot 10^{-2}$	$3.1252 \cdot 10^{-5}$

Table 5.3: *Experimental accuracy of dissolving a planar precipitate in 3D.*

We simulate until $t_{\text{end}} = 0.25$. For the value of the interface-reaction speed K we take $K = 10^k, k \in \{0, 1, 2, 3\}$.

Figure 5.2 shows the results obtained with Algorithm 5.1 for the various values of K at $t \in \{0, 0.05, 0.1, 0.15, 0.2, 0.25\}$. These results show two effects of the value of K on the dissolution kinetics of the precipitate. First we clearly see that if K decreases in magnitude, the overall dissolution rate of the precipitate slows down, resulting in larger precipitates at $t = 0.25$ for lower values of K . This indicates that for lower values of K the reaction at the interface becomes limiting for the dissolution kinetics, which agrees with what has already been shown in the analysis of the model. Secondly, the shape of the precipitate during dissolution is influenced by the magnitude of K , where a smaller K preserves the initial shape and a larger K causes rounding of the corners of the precipitate. This is a direct consequence of the fact that diffusion is the rate-determining step if K is large. Diffusion processes generally smooth solutions and thereby make the interface smooth. This means that if precipitates observed in physical experiments maintain sharp corners during dissolution, these precipitates could be described best by a mixed-mode model with a low value of K .

5.4.3 Mixed-mode growth

Mullins and Sekerka [1963] have shown that the growth of a precipitate is an unstable process if perturbations of the interface are present. It was further assumed that Equation (5.10) holds instead of Equation (5.7). To investigate these instabilities in our mixed-mode model, we simulate the growth of a square precipitate with initial diagonal 0.1 in the computational domain $[-1/2, 1/2]^2$. The centre of the precipitate is located at the origin $(0, 0)$ and is rotated over 45 degrees. Within the precipitate the concentration is given by $c_p = 0.45$, whereas the initial concentration in Ω_D is given by $c_0 = 0.3$ and the equilibrium concentration by $c_s^\infty = 0.2$. We take $\zeta = 0$ to exclude curvature effects and assume $D = 1$. We take an irregular background mesh \mathcal{T} with coarseness $h = 1/64$. We simulate until $t_{\text{end}} = 0.1$. For the value of the interface-reaction speed K we take $K \in \{10^0, 10^1, 10^2, 10^3\}$.

Figure 5.3 shows the results obtained with Algorithm 5.1 for the various values of K at $t \in \{0, 0.02, 0.04, 0.06, 0.08, 0.1\}$. Similar to the results shown in Figure 5.2 for the dissolution of the square particle, the value of K has two influences on the growth kinetics. First the precipitate grows slower for smaller values of K , as expected from Equation (5.8). Secondly higher values of K cause instabilities to occur in the shape of the interface. As a high value of K corresponds with a diffusion-controlled process, Equation (5.7) could be replaced by Equation (5.10). This indicates that our model reproduces the analytical instabilities shown in Mullins and Sekerka [1963] correctly. We believe that the initial instabilities that are amplified during the simulation are caused by small numerical fluctuations in the concentrations at the interface which are related to the topology of the mesh.

5.4.4 Curvature-influenced growth

In Mullins and Sekerka [1963], it has also been shown that if the curvature of a precipitate is taken into account during growth, the perturbations are damped out. To investigate this effect in the mixed-mode model, we again simulate the precipitate

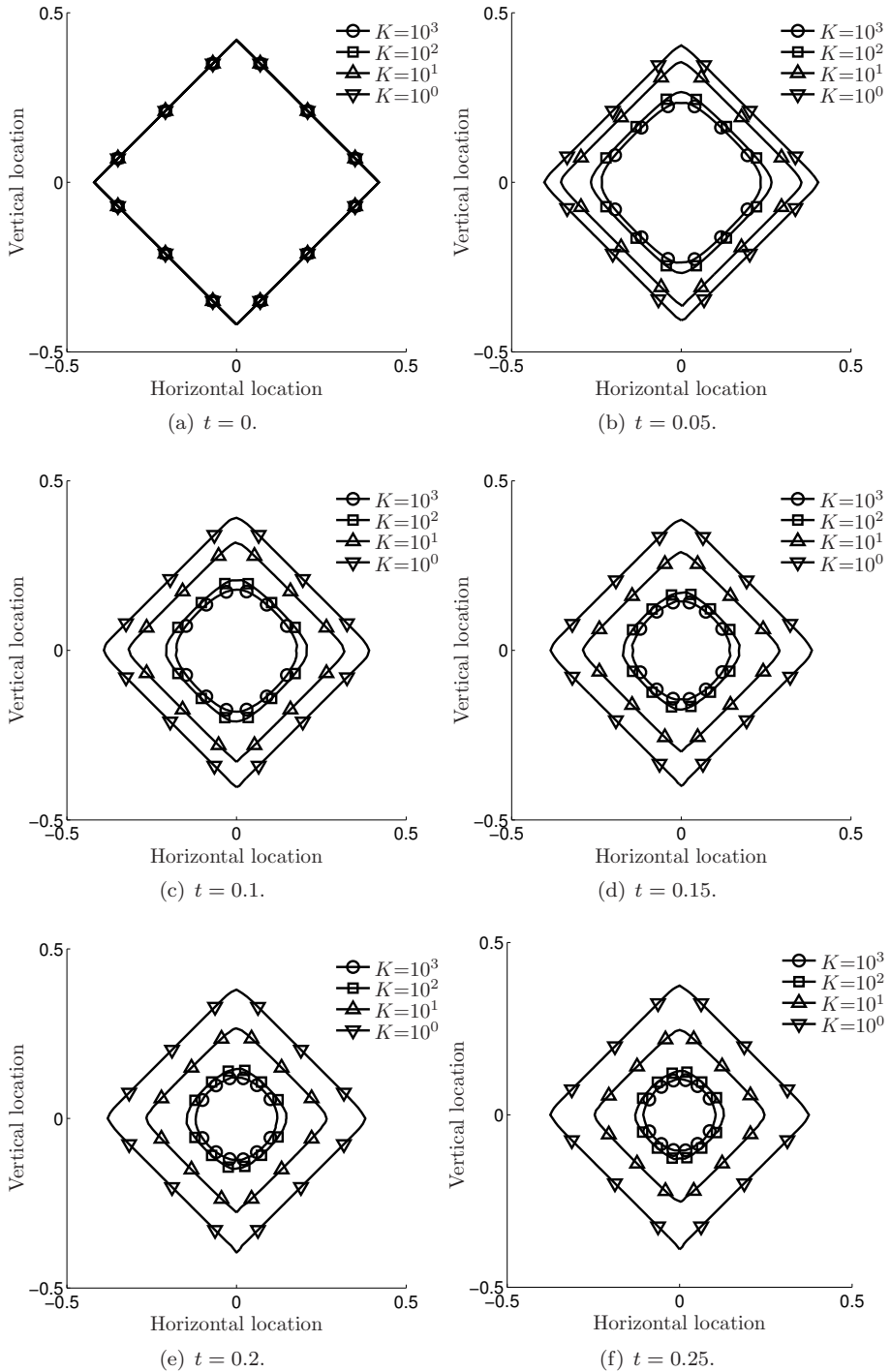


Figure 5.2: 2D mixed-mode dissolution results for the values of $K = \{10^0, 10^1, 10^2, 10^3\}$ at 6 simulation times, where $\zeta = 0$ and $D = 1$.

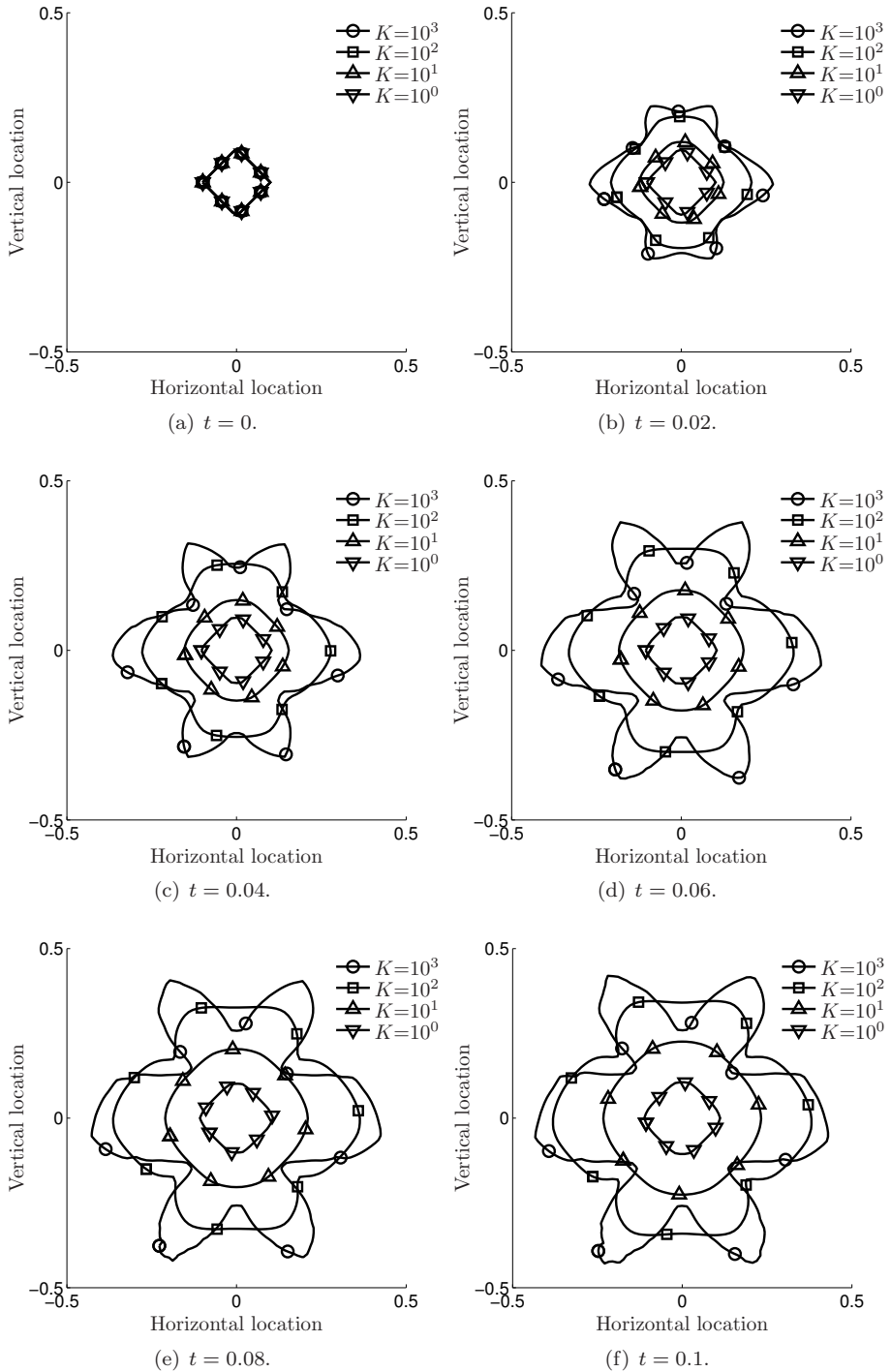


Figure 5.3: 2D mixed-mode growth results for the values of $K \in \{10^0, 10^1, 10^2, 10^3\}$ at 6 simulation times, where $\zeta = 0$ and $D = 1$.

from Section 5.4.3, but now take $K = 1000$ and take $\zeta \in \{0, 10^{-4.5}, 10^{-4}, 10^{-3.5}\}$. All other settings are kept the same.

Figure 5.4 shows the results obtained with Algorithm 5.1 for the various values of ζ at $t \in \{0, 0.02, 0.04, 0.06, 0.08, 0.1\}$. Similar to the influence of K on the dissolution and growth kinetics shown in Figures 5.2 and 5.3, the value of ζ has a significant influence on the growth kinetics. One can see that the amplification of the perturbations reduces significantly for higher values of ζ , thereby suppressing the creation of concave interface parts. If, however, concave interface parts occur, these grow faster for higher values of ζ , thereby reducing the concavity. Furthermore, we see that for larger values of ζ , there is no shape preservation, but rounding of the precipitate. This indicates that a minimal value of ζ could exist such that the shape of the precipitate stays convex. This minimal value may depend on the physical and geometrical application.

5.4.5 Precipitate breakup

During dissolution of precipitates, precipitates might break into several pieces due to the geometry of the initial precipitate. To test the numerical scheme on dealing with these topological changes, we modelled the dissolution of a dumbbell-shaped precipitate, consisting of a sphere with radius 0.15 and centre $(-0.275, 0, 0)$, a sphere with radius 0.2 and centre $(0.21, 0, 0)$ and a connecting cylinder with radius 0.05 with the axis aligned with the x -axis. The computational domain is $[-1/2, 1/2]^3$, the diffusivity $D = \sqrt{2}$, the initial concentration $c_0 = 0$, the precipitate concentration c_p , the solubility $c_s^\infty = 1$, the interface reaction speed $K = 10^3$ and the interfacial parameter $\zeta = 0$. We take a regular mesh with point spacing $1/64$. We simulate until full dissolution is obtained. Figure 5.5 shows the results of these simulations at 6 discrete times.

The dissolution process as shown in Figure 5.5 clearly shows the ability of the level-set method to handle topology changes, as it does not discriminate between one, two or more precipitates, but only considers a sharp interface between two phases. The breakup of the particle is handled without any trouble. Further our algorithm, as presented in Algorithm 5.1, has no problems with the cusps created along the x -axis at the moment of dissolution of the connecting cylinder.

5.4.6 Cementite dissolution in austenite

To investigate the performance of the model further, we simulate the dissolution of a cementite particle within austenite based on the diffusion process of carbon in austenite. The computational austenite domain is taken as 2.5 by 4 by $0.5 \mu\text{m}^3$, which contains a cementite particle of size 1 by 3.5 by $0.1 \mu\text{m}^3$. The cementite particle is perturbed inward near several lines. For each line, the perturbation is $0.035 \mu\text{m}$ along the line and decreases linear to zero over a region of width $0.2 \mu\text{m}$ around the line. The initial shape of the cementite particle is as shown in Figure 5.6(a). The physical parameters needed for the simulation are given in Table 5.4. The parameters c_s^∞ , D and K reflect the dissolution temperature of 800°C . The value of the interface reaction speed K is chosen proportional to the Debye frequency of carbon multiplied by the distance an atom jumps. The Debye frequency for carbon is in turn proportional

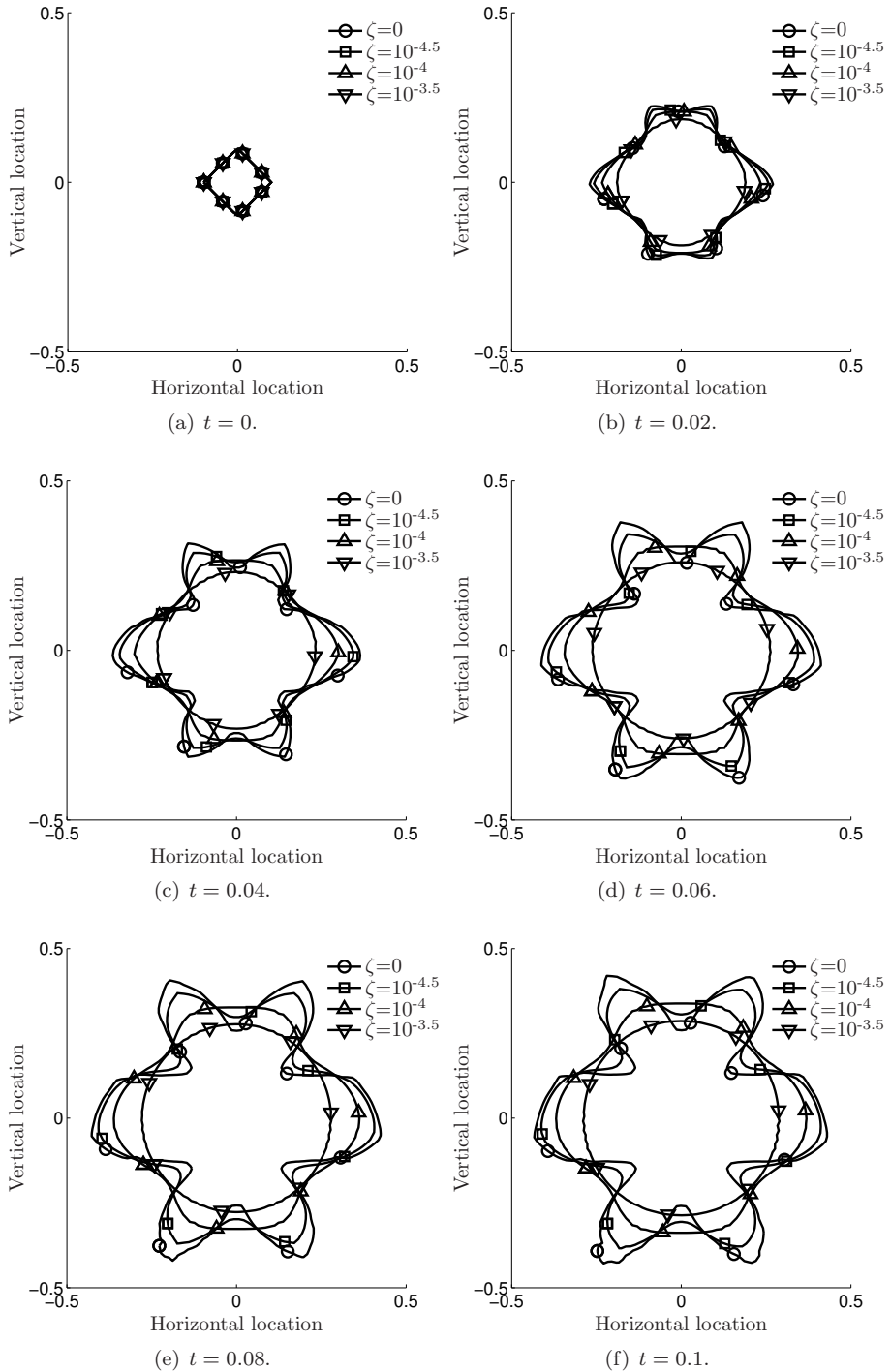


Figure 5.4: 2D mixed-mode growth results for the values of $\zeta \in \{0, 10^{-4.5}, 10^{-4}, 10^{-3.5}\}$ at 6 simulation times, where $K = 10^3$ and $D = 1$.

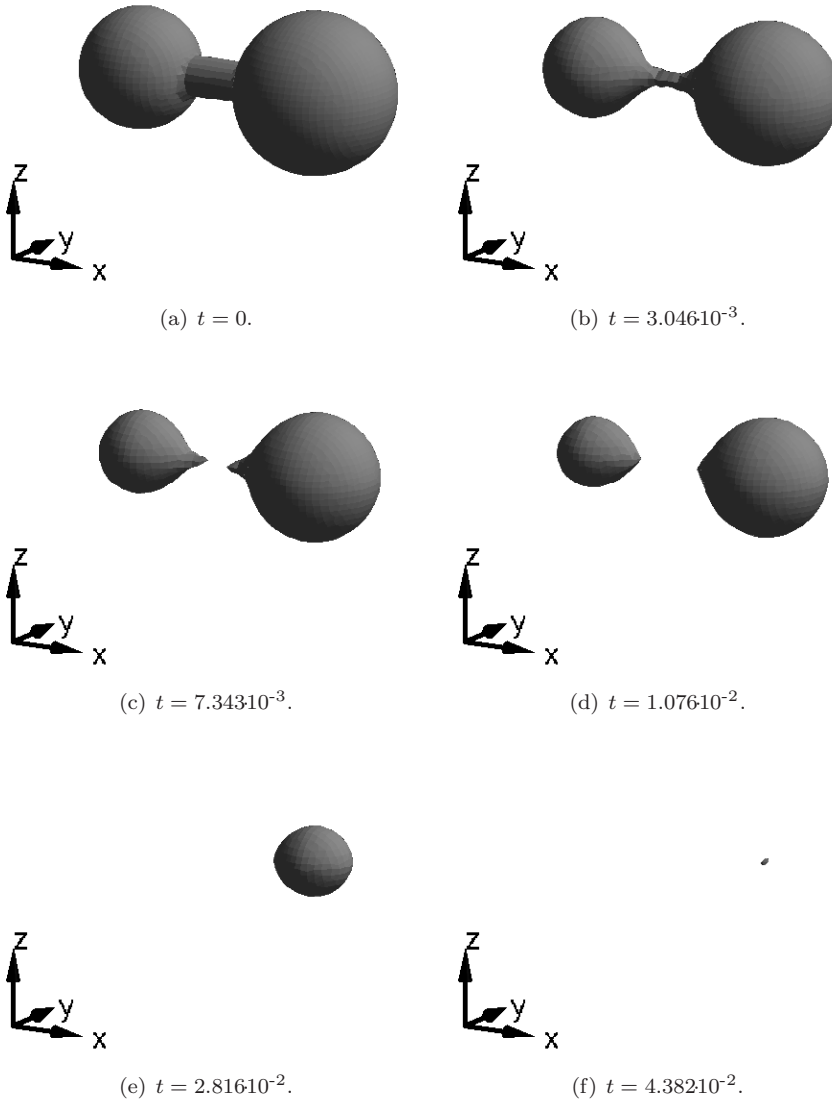


Figure 5.5: *3D dissolution of a dumbbell-shaped precipitate at 6 simulation times, where $K = 10^3$, $\zeta = 0$ and $D = \sqrt{2}$.*

Parameter	Value	Unit	Note
c_p	10718	mol/m ³	Chosen
c_0	0	mol/m ³	Chosen
c_s^∞	4635.5	mol/m ³	Javierre [2006]
ζ	0	μm	Chosen
D	2.98	$\mu\text{m}^2/\text{s}$	Javierre [2006]
a	$3.6462 \cdot 10^{-4}$	μm	
k_0	1		Chosen
K	8172.8	$\mu\text{m}/\text{s}$	Equation (5.45)

Table 5.4: *Physical parameters used for the dissolution of a cementite particle in austenite.*

to the diffusivity D of carbon and inversely proportional to the square of the lattice parameter of austenite. The jump distance is proportional to lattice parameter of austenite. This leads to the equation

$$K = k_0 \frac{D}{a^2} a = k_0 \frac{D}{a}, \quad (5.45)$$

where a is the lattice parameter of austenite at 800°C and k_0 a proportionality constant, set to 1 for the current simulation. We simulate until full dissolution of the cementite particle.

Figure 5.6 shows the cementite particle at six times during dissolution and Figure 5.7 shows the contour of the precipitate along plane in between the top and the bottom of the austenite block. Full dissolution was obtained after $4.2490 \cdot 10^{-3}$ seconds. Both Figures 5.6 and 5.7 show clearly that our model can capture accurately the breakthrough of the cementite particle without adding this behavior explicitly to the model. It furthermore is visible that the symmetry present in the initial precipitate is maintained throughout the entire simulation. A close inspection of Figure 5.6(c) and Figure 5.7 shows that the breakthrough does not only travel from the outside to the inside of the precipitate, but also from the inside of the precipitate to the outside. The initiating points of the latter direction of breakthrough are on the intersection of two perturbation lines.

Within the model the interface reaction speed K remains an unknown physical quantity, which we estimate in the current simulation with Equation (5.45). If we consider the diffusion distance $L_D = \sqrt{Dt_{\text{diss}}}$ with t_{diss} the full dissolution time, we obtain $L_D = 0.1125 \mu\text{m}$, which of the same order of magnitude as the thickness of $0.1 \mu\text{m}$ as the initial precipitate. This indicates that the chosen value and equation for K could be correct. We however do note that the equation for K is a simplistic assumption. Another approach to obtain a value for the interface reaction speed K is to relate it to the interface mobility $M_{\gamma\theta}$ of the interface between austenite and cementite and the difference in Gibbs free energy $\Delta G_{\gamma\theta}$ between austenite and cementite. A common equation, used for example in Leeuwen et al. [2001], for the normal velocity of an interface between the two phases is

$$v_n = M_{\gamma\theta} \Delta G_{\gamma\theta}, \quad (5.46)$$

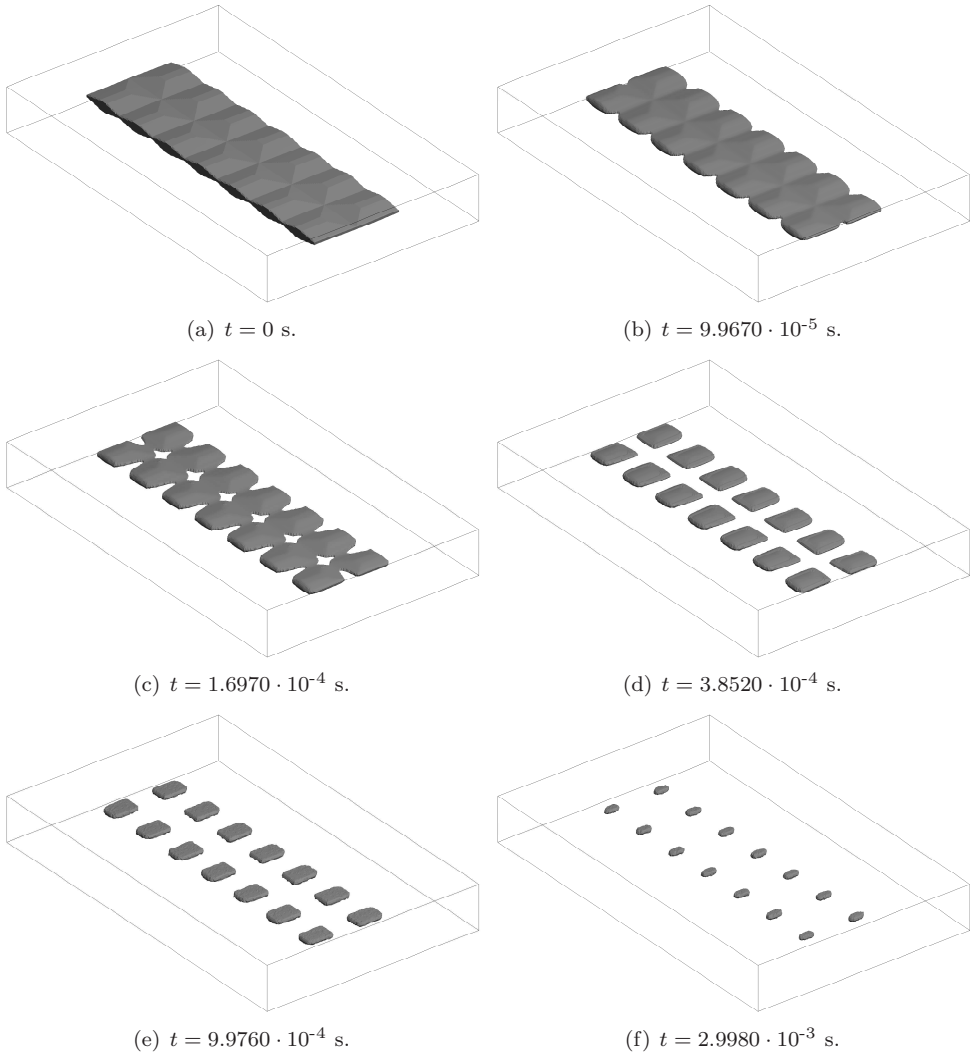


Figure 5.6: *Dissolution of a cementite particle within an austenite matrix at several instances.*

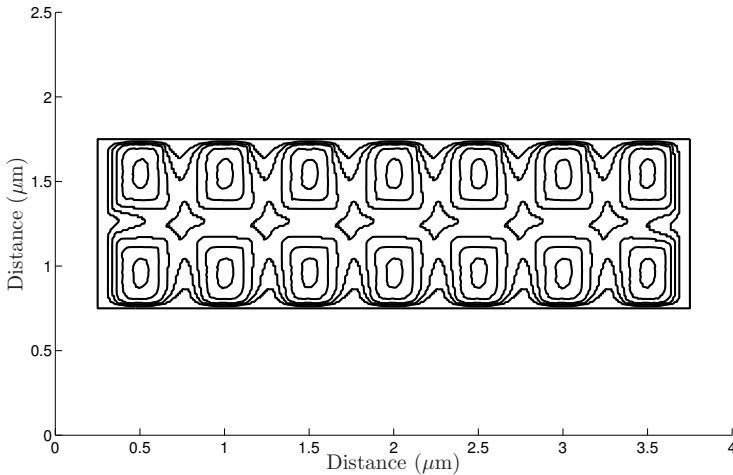


Figure 5.7: *Dissolution of a cementite particle within an austenite matrix at the same times as in Figure 5.6. Contours for consecutive times go from the outside to the inside.*

where $\Delta G_{\gamma\theta}$ is a function of all chemical species in the alloy. One could possibly relate K to this equation by assuming a flat interface, a constant concentration within the matrix, a linear approximation of $\Delta G_{\gamma\theta}$ based on the concentration of carbon within the two phases and the use of Equation (5.6). This however still requires knowledge on the value of $M_{\gamma\theta}$. One could use Darken's Law to relate the diffusion coefficient D , the concentration c and the free energy change $\Delta G_{\gamma\theta}$ to the mobility $M_{\gamma\theta}$, which then again would lead to some equation for K involving the diffusion coefficient D , similar to Equation (5.45). This is however out of the scope this thesis and would recommend it for future research. We will use in the remainder of this thesis Equation (5.45) to obtain a value for the interface reaction speed K .

5.5 Summary and Conclusion

We described a physical model for the mixed-mode dissolution and growth of precipitates within a diffusive phase. The kinetics governing growth and dissolution are influenced by the concentration gradient of a single chemical element near the precipitate interface and an interface reaction. The model also incorporates the local curvature of the interface and the influence of this curvature on the equilibrium between the precipitate and the diffusive phase. The shape and topology of the precipitate are modelled using the level-set method [Osher and Sethian, 1988], where the moving interface is treated as a sharp transition.

Using the current level-set function a background triangulation is transformed to two new meshes, which contains an explicit representation of the interface between the precipitate and the diffusive phase. On these meshes the appearing hyperbolic partial differential equations have been discretised using Streamline-Upwind Petrov-Galerkin finite-element techniques [Tornberg and Engquist, 2000] and a first-order time integration. The required reinitialisation of the level-set function [Sethian, 1999,

Sussman et al., 1994] has been done using an efficient direct approach based on the explicit representation of the interface.

It has been shown that our model and accompanying discretisation achieves first order accuracy with respect to the mesh coarseness for the dissolution of planar and circular precipitates, which agrees with the theory due to the coupling of the mesh coarseness and the time step by the CFL condition [Courant et al., 1928].

The introduced interface reaction speed K has been shown to influence the mixed-mode dissolution of precipitates, where higher values of K cause diffusion-limited dissolution and loss of the shape, e.g. a transition from square to circular, whereas lower values of K cause reaction-limited dissolution and shape preservation.

Our model is able to reproduce the analytical instability which was studied in Mullins and Sekerka [1963], where the onset of the initial instabilities of the interface result from local fluctuations of the numerical error from the finite-element discretisation. These instabilities can be suppressed by two different parameters, the interface reaction speed K and the interfacial parameter ζ . The first parameter causes dampening of the instabilities using the interface reaction and has, similar to mixed-mode dissolution, a shape preserving effect. The parameter ζ introduces indirectly via Equation (5.11) a curvature-driven growth, where concave regions grow faster than convex regions. This curvature driven growth causes rounding of the precipitate.

It has also been shown that the topological changes associated with the dissolution of a dumbbell-shaped precipitate are captured accurately with ease by using the level-set method. The cusps appearing on the interface during the breakup of the precipitate in two smaller precipitate are handled correctly, as is the full dissolution of one of the two remaining precipitates after breakup.

A final simulation of the dissolution of a cementite particle within block of austenite shows that the model and algorithm can handle realistic scenarios and parameters with ease. In this case again breakthrough is observed, which is handled correctly by the algorithm. We further propose a simple equation for the interface reaction speed K , which can be used as a first approximation, and gives reasonable results.

Bibliography

- J.-O. Andersson, T. Helander, L. Höglund, P. Shi and B. Sundman. Thermo-Calc & DICTRA, computational tools for materials science. *Calphad*, 26(2):273–312, 2002.
- S. Chen, B. Merriman, S. Osher and P. Smereka. A Simple Level Set Method for Solving Stefan Problems. *Journal of Computational Physics*, 135(1):8 – 29, 1997.
- R. Courant, K. Friedrichs and H. Lewy. Über die partiellen Differenzgleichungen der mathematischen Physik. *Mathematische Annalen*, 100:32–74, 1928.
- A. Deschamps and Y. Brechet. Influence of predeformation and ageing of an Al-Zn-Mg alloy – II. Modeling of precipitation kinetics and yield stress. *Acta Materialia*, 47(1):293–305, 1999.
- S. Hu and C.H. Henager Jr. Phase-field simulations of Te-precipitate morphology

- and evolution kinetics in Te-rich CdTe crystals. Journal of Crystal Growth, 311 (11):3184–3194, 2009.
- E. Javierre. Numerical methods for vector Stefan models of solid-state alloys. PhD thesis, Delft University of Technology, The Netherlands, 2006.
- R. Kampmann and R. Wagner. Materials Science and Technology - A Comprehensive Treatment, volume 5. VCH, Weinheim, Germany, 1991.
- Y. van Leeuwen, M. Onink, J. Sietsma and S. van der Zwaag. The $\gamma - \alpha$ Transformation Kinetics of Low Carbon Steels under Ultra-fast Cooling Conditions. ISIJ International, 41(9):1037–1046, 2001.
- W.W. Mullins and R.F. Sekerka. Morphological Stability of a Particle Growing by Diffusion or Heat Flow. Journal of Applied Physics, 34(2):323 – 329, 1963.
- S.J. Osher and R.P. Fedkiw. Level Set Methods and Dynamic Implicit Surfaces. Springer, New York, NY, United States of America, 1 edition, 2002.
- S.J. Osher and J.A. Sethian. Fronts propagating with curvature-dependent speed: Algorithms based on Hamilton-Jacobi formulations. Journal of Computational Physics, 79(1):12–49, 1988.
- D. den Ouden, F.J. Vermolen, L. Zhao, C. Vuik and J. Sietsma. Modelling of particle nucleation and growth in binary alloys under elastic deformation: An application to a Cu-0.95 wt%Co alloy. Computational Materials Science, 50(8):2397–2410, 2011.
- M. Perez. Gibbs-Thomson effects in phase transformations. Scripta Materialia, 52 (8):709–712, 2005.
- D.A. Porter and K.E. Easterling. Phase Transformations in Metals and Alloys. Chapman & Hall, London, United Kingdom of Great Britain and Northern Ireland, 2nd edition, 1992.
- J.D. Robson. Modelling the evolution of particle size distribution during nucleation, growth and coarsening. Materials Science and Technology, 20:441–448, 2004.
- G. Segal. SEPRAN manuals. Den Haag, The Netherlands, 2010.
- G. Segal, C. Vuik and F.J. Vermolen. A conserving discretization for the free boundary in a two-dimensional Stefan problem. Journal of Computational Physics, 141(1): 1–21, 1998.
- J. A. Sethian. Fast marching methods. SIAM Rev., 41(2):199–235, 1999.
- F. Soisson, A. Barbu and G. Martin. Monte Carlo simulation of Copper precipitation in dilute Iron-Copper alloys during thermal ageing and under electron radiation. Acta Materialia, 44(9):3789–3800, 1996.
- M. Sussman, P. Smereka and S.J. Osher. A Level Set Approach for Computing Solutions to Incompressible Two-Phase Flow. Journal of Computational Physics, 114(1):146–159, 1994.

- A.-K. Tornberg and B. Engquist. A finite element based level-set method for multi-phase flow applications. Computing and Visualization in Science, 3:93–101, 2000.
- F.J. Vermolen. On Similarity Solutions and Interface Reactions for a Vector-Valued Stefan Problem. Nonlinear Analysis: Modelling and Control, 12:269–288, 2007.
- F.J. Vermolen, E. Javierre, C. Vuik, L. Zhao and S. van der Zwaag. A three-dimensional model for particle dissolution in binary alloys. Computational Materials Science, 39:767–774, 2007.
- C. Vuik. Phase Change Analysis and Jozef Stefan. In J.C. Crepeau, editor, Jozef Stefan: His Scientific Legacy on the 175-th Anniversary of His Birth, pages 166–183, Bussum, The Netherlands, 2013. Bentham Science Publishers.
- C. Zener. Theory of growth of spherical precipitates from solid solution. Journal of Applied Physics, 20(10):950–953, 1949.

Chapter 6

The Level-Set Method for Multi-Component Alloys

6.1 Introduction

In Ouden et al. [2013], a model is proposed for the growth and dissolution of precipitates in binary alloys. Common alloys however do contain several alloying elements, i.e. HSLA steels which contain for example iron, carbon, nitrogen and niobium, and precipitates formed within these alloys also are composed of several elements. In this chapter we will first give a short overview of the moving boundary model used for the description of growth and dissolution in a multi-component alloy, based on the model from Ouden et al. [2013]. Subsequently, we discuss some numerical aspects of our approach and finally we discuss the quality of the results obtained with our method.

6.2 The Stefan Problem

In this section, we describe the models used to simulate the dissolution and growth of a precipitate in a diffusive phase, the matrix, driven by multiple chemical elements. The level-set method, introduced in Osher and Sethian [1988], is used for the description of the boundary, whereas diffusive and reaction fluxes physically determine the movement of the interface.

We assume that within the system a set of $N + 1$ chemical elements are present, of which N elements are present within the precipitate and the matrix. We assume the matrix has a crystal structure consisting of the $(N+1)$ -th element in which the other N elements can diffuse. The model for the elements is similar to the binary model described in Ouden et al. [2013], extended to a multi-component system.

6.2.1 Evolution of the Concentrations

Our model is based on the original Stefan problem described by Jožef Stefan in 1890 (see Vuik [2013]). Consider a matrix $\Omega_D(t)$ in which a precipitate $\Omega_P(t)$ has nucleated at some point. Here $\Omega_D(t)$ and $\Omega_P(t)$ are open domains. Let $\Gamma(t)$ denote the interface

between the two phases, which represents the moving boundary in our model. We use the multi-component version of Fick's second law for the description of the concentrations $c_e(\mathbf{x}, t)$, $e = 1, \dots, N$ within the matrix, where we assume that all species diffuse independently:

$$\frac{\partial c_e}{\partial t}(\mathbf{x}, t) = \nabla \cdot (D_e(\mathbf{x}, t) \nabla c_e(\mathbf{x}, t)), \quad \text{for } \mathbf{x} \in \Omega_D(t), t > 0, e = 1, \dots, N, \quad (6.1)$$

where $D_e, e = 1, \dots, N$ are the diffusivities of the chemical elements. Within the precipitate $\Omega_P(t)$ we assume constant concentrations $c_e^p, e = 1, \dots, N$. On the outer boundary of Ω_D , i.e. $\partial\Omega_D(t) \setminus \Gamma(t)$, we assume a no-flux condition, which results into an homogeneous Neumann boundary condition. We note that all the methods presented in this article can also be applied to vector-valued problems with an-isotropic diffusivities and/or cross-diffusivities, see for example Vermolen [2007].

For each element $e \in \{1, \dots, N\}$, we take the same set of boundary conditions at the precipitate/matrix interface $\Gamma(t)$ as in Ouden et al. [2013]:

$$K_e(\mathbf{x}, t) (c_e^s(\mathbf{x}, t) - c_e(\mathbf{x}, t)) = D_e(\mathbf{x}, t) \frac{\partial c_e}{\partial n}(\mathbf{x}, t) + c_e(\mathbf{x}, t) v_n(\mathbf{x}, t), \quad (6.2)$$

$$c_e^p v_n(\mathbf{x}, t) = D_e \frac{\partial c_e}{\partial n}(\mathbf{x}, t) + c_e(\mathbf{x}, t) v_n(\mathbf{x}, t), \quad (6.3)$$

$$\text{for } \mathbf{x} \in \Gamma(t), t > 0.$$

In these definitions $K_e(\mathbf{x}, t)$ is the interface-reaction speed, $c_e^s(\mathbf{x}, t)$ the local equilibrium concentration and $v_n(\mathbf{x}, t)$ denotes the speed of the interface in the outward normal direction $\mathbf{n}(\mathbf{x}, t)$ from the domain $\Omega_D(t)$ at $\Gamma(t)$.

By subtracting Equation (6.3) from Equation (6.2) we see that the interface velocity $v_n(\mathbf{x}, t)$ is given by

$$v_n(\mathbf{x}, t) = \frac{K_e(\mathbf{x}, t)}{c_e^p} (c_e^s(\mathbf{x}, t) - c_e(\mathbf{x}, t)), \quad \text{for } \mathbf{x} \in \Gamma(t), t > 0, \quad (6.4)$$

for an arbitrary element e . Substituting the above result in either Equation (6.2) or (6.3), yields that the normal diffusive flux at the interface for any element e is given by

$$D_e(\mathbf{x}, t) \frac{\partial c_e}{\partial n}(\mathbf{x}, t) = \frac{K_e(\mathbf{x}, t)}{c_e^p} (c_e^s(\mathbf{x}, t) - c_e(\mathbf{x}, t)) (c_e^p - c_e(\mathbf{x}, t)), \quad (6.5)$$

$$\text{for } \mathbf{x} \in \Gamma(t), t > 0.$$

In this paper we assume that the solubility of all elements at the precipitate/matrix interface inside the matrix, $c_e^s(\mathbf{x}, t), e = 1, \dots, N$, is modelled using the Gibbs-Thomson effect [Perez, 2005, Porter and Easterling, 1992]

$$\prod_{e=1}^N (x_e^s(\mathbf{x}, t))^{x_e^p} = K^\infty(t) \exp(\zeta(\mathbf{x}, t) \kappa(\mathbf{x}, t)) =: K_\kappa^\infty(\mathbf{x}, t), \quad (6.6)$$

where $x_e^s(\mathbf{x}, t)$ and x_e^p are, respectively, the solubility mole fractions and the mole fractions within the precipitate. The function $\zeta(\mathbf{x}, t)$ is a positive physical factor and

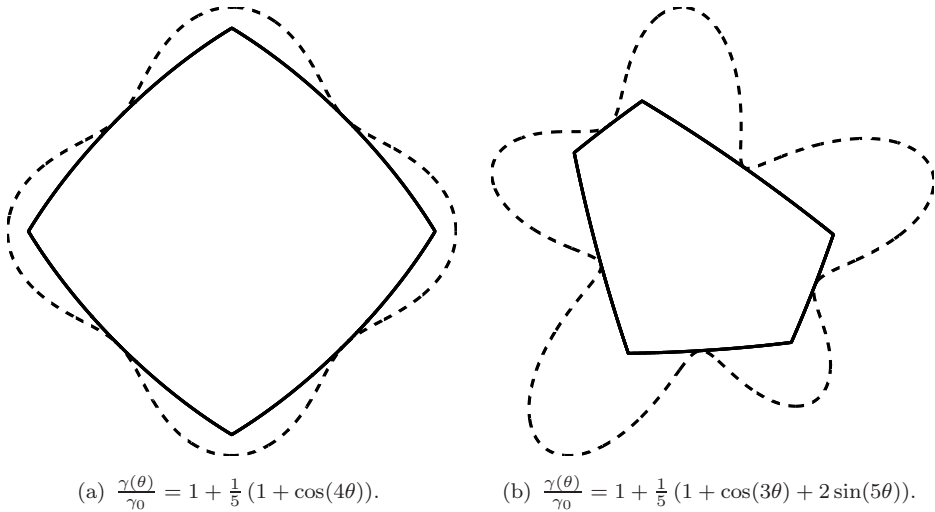


Figure 6.1: *Two examples of Wulff diagrams. θ is the angle between \mathbf{n}_p and the horizontal axis. The solid line indicates the equilibrium shape, the dashed line the (normalized) polar plot of the interfacial energy.*

$\kappa(\mathbf{x}, t)$ the sum of the local principle curvatures of the interface $\Gamma(t)$, to which we refer to as sum-curvature in the remainder of this chapter. The solubility product $K^\infty(t)$ can be derived from thermodynamic databases such as ThermoCalc [Andersson et al., 2002]. The function $\zeta(\mathbf{x}, t)$ is defined as

$$\zeta(\mathbf{x}, t) := \frac{\gamma(\mathbf{x}, t)V_m}{R_g T}, \quad (6.7)$$

with $\gamma(\mathbf{x}, t)$ the interface energy, V_m the molar volume of the precipitate, R_g the gas constant and T the temperature. We allow the interface energy to be anisotropic, but we restrict it to be a function of the direction of the normal $\mathbf{n}_p(\mathbf{x}, t)$ of the interface outward of the particle, i.e. $\gamma(\mathbf{x}, t) = \gamma(-\mathbf{n}(\mathbf{x}, t))$, with $\mathbf{n}(\mathbf{x}, t)$ the outward normal of $\Omega_D(t)$. For a given interface energy function $\gamma(\mathbf{n}_p)$, a Wulff diagram can be constructed which predicts the equilibrium shape of the particle. This diagram is constructed by performing the following steps [Herring, 1951, Straumal et al., 2004]:

- 6.1. For every normal direction \mathbf{n}_p draw a point at $\gamma(\mathbf{n}_p)\mathbf{n}_p$;
- 6.2. For every point of this plot draw a line/plane through this point and perpendicular to $\gamma(\mathbf{n}_p)\mathbf{n}_p$;
- 6.3. Draw the envelope of the area/volume that can be reached from the origin without crossing any of the lines/planes.

The equilibrium shape of the crystal is given by the inner envelope drawn in step 3 above. Figure 6.1 shows two examples of such Wulff diagrams.

For a sphere the derivation of Equation (6.6) can be found in Perez [2005], leading to $\kappa = 2/R$ where R is the radius of the sphere. By Equation (6.6) the product of

equilibrium concentrations increases for locally convex interfaces, which have positive sum-curvature, and decreases for locally concave interfaces, which have negative sum-curvature. This amplification/dampening will cause the precipitate to grow/dissolve to the configuration with the lowest overall surface tension, i.e. the total energy of the system will be minimised.

Assuming a specific lattice structure for the matrix, such as face-centred cubic (fcc), and an absence of vacancies, we can divide the set of elements $\mathbb{E} = \{1, \dots, N\}$ into subsets \mathbb{S} and \mathbb{I} , where the subset \mathbb{S} contains the substitutional elements and the subset \mathbb{I} contains the interstitial elements. Using the crystal structure of the matrix, we can define a maximum total concentration of substitutional elements M , given by

$$M := \frac{m}{vN_A}, \quad (6.8)$$

where m is the number of substitutional sites in a lattice unit cell, v is the volume of a lattice unit cell and N_A is the Avogadro constant. We can now define the mole fractions used in Equation (6.6) as

$$x_e^s(\mathbf{x}, t) := \frac{c_e^s(\mathbf{x}, t)}{\sum_{f \in \mathbb{I}} c_f^s(\mathbf{x}, t) + M}, \quad \text{and} \quad x_e^p := \frac{c_e^p}{\sum_{f=1}^{N+1} c_f^p}. \quad (6.9)$$

The local equilibrium concentrations $c_e^s(\mathbf{x}, t)$ for $e = 1, \dots, N$ are not uniquely determined by Equation (6.6). Similar to Javierre [2006], Equation (6.4) implicitly implies

$$\frac{K_e^s(\mathbf{x}, t)}{c_e^p} (c_e^s(\mathbf{x}, t) - c_e(\mathbf{x}, t)) = \frac{K_{e-1}(\mathbf{x}, t)}{c_{e-1}^p} (c_{e-1}^s(\mathbf{x}, t) - c_{e-1}(\mathbf{x}, t)), \quad (6.10)$$

for $\mathbf{x} \in \Gamma(t)$, $t > 0$,

for all elements $e = 2, \dots, N$. Equation (6.6), combined with the above equations, gives rise to a set of N equations from which the local equilibrium concentrations $c_e^s(\mathbf{x}, t)$ can be solved, assuming the concentrations $c_e(\mathbf{x}, t)$ are known. As no analytical solution is known for this problem, we will solve this problem with an iterative method, which will be discussed in Section 6.3.3.

6.2.2 The Level-Set Method

We will employ, similar to Ouden et al. [2013], the level-set method [Osher and Sethian, 1988] to describe the interface $\Gamma(t)$ and its motion. We define the used signed-distance function by

$$\phi(\mathbf{x}, t) := \begin{cases} + \min_{\mathbf{y} \in \Gamma(t)} \|\mathbf{y} - \mathbf{x}\|_2 & \text{if } \mathbf{x} \in \overline{\Omega}_P(t) \setminus \Gamma(t), \\ 0 & \text{if } \mathbf{x} \in \Gamma(t), \\ - \min_{\mathbf{y} \in \Gamma(t)} \|\mathbf{y} - \mathbf{x}\|_2 & \text{if } \mathbf{x} \in \overline{\Omega}_D(t) \setminus \Gamma(t). \end{cases} \quad (6.11)$$

with the normal $\mathbf{n}(\mathbf{x}, t)$

$$\mathbf{n}(\mathbf{x}, t) := \frac{\nabla \phi(\mathbf{x}, t)}{\|\nabla \phi(\mathbf{x}, t)\|_2}, \quad (6.12)$$

which will point into $\Omega_P(t)$ and out of $\Omega_D(t)$ due to our chosen orientation of $\phi(\mathbf{x}, t)$. The sum-curvature used in Equation (6.6) is defined as

$$\kappa(\mathbf{x}, t) := -\nabla \cdot \frac{\nabla \phi(\mathbf{x}, t)}{\|\nabla \phi(\mathbf{x}, t)\|_2}. \quad (6.13)$$

The movement of the interface is captured by evolving the signed-distance function $\phi(\mathbf{x}, t)$ using the convection equation [Osher and Fedkiw, 2002]

$$\frac{\partial \phi}{\partial t}(\mathbf{x}, t) + v_n^{\text{ex}}(\mathbf{x}, t) \|\nabla \phi(\mathbf{x}, t)\|_2 = 0, \quad \text{for } \mathbf{x} \in \Omega, t > 0, \quad (6.14)$$

where the extended normal velocity $v_n^{\text{ex}}(\mathbf{x}, t)$ is calculated from $v_n(\mathbf{x}, t)$, as defined in Equation (6.4), using the technique described in Ouden et al. [2013].

The reinitialisation of the signed-distance function will be performed with the method proposed in Ouden et al. [2013], ensuring that $\phi(\mathbf{x}, t)$ remains a signed-distance function during the application of the model.

6.2.3 The initial condition

For testing purposes, it is essential to have an initial condition for Equation (6.1) for which the boundary condition in Equation (6.5) on $\Gamma(0)$ and the no-flux condition on $\partial\Omega_D(0) \setminus \Gamma(0)$ holds. To construct such an initial condition, we first solve the systems

$$\begin{cases} \nabla \cdot (D_e^0 \nabla \tilde{c}_e(\mathbf{x})) = 0 & \text{for } \mathbf{x} \in \Omega_D(0), \\ \tilde{c}_e(\mathbf{x}) = c_e^0 & \text{for } \mathbf{x} \in \partial\Omega_D(0) \setminus \Gamma(0), \\ D_e^0 \frac{\partial \tilde{c}_e}{\partial n}(\mathbf{x}) = \frac{K_e^0}{c_e^p} (c_e^{s,0} - \tilde{c}_e(\mathbf{x})) (c_e^p - \tilde{c}_e(\mathbf{x})) & \text{for } \mathbf{x} \in \Gamma(0), \end{cases} \quad (6.15)$$

for the auxiliary concentrations $\tilde{c}_e, e = 1, \dots, N$ and where $D_e^0 := D_e(\mathbf{x}, 0)$, $K_e^0 := K_e(\mathbf{x}, 0)$ and $c_e^{s,0} := c_e^s(\mathbf{x}, 0)$. For the local equilibrium concentrations $c_e^{s,0}$ we demand that Equation (6.6) holds.

We set our initial condition for $c_e(\mathbf{x}, t), e = 1, \dots, N$ subsequently as

$$c_e(\mathbf{x}, 0) = (\tilde{c}_e(\mathbf{x}) - c_e^0) H(\mathbf{x}) + c_e^0, \quad (6.16)$$

for $e = 1, \dots, N$ and the function $H(\mathbf{x})$ and the parameter σ are defined by

$$H(\mathbf{x}) := \begin{cases} \frac{1}{2} \left(1 - \sin \left(\frac{(\phi(\mathbf{x}, 0) - \sigma)\pi}{2\sigma} \right) \right) & \text{if } |\phi(\mathbf{x}, 0) - \sigma| \leq \sigma, \\ 0 & \text{if } \phi(\mathbf{x}, 0) < -2\sigma, \end{cases} \quad (6.17)$$

$$\sigma := \frac{1}{2} \left| \max_{\mathbf{x} \in \partial\Omega_D(0) \setminus \Gamma(0)} \phi(\mathbf{x}, 0) \right|. \quad (6.18)$$

The parameter σ represents half of the minimum distance between $\Gamma(0)$ and the outer boundary of $\Omega_D(0)$. Our choice for H and σ guarantees a smooth initial condition, which respects both the boundary condition in Equation (6.5) on $\Gamma(0)$ and the no-flux condition on $\partial\Omega_D(0) \setminus \Gamma(0)$.

If an initial condition is available for the concentrations, for example originating from physical measurements, one should verify that this data respects both boundary

conditions. If the boundary conditions do not hold, one could try to solve for the normal velocity $v_n(\mathbf{x}, 0)$ and the equilibrium concentrations such that the concentrations are solutions to, for example, Equation (6.15) and are of minimal distance to the input data, leading to a pde constrained minimisation problem. This approach is however out of scope for this chapter and will not be further investigated.

6.3 Numerical Methodology

Both Equation (6.1) and Equation (6.14) are solved using standard Galerkin finite-element techniques. We combine this discretisation scheme with Explicit-Euler time-integration for the signed-distance function $\phi(\mathbf{x}, t)$ and Implicit-Euler time-integration for the concentrations $c_e(\mathbf{x}, t)$, $e = 1, \dots, N$. All finite-element techniques are applied on meshes with linear elements, for which we use the same meshing techniques as in Ouden et al. [2013]. In the following we will discuss shortly the discretisation of Equation (6.1), the method for sum-curvature recovery and in more detail the approach taken to solve the system consisting of Equations (6.6) and (6.10). We restrict the size of the time-step using a CFL condition [Courant et al., 1928], with the CFL parameter ν set to 0.25.

6.3.1 Solution of Equation (6.1)

We discretise Equation (6.1) combined with boundary conditions in Equation (6.3) using standard Galerkin finite-element techniques and Implicit-Euler time-integration, under the assumption that the normal velocity $v_n(\mathbf{x}, t)$ is known. The finite-element technique will transform Equation (6.1) to a system of ordinary differential equations

$$M(t) \frac{d\mathbf{c}_e(t)}{dt} = S_e(t, \mathbf{v}_n(t)) \mathbf{c}_e(t) + \mathbf{f}_e(t, \mathbf{v}_n(t)), \quad (6.19)$$

for each $e = 1, \dots, N$ and where $\mathbf{c}_e(t)$ represents the finite-element approximation at time t and $\mathbf{v}_n(t)$ is the vector $(v_n(\mathbf{x}_1, t), \dots, v_n(\mathbf{x}_B, t))^T$, where the interface $\Gamma(t)$ consists of B points. The mass matrix $M(t)$, the stiffness matrix $S_e(t, \mathbf{v}_n(t))$ and vector $\mathbf{f}_e(t, \mathbf{v}_n(t))$ contain integrals over the domain $\Omega_D(t)$ and the interface $\Gamma(t)$.

Application of Implicit-Euler time-integration on Equation (6.19) leads to the matrix-vector equation

$$(M(t^{\tau+1}) - \Delta t S_e(t^{\tau+1}, \mathbf{v}_n^{\tau+1})) \mathbf{c}_e^{\tau+1} = M(t^{\tau+1}) \mathbf{c}_e^{\tau} + \Delta t \mathbf{f}_e(t^{\tau+1}, \mathbf{v}_n^{\tau+1}), \quad (6.20)$$

where the superscript τ refers to the evaluation of the variable at the discrete time t^τ and Δt is the chosen time step. As in Ouden et al. [2013] there might be a dimensional mismatch between $M(t^{\tau+1})$ and \mathbf{c}_e^τ .

The dimensional mismatch in Equation (6.20) is overcome by application of a similar technique as in Ouden et al. [2013] by introduction of a mesh velocity \mathbf{v}^{mesh} and the extension of \mathbf{c}_e^τ to the mesh at $t^{\tau+1}$. This approach leads to N linear systems in $\mathbf{c}_e^{\tau+1}$, $e = 1, \dots, N$ which can easily be solved, assuming the normal velocity $\mathbf{v}_n^{\tau+1}$ is known.

To calculate the mesh velocity, we start by projecting all points on the (discrete) boundary $\mathcal{E}^{\tau+1}$ to the (discrete) boundary \mathcal{E}^τ , which both are known from the mesh

generation step [See Ouden et al., 2013]. Thereafter we apply an extension procedure to the displacements of all points in $\mathcal{T}_D^{\tau+1}$, by solving in each direction the Laplace equation with Dirichlet conditions on $\Gamma(t^{\tau+1})$ and homogeneous Dirichlet conditions on the outer boundary of $\Omega_D(t^{\tau+1})$. This gives a new set of coordinates $\{\tilde{\mathbf{x}}_i\}_i$, which we use to define the mesh velocity by

$$\mathbf{v}^{\text{mesh}}(\mathbf{x}_i) := \frac{\mathbf{x}_i - \tilde{\mathbf{x}}_i}{\Delta t}, \quad (6.21)$$

and the extended concentration fields by interpolation

$$\mathbf{c}_e^{\tau, \text{ex}}(\mathbf{x}_i) := \mathbf{c}_e^\tau(\tilde{\mathbf{x}}_i), \quad (6.22)$$

all for each nodal point i and each chemical element e . This approach results in mesh velocities that have a similar speed near $\mathcal{E}^{\tau+1}$ as the normal speed of the boundary and are also approximately normal to the boundary at any time.

6.3.2 Gradient and sum-curvature recovery

During the solution of Equation (6.14), we must make use of an appropriate approximation of the gradient of $\phi_h(\mathbf{x}, t^\tau)$, to obtain the velocity field needed to advect $\phi_h(\mathbf{x}, t^\tau)$ to $\phi_h(\mathbf{x}, t^{\tau+1})$. To this end we will use the superconvergent gradient method proposed in Zhang and Naga [2005], which exhibits $\mathcal{O}(h^2)$ convergence on regular meshes. For the sake of being general, we consider a d -dimensional space. Within this method for a mesh point \mathbf{x}^p a patch of surrounding mesh points is created of minimum size $\frac{1}{2}d^2 + \frac{3}{2}d + 1$ for linear elements, which are subsequently used to create a quadratic fit $\phi_{h^2}(\mathbf{x}, t^\tau)$ to $\phi_h(\mathbf{x}, t^\tau)$ using least squares. The quadratic fit is of the general d -dimensional form

$$\phi_{h^2}(\mathbf{x}, t^\tau) := A + B^T \eta + \eta^T C \eta, \quad (6.23)$$

with A a scalar, B a $d \times 1$ vector and C a $d \times d$ symmetric matrix and η the scaled centralised coordinate

$$\eta := \frac{\mathbf{x} - \mathbf{x}^p}{h_p}, \quad (6.24)$$

using h_p as the length of the longest edge attached to \mathbf{x}_p . In the point \mathbf{x}_p the gradient is then given as

$$\nabla \phi_{h^2}(\mathbf{x}^p, t^\tau) = h_p^{-1} B, \quad (6.25)$$

and we set our numerical normals as

$$\mathbf{n}_h(\mathbf{x}^p, t^\tau) := \frac{\nabla \phi_{h^2}(\mathbf{x}^p, t)}{\|\nabla \phi_{h^2}(\mathbf{x}^p, t)\|_2} = \frac{B}{\|B\|_2}, \quad (6.26)$$

In determining the normal interface velocity, we need information on the sum-curvature $\kappa(\mathbf{x}, t^{\tau+1})$, which should be determined, using $\phi_h(\mathbf{x}, t^{\tau+1})$, from Equation (6.13). To the authors' knowledge only one convergent method for the reconstruction of the mean-curvature on arbitrary linear triangular meshes is known [Heine, 2013]. This method solves a variational problem for the mean-curvature, which includes a regularisation term. This method has been shown to have a theoretical and numerical

order of $h^{2/3}$, but due to the explicitly introduced regularisation, we choose not to use this method. Within the literature several methods for the reconstruction of the Hessian and/or second derivatives can be found [Picasso et al., 2011, Vallet et al., 2007], but none of these methods have considered recovering the mean-curvature or sum-curvature. In Vallet et al. [2007] it however has been shown that a quadratic patch-based recovery method is the most robust method to recover Hessians.

As the sum-curvature $\kappa(\mathbf{x}, t)$ contains next to first-order derivatives also second-order derivatives, we expect to obtain some manner of convergence if we use a quadratic patch-based recovery method. We propose to calculate the sum-curvature in the mesh point \mathbf{x}^p , by scaling $\nabla\phi_{h^2}(\mathbf{x}, t)$, given by Equation (6.25), by it's Euclidean norm and taking the divergence, which leads to the explicit formula

$$\kappa_h(\mathbf{x}^p, t^\tau) = \frac{2B^T(C - \text{tr}(C)I_d)B}{h_p \|B\|_2^3}, \quad (6.27)$$

for the sum-curvature at the mesh point \mathbf{x}^p around which the patch has been constructed. We will use for each mesh point \mathbf{x}^p a patch consisting of all second neighbours, as tests have shown the best results for this patch size.

We can apply Equation (6.27) in two ways to obtain the sum-curvature in the points of the discrete boundary $\mathcal{E}^{\tau+1}$. The first is to calculate the sum-curvature directly on the points of the mesh $\mathcal{T}_C^{\tau+1}$, which contains points where the level set function is positive and negative and has the boundary $\mathcal{E}^{\tau+1}$ embedded, in the following we will refer to this method as the Fitted Mesh Direct Recovery (FMDR) method. The second approach is to calculate the sum-curvature on the original mesh \mathcal{T} and using linear interpolation to obtain the sum-curvature on the boundary $\mathcal{E}^{\tau+1}$, this method will be referred to as the Unfitted Mesh Direct Recovery (UMDR) method. In Section 6.4.1 we will compare these two approaches.

A second approach for obtaining the sum-curvature at a mesh-point \mathbf{x}^p is by reapplying the quadratic patch-recovery method to all components of the normals calculated with Equation (6.26) and adding the relevant derivatives to obtain the sum-curvature. This approach can also be applied in the two manners discussed previously and will also be part of the comparison on Section 6.4.1. We will refer to these methods as the Fitted Mesh Indirect Recovery (FMIR) method and the Unfitted Mesh Indirect Recovery (UMIR) method.

6.3.3 Obtaining the normal velocity

Equations (6.6) and (6.10) combined with Equations (6.1) and (6.3) constitute a set of $2N + 1$ unknowns on the boundary $\Gamma(t)$ at moment in time. After discretisation in place and time-integration, we obtain a set of $2N + 1$ unknowns in an equally sized set of non-linear equations per mesh point \mathbf{x}^p of the (discrete) boundary $\mathcal{E}^{\tau+1}$. In order to reduce the highly non-linear nature of these equations and to reduce the computational cost, we will discuss the approach taken.

Inspection of Equations (6.1) and (6.3) shows that a linear system is obtained in $c_e^{\tau+1}$, see also Section 6.3.1, if the vector $\mathbf{v}_n^{\tau+1}$ is assumed known. Similarly, one can use Equation (6.4) to obtain

$$c_e^s(\mathbf{x}_p, t^{\tau+1}) = \frac{c_e^p}{K_e(\mathbf{x}^p, t^{\tau+1})} v_n(\mathbf{x}_p, t^{\tau+1}) + c_e(\mathbf{x}_p, t^{\tau+1}), \quad (6.28)$$

for $e = 1, \dots, N$ in every mesh point \mathbf{x}^p of the boundary $\mathcal{E}^{\tau+1}$. This indicates that by obtaining the vectors $\mathbf{c}_e^{\tau+1}$, $\mathbf{c}_e^{s,\tau+1} = (c_e^s(\mathbf{x}_1, t^{\tau+1}), \dots, c_e^s(\mathbf{x}_B, t^{\tau+1}))^T$ and $\mathbf{v}_n^{\tau+1}$, it can be reduced to obtaining the latter vector, the normal velocity.

Using Equations (6.28), (6.9) and Section 6.3.1, we see that $\mathbf{v}_n^{\tau+1}$ must be a solution to Equation (6.6). To this end we will use the Newton-Raphson method in finding the root of the equivalent function

$$f(\mathbf{x}^p) := \frac{\sum_{e=1}^N x_e^p \log(x_e^s(\mathbf{x}^p, t^{\tau+1})) - \log(K_\kappa^\infty(\mathbf{x}^p, t^{\tau+1}))}{\log(K_\kappa^\infty(\mathbf{x}^p, t^{\tau+1}))}, \quad (6.29)$$

for each mesh point \mathbf{x}^p from the boundary $\mathcal{E}^{\tau+1}$. In solving Equation (6.29) we note that we take a first-discretise-then-solve approach, as this procedure drastically reduces the complexity of the root-finding problem. The Jacobians needed for each update of $\mathbf{v}_n^{\tau+1}$ are easily obtained by differentiation of the finite-element equations for $\mathbf{c}_e^{\tau+1}$, $e = 1, \dots, N$ and Equations (6.28), (6.9) and (6.29) with respect to $\mathbf{v}_n^{\tau+1}$.

We note that the initial condition discussed in Section 6.2.3 is obtained using a similar technique as discussed above.

6.4 Numerical tests

6.4.1 Sum-curvature recovery

To obtain an indication of the experimental order of convergence for the four discussed methods for sum-curvature recovery, in conjunction with our meshing algorithm, we have performed several tests. The first test is the calculation of the sum-curvature of a circle with radius $1/2$ centred within $[-1, 1]^2$. The level set function used is given by

$$\phi(\mathbf{x}) = \frac{1}{2} - \|\mathbf{x}\|_2, \quad (6.30)$$

which has the exact sum-curvature of 2 at the circle. The second test is based on the star-shaped parametric curve

$$\begin{cases} x_1(\theta) &= \left(\frac{3}{5} + \frac{1}{10} \cos(6\theta)\right) \cos(\theta), \\ x_2(\theta) &= \left(\frac{3}{5} + \frac{1}{10} \cos(6\theta)\right) \sin(\theta), \end{cases} \quad (6.31)$$

for $\theta \in [0, 2\pi)$. This curve is the zero contour of the function [Ünsulan and Erçil, 2001]

$$\mathcal{I}(\mathbf{x}) = \left(\frac{3}{5} + \frac{1}{10} \cos\left(6 \tan^{-1}\left(\frac{x_2}{x_1}\right)\right)\right)^2 - \|\mathbf{x}\|_2^2. \quad (6.32)$$

We initialise the level set function using the sign of $\mathcal{I}(\mathbf{x})$ and the distance to the curve. The exact sum-curvature at the interface is calculated using Equation (6.31).

For both level set functions, we calculated the sum-curvature on a regular mesh with aligned diagonals and on a mesh with near-equilateral triangles, both with repeated local refinement near the zero-contour of the level set function using the techniques described in Möller [2008], where refinement occurs in bands of two times the average edge length of the mesh after the previous refinement. We present the results

of the four discussed methods in Figures 6.2 and 6.3 in both the discrete 1-norm, 2-norm and ∞ -norm versus the minimum edge length h :

$$\|\mathbf{x}\|_1 := \frac{1}{N} \sum_{i=1}^N |x_i|, \quad (6.33)$$

$$\|\mathbf{x}\|_2 := \sqrt{\frac{1}{N} \sum_{i=1}^N x_i^2}, \quad (6.34)$$

$$\|\mathbf{x}\|_\infty := \max_{i \in \{1, \dots, N\}} |x_i|. \quad (6.35)$$

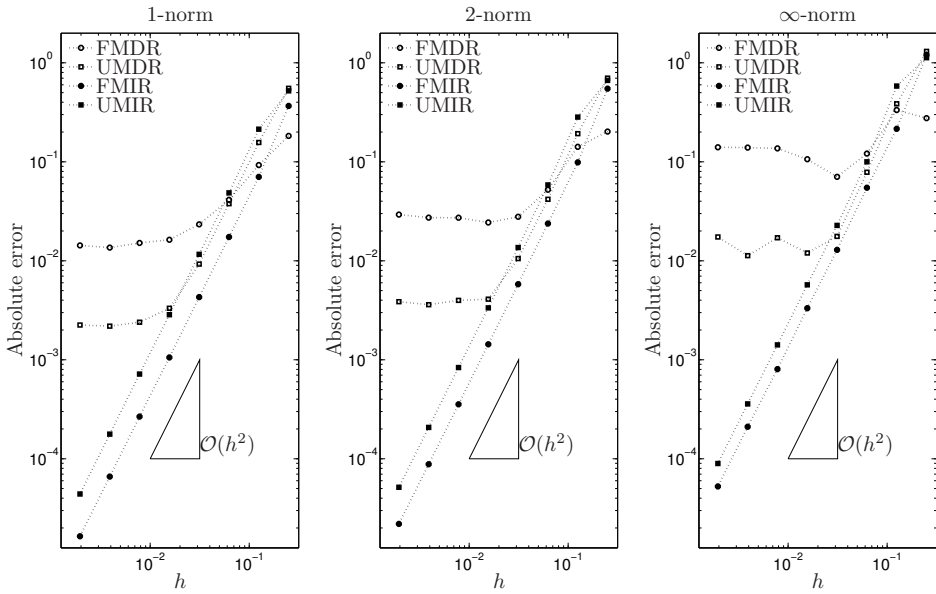
All methods show initially convergence for both test cases and both meshes, but eventually the FMDR method diverges. The UMDR method does diverge for the circular problem on both meshes, but no divergence is directly apparent for the star test case. We can however see that the UMDR method has a slightly larger error in all three norms than the UMIR method for the smallest mesh size tested, which may indicate the start of divergence. Both indirect recovery methods, FMIR and UMIR, show convergence for the tested mesh sizes, although differences in experimental order are present. On the regular mesh second order accuracy is obtained for both test cases, but on the equilateral mesh the circle test case shows eventually a first order rate of convergence in the ∞ -norm. This is however not (yet) observed for the star test case. As the ∞ -norm is one of the strictest norms, we expect the first order convergence to occur also for the star test case for finer meshes.

As both the FMIR and the UMIR methods perform equally well to recover the sum-curvature for these test cases, we propose to use the Unfitted Mesh Indirect Method, as the normals calculated using Equation (6.25) are needed in subsequent steps of the algorithm and are directly used in calculating the sum-curvature. We do however stress that this is a specific choice for our application to reduce the computational costs and the FMIR method may be better or more suitable for other applications. We also note that to reduce the computational cost, we only calculate the sum-curvature on the unfitted mesh in those points that are needed to perform the linear interpolation to the points on the boundary.

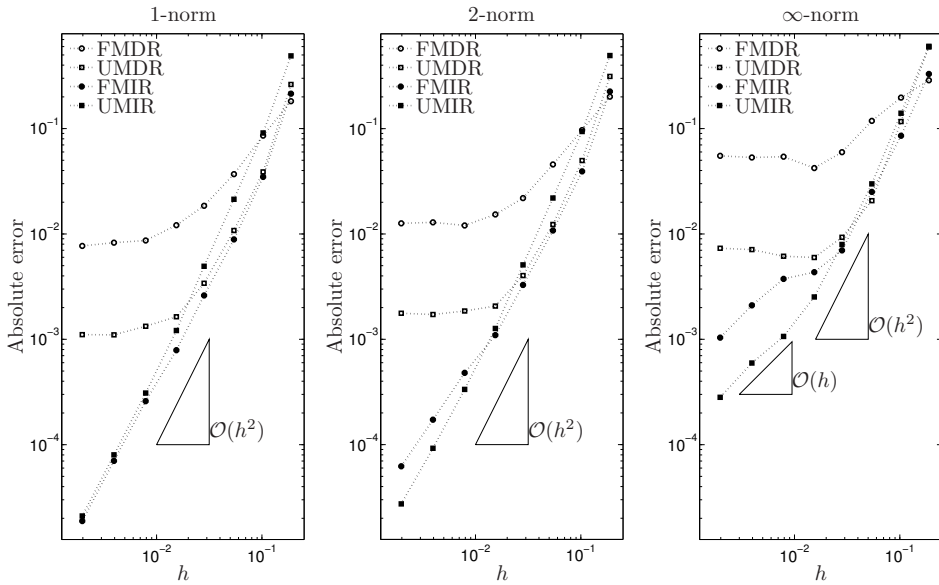
6.4.2 The need for and effect of smoothing

To show the solution $v_n(\mathbf{x}, t)$ with the use of the method proposed in Section 6.3.3, we will compute the normal velocity $v_n(\mathbf{x}, t)$ at several instances for the dissolution of a circular Mg_2Si precipitate located within an aluminium matrix. We choose the computational domain as $[-150, 150]^2$ in nanometers (nm) and the initial radius of the precipitate as 50 nm. The other needed parameters can be found within Table 6.1 and are representative at 400°C. We triangulate the computational domain using equilateral triangles with an average mesh size of 19 nm and refine the mesh locally three times in bands with a width of two times the current average mesh size around the zero contour of the (current) level set function.

We first calculate the initial condition following Sections 6.2.3 and 6.3.3, which results in the normal velocity and concentrations shown in Figure 6.4(a). The results clearly show a larger periodic behaviour contaminated with high frequency numerical artefacts. The concentrations shown are nearly constants, which in combination

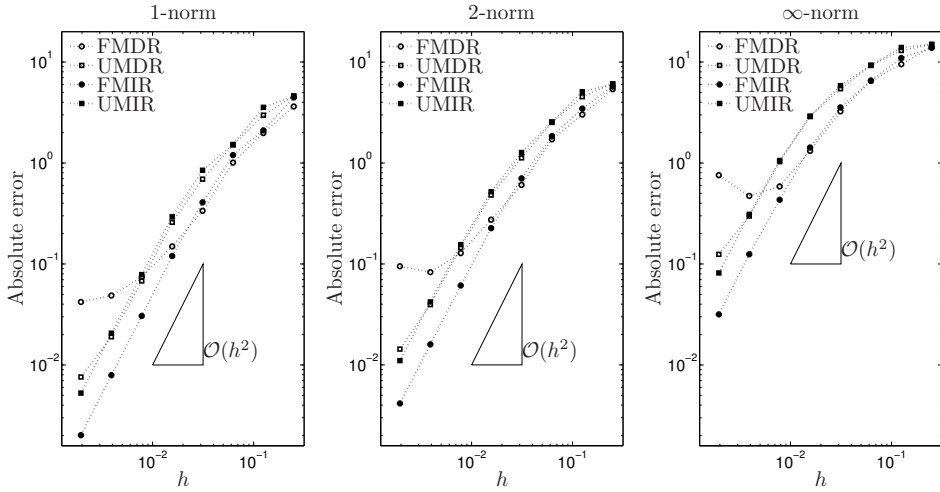


(a) Results for the regular mesh.

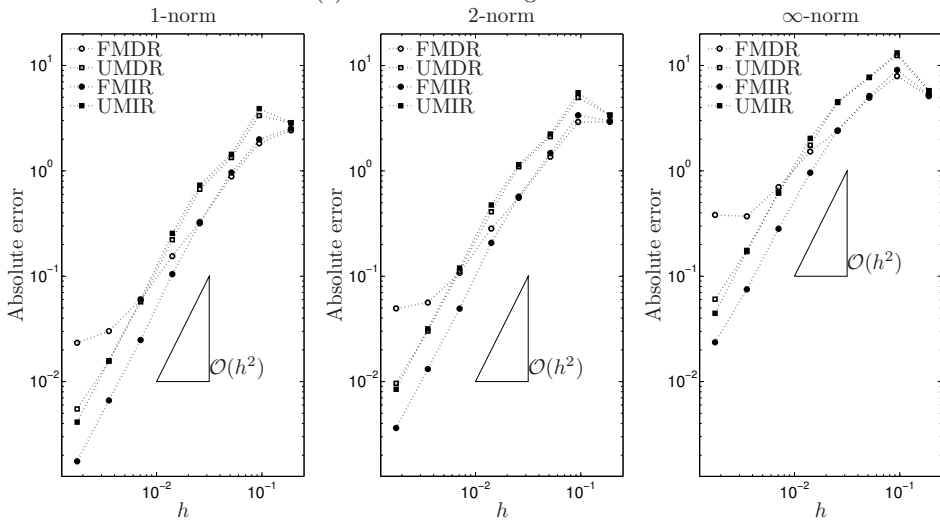


(b) Results for the equilateral mesh.

Figure 6.2: *Sum-curvature convergence results for the circle test case on several meshes. Shown are the absolute errors in the discrete 1-norm, 2-norm and ∞ -norm versus the minimum edge length h .*



(a) Results for the regular mesh.



(b) Results for the equilateral mesh.

Figure 6.3: *Sum-curvature convergence results for the star test case on several meshes. Shown are the absolute errors in the discrete 1-norm, 2-norm and ∞ -norm versus the minimum edge length h .*

Parameter	Value	Unit
c_{Mg}^p	$5.1882 \cdot 10^4$	mol/m ³
c_{Si}^p	$2.5941 \cdot 10^4$	mol/m ³
c_{Mg}^0	0	mol/m ³
c_{Si}^0	0	mol/m ³
K^∞	0.0256	
ζ	0	nm
D_{Mg}	$1.0626 \cdot 10^5$	nm ² /s
D_{Si}	$2.0642 \cdot 10^3$	nm ² /s
K_{Mg}	$2.6239 \cdot 10^5$	nm/s
K_{Si}	$5.0974 \cdot 10^3$	nm/s
M	$9.9987 \cdot 10^4$	mol/m ³

Table 6.1: *Physical parameters used for the dissolution of a Mg₂Si precipitate in an aluminium matrix.*

with the imposed Dirichlet condition leads to a larger normal diffusive flux along the boundary $\Gamma(0)$ at points closer to the outer boundary of $\Omega_D(0)$. Equation (6.2) then shows that at those points also a higher normal velocity should be expected. The results for the normal velocity shows that the larger periodic behaviour is in good agreement with the shape of the domain and the particle, as higher values of v_n are obtained at parts of the interface which are close to the outer boundary.

To remove the numerical artifacts, appearing as high frequency oscillations, we will apply Laplace smoothing of the form

$$-\mu \Delta_\Gamma \tilde{c}_e(\mathbf{x}, t^{\tau+1}) + \tilde{c}_e(\mathbf{x}, t^{\tau+1}) = c_e(\mathbf{x}, t^{\tau+1}) \quad \text{for } e \in \{\text{Mg}, \text{Si}\}, \quad (6.36)$$

to the concentrations along $\Gamma(0)$, with Δ_Γ the Laplace-Beltrami operator on $\Gamma(0)$ and $\mu \geq 0$ an appropriate smoothing value. This smoothing step is applied within each of the Newton iterations and the needed Jacobian entries are also smoothed using the same technique. For the initial condition empirically an optimal value of $\mu^* = 182$ is found. Figure 6.4(b) shows the results obtained for the normal velocity v_n and the concentrations c_{Mg} and c_{Si} with the use of the optimal value μ^* , super positioned over the original results. One can see that the smooth periodic results are captured, while the numerical artefacts are dampened satisfactory.

Next we will advect the level set function a single time step and calculate the normal velocity v_n and the concentrations. We will advect with the smoothed results in Figure 6.4(b). The results of these calculations can be found in Figure 6.5(a). Similar to the initial data some larger periodic behaviour is observed, which is highly influenced by numerical artefacts.

Using again Laplace smoothing by Equation (6.36) in each Newton step, empirically the optimal value of μ is found to be $\mu^* = 30$. Figure 6.4(b) shows the results obtained for the normal velocity v_n and the concentrations c_{Mg} and c_{Si} with the use of the optimal value μ^* , super positioned over the original results. One can see that the smooth periodic results are captured, while the numerical artefacts are dampened satisfactory, again in good agreement with the results for the initial conditions. We

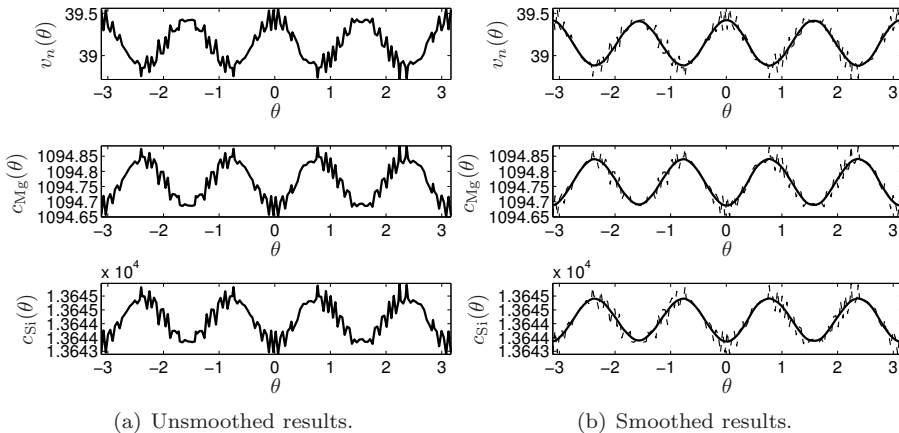


Figure 6.4: The calculated initial conditions without (a) and with smoothing (b) as a function of the polar angle θ . The optimal value of μ is found to be $\mu^* = 182$.

do however note that the obtained results contain some smooth local details which are not of a periodic nature. We believe these small details originate from the advection of the level-set function and the mesh generation. The results however do seem reasonable. We also note that the concentrations are dampened slightly more with respect to the initial conditions, but we note that the maximum point-wise damping is less than 0.1 percent of the original noisy results.

In the previous two examples the parameter ζ was chosen as zero, which indicates a constant value for $K_\kappa^\infty(\mathbf{x}, t)$ and this value is expected to have little influence on the numerical artefacts. To show the effect of non-constant $K_\kappa^\infty(\mathbf{x}, t)$, we recalculate the initial condition from the initial example, but now take $\gamma = 0.295 \text{ J/m}^2$, which indicates $\zeta = 2.0318 \text{ nm}$ using Equation (6.7). We calculate $v_n(\mathbf{x}, 0)$ without any smoothing, with Laplace smoothing only on $c_e(\mathbf{x}, 0)$, $e \in \{\text{Mg}, \text{Si}\}$, with Laplace smoothing only on $K_\kappa^\infty(\mathbf{x}, 0)$ and with Laplace smoothing on both $c_e(\mathbf{x}, 0)$, $e \in \{\text{Mg}, \text{Si}\}$ and $K_\kappa^\infty(\mathbf{x}, 0)$. Figure 6.6 shows the obtained results.

If we compare Figure 6.6(a) with Figure 6.6(b), we see that smoothing of the concentrations has a positive effect on the results, similarly to the previous examples and obtain a slightly larger value, but of the same magnitude, for the optimal value μ^* as initially. Some high frequency oscillations however do remain, which cannot be removed by solely smoothing the concentrations. Comparison of Figure 6.6(a) with Figure 6.6(c) shows that smoothing solely K_κ^∞ has almost no effect on the results and we achieve an optimal value μ^* which is relatively large. Figure 6.6(d) shows the results obtained by smoothing both the concentrations and K_κ^∞ and leads to an optimal value of $\mu^* = 159$, which is slightly smaller compared to the optimal value for only smoothing of the concentrations, but still of the same magnitude. This is an indicator that the amplified numerical oscillations in the concentrations and K_κ^∞ have similar frequencies which can be dampened in a similar fashion. The results also indicate that if K_κ^∞ is not smoothed, the value of μ becomes larger to compensate for the remaining high frequency oscillations originating from K_κ^∞ .

Although the results in Figures 6.4, 6.5 and 6.6 indicate good results with the use

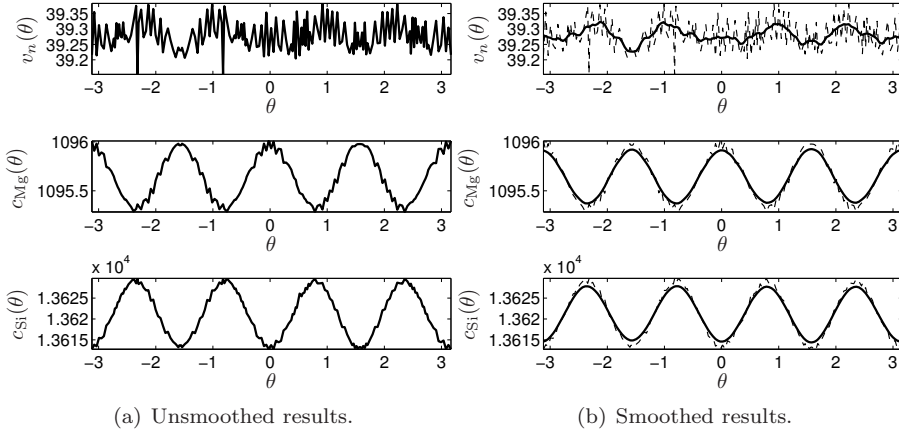


Figure 6.5: *The calculated results after a single time step without (a) and with smoothing (b) as a function of the polar angle θ . The optimal value of μ is found to be $\mu^* = 30$.*

of Laplace smoothing of the intermediate variables c_{Mg} , c_{Si} and K_κ^∞ , performing a single time step becomes expensive as manually an optimal value of μ must be found. To resolve this problem we have investigated the use of some criteria what defines an optimal smoothing parameter. This investigation has led to the minimisation problem

$$\mu^* = \arg \min_{\mu \in [0, \bar{\mu}]} \mathcal{L}(\mu), \quad (6.37)$$

with

$$\mathcal{L}(\mu) := \mathcal{L}_0(\mu) + \mathcal{L}_2(\mu), \quad (6.38)$$

$$\mathcal{L}_0(\mu) := \frac{\|v_{n,0}(\mathbf{x}, t^{\tau+1}) - v_{n,\mu}(\mathbf{x}, t^{\tau+1})\|_{2,\Gamma}}{\|v_{n,0}(\mathbf{x}, t^{\tau+1}) - \bar{v}_n\|_{2,\Gamma}} \quad (6.39)$$

$$\mathcal{L}_2(\mu) := -\lambda \frac{\|\Delta_\Gamma(v_{n,0}(\mathbf{x}, t^{\tau+1}) - v_{n,\mu}(\mathbf{x}, t^{\tau+1}))\|_{2,\Gamma}}{\|\Delta_\Gamma v_{n,0}(\mathbf{x}, t^{\tau+1})\|_{2,\Gamma}}, \quad (6.40)$$

in which $v_{n,0}(\mathbf{x}, t^{\tau+1})$ is the non-smoothed solution obtained with $\mu = 0$, $v_{n,\mu}(\mathbf{x}, t^{\tau+1})$ the solution obtained with $\mu \geq 0$, λ a non-negative penalty parameter, \bar{v}_n the average of $v_{n,0}(\mathbf{x}, t^{\tau+1})$ over $\Gamma(t^{\tau+1})$ and $\|\cdot\|_{2,\Gamma}$ the continuous 2-norm over $\Gamma(t^{\tau+1})$. Further investigation into this minimisation problem has shown that in some cases a value of μ was found that performs satisfactory in the first time steps to reduce the numerical artefacts, but in many cases the results still obtained high frequency oscillations at later stages.

We have also investigated the use of low-pass filters in combination with Lomb-Scargle periodograms [Hocke and Kämpfer, 2009] and the use of wavelet-thresholding [Kovac, 1998] to reduce the numerical artefacts. Both of these methods showed promising results, but contain some freedom in choosing smoothing parameters or

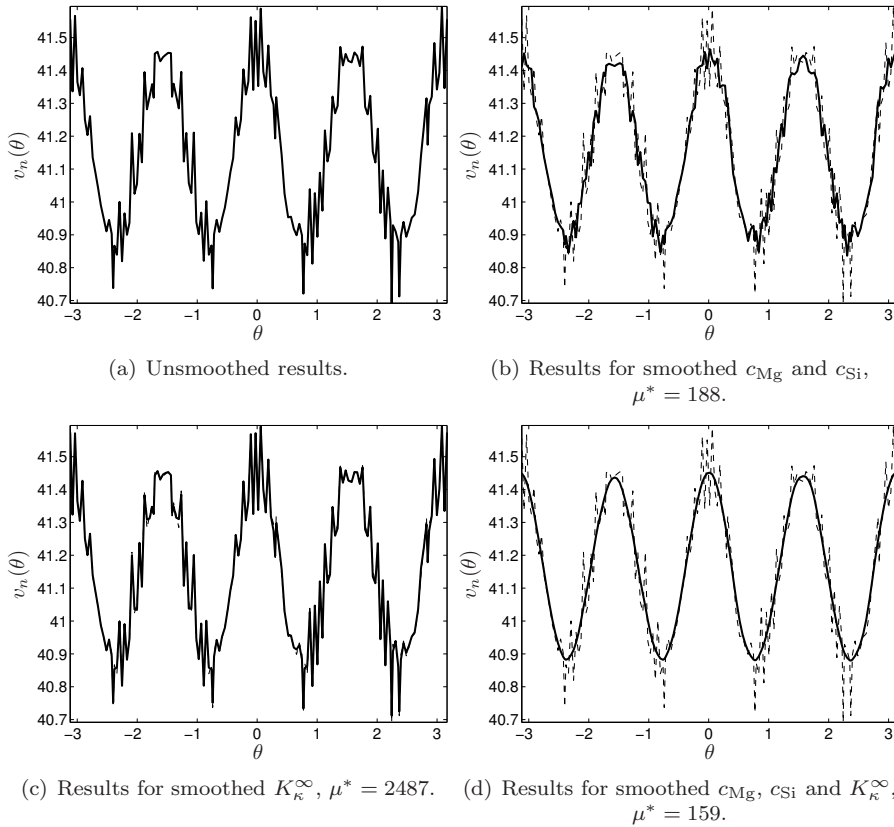


Figure 6.6: The calculated initial conditions with $\gamma = 0.295 \text{ J/m}^2$ without (a) and with smoothing (b),(c),(d) as a function of the polar angle θ . The optimal values of μ are given below the figures.

rely on assumptions[†] which may not be valid for this problem. Furthermore these methods currently require user intervention to obtain an optimally smoothed solution, which does not allow for an efficient algorithm to be possible at the moment. Therefore we recommend further studies in this problem, where possible directions are different smoothing techniques, other solution techniques or a possible reformulation of Equation (6.29) into a pde constraint minimisation problem, allowing techniques from this field to be applied.

6.5 Summary and Conclusion

We extended the physical model for the mixed-mode dissolution and growth of precipitates within a matrix from Chapter 5 to incorporate multiple chemical species. The kinetics governing growth and dissolution are influenced by the concentration gradient of all chemical elements near the precipitate interface and an interface reaction per chemical element. The model also incorporates the local sum-curvature of the interface and the influence of this sum-curvature on the equilibrium between the precipitate and the matrix. The shape and topology of the precipitate are again modelled using the level-set method [Osher and Sethian, 1988], where the moving interface is treated as a sharp transition.

We have proposed two techniques to obtain estimates for the sum-curvature of the local interface, based on patch recovery techniques commonly applied for gradient recovery. We have shown experimental convergence for one of recovery techniques, which relies on repeated application of the gradient recovery techniques. The order of experimental convergence is initially second order in mesh size and reduces for some of the cases to first order convergence.

In Section 6.3.3 we developed a Newton-based algorithm to obtain the normal velocity of the interface and all concentrations. In Section 6.4.2 we have shown the results from this method and the severe numerical artefacts present within the obtained solutions. An investigation into Laplace smoothing of intermediate variables to reduce the numerical artefacts has shown that this approach has possibilities, but leads to an algorithm which requires user interaction in every time step. Therefore we recommend further studies to solve this problem.

Bibliography

- J.-O. Andersson, T. Helander, L. Höglund, P. Shi and B. Sundman. Thermo-Calc & DICTRA, computational tools for materials science. *Calphad*, 26(2):273–312, 2002.
- R. Courant, K. Friedrichs and H. Lewy. Über die partiellen Differenzgleichungen der mathematischen Physik. *Mathematische Annalen*, 100:32–74, 1928.
- C.J. Heine. Mean-Curvature Reconstruction with Linear Finite Elements. European Numerical Mathematics and Advanced Applications (ENUMATH), Lausanne, Switzerland, 2013.

[†]Such as white noise.

- C. Herring. Some Theorems on the Free Energies of Crystal Surfaces. Physical Review, 82:87–93, 1951.
- K. Hocke and N. Kämpfer. Gap filling and noise reduction of unevenly sampled data by means of the Lomb-Scargle periodogram. Atmospheric Chemistry and Physics, 9(12):4197–4206, 2009.
- E. Javierre. Numerical methods for vector Stefan models of solid-state alloys. PhD thesis, Delft University of Technology, The Netherlands, 2006.
- A. Kovac. Wavelet Thresholding for Unequally Time-Spaced Data. PhD thesis, University of Bristol, Bristol, United Kingdom of Great Britain and Northern Ireland, 1998.
- M. Möller. Adaptive High-Resolution Finite Element Schemes. PhD thesis, Technische Universität Dortmund, 2008.
- S.J. Osher and R.P. Fedkiw. Level Set Methods and Dynamic Implicit Surfaces. Springer, New York, NY, United States of America, 1 edition, 2002.
- S.J. Osher and J.A. Sethian. Fronts propagating with curvature-dependent speed: Algorithms based on Hamilton-Jacobi formulations. Journal of Computational Physics, 79(1):12–49, 1988.
- D. den Ouden, A. Segal, F.J. Vermolen, L. Zhao, C. Vuik and J. Sietsma. Application of the level-set method to a mixed-mode driven stefan problem in 2D and 3D. Computing, 95(1):553–572, 2013.
- M. Perez. Gibbs-Thomson effects in phase transformations. Scripta Materialia, 52(8):709–712, 2005.
- M. Picasso, F. Alauzet, H. Borouchaki and P. George. A Numerical Study of Some Hessian Recovery Techniques on Isotropic and Anisotropic Meshes. SIAM Journal on Scientific Computing, 33(3):1058–1076, 2011.
- D.A. Porter and K.E. Easterling. Phase Transformations in Metals and Alloys. Chapman & Hall, London, United Kingdom of Great Britain and Northern Ireland, 2nd edition, 1992.
- B. Straumal, Ya. Kucherinenko and B. Baretzky. 3-Dimensional Wulff Diagrams for $\Sigma 3$ Grain Boundaries in Cu. Reviews on Advanced Materials Science, 7:23–31, 2004.
- C. Ünsulan and A. Erçil. Conversions between parametric and implicit forms using polar/spherical coordinate representations. Computer Vision and Image Understanding, 81:1–25, 2001.
- M.-G. Vallet, C.-M. Manole, J. Dompierre, S. Dufour and F. Guibault. Numerical comparison of some Hessian recovery techniques. International Journal for Numerical Methods in Engineering, 72(8):987–1007, 2007.

-
- F.J. Vermolen. On Similarity Solutions and Interface Reactions for a Vector-Valued Stefan Problem. Nonlinear Analysis: Modelling and Control, 12:269–288, 2007.
- C. Vuik. Phase Change Analysis and Jozef Stefan. In J.C. Crepeau, editor, Jozef Stefan: His Scientific Legacy on the 175-th Anniversary of His Birth, pages 166–183, Bussum, The Netherlands, 2013. Bentham Science Publishers.
- Z. Zhang and A. Naga. A new finite element gradient recovery method: Superconvergence property. SIAM Journal on Scientific Computing, 26(4):1192–1213, 2005.

Chapter 7

Conclusions and recommendations

7.1 Introduction

The primary focus of this thesis is on the development of models that describe the nucleation and growth of precipitates. We divided this focus into two parts, first by considering models describing the evolution of size distributions of precipitates and by subsequently investigating models with a primary focus on the size and shape evolution of single precipitates. In this chapter we will briefly summarise the results and conclusions reached on each subject. Finally we will identify several remaining and open problems and suggest directions for future research.

7.2 Distributions

7.2.1 Conclusions

In Part I the KWN-model has been extended with the effects of elastic stress, which primarily leads to an increase of the nucleation rate and the mean radius of precipitates in the initial stages of nucleation and growth. As an effect, a smaller mean radius is attained due to a faster depletion of the matrix. We, furthermore, adapted the KWN model such that all chemical species occurring within the alloy influence the nucleation and growth of precipitates. The theoretical model introduced for the frequency of atomic attachment is the first of its kind in literature and shows reasonable values compared to other models, but has a better dependence on all chemical species. The incorporation of all chemical species within the equations for the growth rates and nucleation rates has led to a natural coupling between different precipitate phases and it has been shown that the occurrence of one precipitate phase can significantly influence other precipitate phases. Finally the KWN model has been combined with a hardness model for martensitic steels containing precipitates with a cubic shape, which nucleate near dislocations. With the use of this hardness model, we obtained

a fit to experimental results. The results show that these models can accurately be used to predict the hardness evolution due to precipitate hardening, solid solution strengthening and due to dislocation recovery.

7.2.2 Recommendations

Although we extended the KWN-model in several ways, it can still be improved significantly in several ways. A drawback of the KWN-model is its basic assumption of spherical precipitates. Although the extension of the nucleation rates for other parametric shapes such as cubes, disks and needles, can be done in a relatively straightforward way, obtaining growth rates for these shapes has not been done widely. In our opinion the following items must be obtained for any of the parametric shapes to obtain a first accurate description of growth rates:

- A description of the normal velocity at any point of the interface using the Zener approximation;
- A relation between the size evolution and the parameters describing the parameter shape;
- An extension of the Gibbs-Thomson effect for parametric precipitate shapes;
- An accurate solution technique to obtain the resulting rate of change of the shape parameters;
- An accurate numerical methodology to solve the (possible) higher-dimensional convection equations.

In order to improve the KWN-model we recommend future research along the points mentioned above.

Within the KWN-model the nucleation of precipitates is primarily modelled homogeneous and heterogeneous nucleation is simulated by using an effective interfacial energy. Although this treatment gives some formulas with a reasonable order of approximation for nucleation on grain boundaries and near dislocations, these equations cannot be applied to nucleation on dislocations or other precipitate phases, leaving this subject open for future research.

In the alloys studied within this thesis, only secondary phases are considered which directly nucleate at their stoichiometric composition. In other alloys, such as aluminium alloys, commonly a sequence of secondary phases occurs, in which one phase nucleates and transforms to the other precipitate phases at certain sizes. Since these transition sizes commonly depend on temperature and composition, the equations describing the size distributions of each of the phases become more complex and special care must be taken to numerically solve these equations. As many alloys contain precipitation sequences, we recommend further studies in this direction.

Finally, alloys often contain several primary phases, for example during the transformation from austenite to ferrite or vice versa during thermomechanical processing. In each of these primary phases precipitates can nucleate and grow and the primary phase around precipitates may change. These effects can also be included within the KWN-model, but again lead to more complex equations and numerical methods. To obtain a widely applicable KWN-model during thermomechanical processing, we suggest this subject for future research.

7.3 Interfaces

7.3.1 Conclusions

In Part II we have analysed a mixed-mode model for the size evolution of arbitrarily shaped precipitates based on several chemical elements. The proposed meshing algorithm, based on the current level-set function gives good meshes on which the solutions exhibit first order experimental convergence with respect to mesh size. The proposed numerical methods for the binary model are able to capture the interface evolution accurately based on the interface reaction speed and interface curvature. Precipitate breakup is handled correctly as well. An important part within the level-set method is the reinitialisation of the level-set function to a signed-distance function, for which we have proposed a simple alternative method. This method makes directly use of the information available and is at least as efficient as other common methods for reinitialisation, but does not rely on the gradient of the level-set function. Furthermore, we introduced a patch-based curvature-recovery method, which exhibits a minimal experimental order of convergence of one. For the proposed numerical methods for the multi-component model we have shown a sensitivity to numerical artefacts, which can partially be reduced by application of Laplace smoothing. This however does not lead to a robust method. Finally, an equation for the value of the interface reaction speed has been proposed which has led to realistic results.

7.3.2 Recommendations

As the proposed numerical methods for the multi-component precipitate size evolution model are subject to a sensitivity to numerical artefacts, we recommend further studies for this problem. Possible solution direction are:

- Different smoothing techniques;
- A different solution approach, such as a different finite element basis;
- A reformulation of the posed problem, allowing for different techniques to be used.

Although we showed an experimental order of convergence for the proposed curvature-recovery method, an exact order of convergence would support the use of the method greatly. We therefore pose the proof of convergence as an open problem.

We introduced an equation for the reaction interface speed, which leads to a first approximation of this parameter. Since this parameter can also be related to the Gibbs free energy and the interface mobility, we recommend further studies in obtaining a relation between these parameters and the interface reaction speed.

Appendix A

Proof of Proposition 2.1

In Section 2.2.2 we stated the following proposition:

Proposition 2.1. *If the system is not in equilibrium the no-growth radius \hat{r} is only equal to the critical radius for nucleation r^* under the following assumptions:*

- 2.1. *The elements within the system are considered to be of equal molar mass, or equivalent that $x_m/x_m^e = C_m/C_m^e$ holds, in Equation (2.18);*
- 2.2. *The precipitates consist of a single solute element, that is $x_p \equiv 1$;*
- 2.3. *The free energy ΔG is solely influenced by the chemical volume free energy and the interface energy.*

In all other cases $\hat{r} \neq r^$ will hold.*

Proof of Proposition 2.1. To prove our claims assume 2.1.-2.3. as stated above. Assumptions 2.1. and 2.2. cause Equation (2.18) to become

$$\Delta g_v = \frac{RT}{V_m^p} \ln \left(\frac{C_m}{C_m^e} \right). \quad (\text{A.1})$$

Using Equation (2.16) and assumption 2.3., we obtained

$$r^* = \frac{2\gamma V_m^p}{RT} \left[\ln \left(\frac{C_m}{C_m^e} \right) \right]^{-1}, \quad (\text{A.2})$$

This appendix is based on the article:

D. den Ouden, F.J. Vermolen, L. Zhao, C. Vuik and J. Sietsma. Modelling of particle nucleation and growth in binary alloys under elastic deformation: An application to a Cu-0.95 wt%Co alloy. *Computational Materials Science*, 50(8):2397–2410, 2011a.

which is identical to Equation (2.25), proving that under assumptions 2.1.-2.3. $r^* = \hat{r}$.

To prove the uniqueness of $r^* = \hat{r}$ under the three assumptions, note that $r^* = \hat{r}$ should fail if at least one of the assumptions is violated. For each of the seven possible combinations of failed assumptions below is a proof stated that $r^* \neq \hat{r}$.

Case I - Only assumption 2.1. is violated: Due to assumption 2.2., we have

$$\Delta g_v = \frac{RT}{V_m^p} \ln \left(\frac{x_m}{x_m^e} \right). \quad (\text{A.3})$$

This can be rewritten as

$$\Delta g_v = \frac{RT}{V_m^p} \ln \left(\frac{C_m}{C_m^e} \right) + \frac{RT}{V_m^p} \ln (f(p, q)), \quad (\text{A.4})$$

in which $p = C_m/C_m^e$ and $q = M_2/M_1$, with M_2 and M_1 , respectively, the molar mass of the solvent and the solute element, and $f(p, q)$ defined by

$$f(p, q) = \frac{(q-1)C_m^e + 100}{p(q-1)C_m^e + 100}. \quad (\text{A.5})$$

For this function f , it can be shown that the sign of $(p-1)(q-1)$ is of importance to the value of f . If $(p-1)(q-1)$ is negative, $f(p, 1)$ will be larger than 1, and if $(p-1)(q-1)$ is positive, $f(p, 1)$ will be smaller than 1. This indicates that we must have

- If $(p-1)(q-1) > 0$, then $\Delta g_v < \frac{RT}{V_m^p} \ln \left(\frac{C_m}{C_m^e} \right)$;
- If $(p-1)(q-1) < 0$, then $\Delta g_v > \frac{RT}{V_m^p} \ln \left(\frac{C_m}{C_m^e} \right)$;

and as a consequence by Equation (2.16)

- If $(p-1)(q-1) > 0$, then $r^* > \hat{r}$;
- If $(p-1)(q-1) < 0$, then $r^* < \hat{r}$.

which proves that if assumption 2.1. is violated, we cannot have $r^* = \hat{r}$.

Case II - Only assumption 2.2. is violated: If we apply assumption 2.1. we obtain

$$\Delta g_v = \frac{RT}{V_m^p} x_p \ln \left(\frac{C_m}{C_m^e} \right) + \frac{RT}{V_m^p} (1-x_p) \ln \left(\frac{100-C_m}{100-C_m^e} \right). \quad (\text{A.6})$$

For the latter part of this equation, it can be shown that if $C_m^e > C_m$, Δg_v is positive and if $C_m^e < C_m$, Δg_v is negative. Using the fact that $0 < x_p < 1$, we have, if $C_m^e < C_m$, that

$$(1-x_p) \ln \left(\frac{C_m}{C_m^e} \right) > (1-x_p) \ln \left(\frac{100-C_m}{100-C_m^e} \right). \quad (\text{A.7})$$

This expression can be rewritten, using Equation (2.18) as

$$\frac{RT}{V_m^p} \ln \left(\frac{C_m}{C_m^e} \right) > \Delta g_v. \quad (\text{A.8})$$

As a result, we have by Equations (2.16) and (2.25):

$$\hat{r} < r^*. \quad (\text{A.9})$$

Similarly if $C_m^e > C_m$, we have

$$(1 - x_p) \ln \left(\frac{C_m}{C_m^e} \right) < (1 - x_p) \ln \left(\frac{100 - C_m}{100 - C_m^e} \right), \quad (\text{A.10})$$

Which can be rewritten, using Equation (2.18) as

$$\frac{RT}{V_m^p} \ln \left(\frac{C_m}{C_m^e} \right) < \Delta g_v. \quad (\text{A.12})$$

Hence, from Equations (2.16) and (2.25), it follows that

$$\hat{r} > r^*. \quad (\text{A.13})$$

The above arguments proves that if assumption 2.2. is violated, we cannot have $r^* = \hat{r}$.

Case III - Only assumption 2.3. is violated: If assumption 2.3. is false, and we apply assumptions 2.1. and 2.2. to Equations (2.18) and (2.16), then we obtain:

$$r^* = \frac{2\gamma}{\frac{RT}{V_m^p} \ln \left(\frac{C_m}{C_m^e} \right) + \Delta g_0}, \quad (\text{A.14})$$

in which Δg_0 contains all other modelled energy density terms. If Δg_0 has a negative sign, then by Equations (2.16) and (2.25) we have that $r^* > \hat{r}$, whereas if Δg_0 has a positive sign, then we have $r^* < \hat{r}$ by the same equations. This proves that if assumption 2.3. is violated, we cannot have $r^* = \hat{r}$.

Case IV - Only assumptions 2.1. and 2.2. are violated: Similar to Case II, we have by failure of assumption 2.2.

$$\ln \left(\frac{C_m}{C_m^e} \right) \neq x_p \ln \left(\frac{C_m}{C_m^e} \right) + (1 - x_p) \ln \left(\frac{100 - C_m}{100 - C_m^e} \right). \quad (\text{A.15})$$

By failure of assumption 2.1., similar as in Case I, we also have

$$\ln \left(\frac{C_m}{C_m^e} \right) \neq \ln \left(\frac{x_m}{x_m^e} \right), \quad (\text{A.16})$$

$$\ln \left(\frac{100 - C_m}{100 - C_m^e} \right) \neq \ln \left(\frac{1 - x_m}{1 - x_m^e} \right). \quad (\text{A.17})$$

Combination of the three inequalities above give that $r^* \neq \hat{r}$, if assumptions 2.1. and 2.2. are violated.

Case V - Only assumptions 2.1. and 2.3. are violated: Due to violation of assumption 2.3., we have

$$\Delta g_v \neq \Delta g_v + \Delta g_0, \quad (\text{A.18})$$

where Δg_0 is as defined in Case III. This inequality in combination with those from Case I, we have that $r^* \neq \hat{r}$ if assumptions 2.1. and 2.3. are violated.

Case VI - Only assumptions 2.2. and 2.3. are violated: Due to violation of assumption 2.3., we have

$$\Delta g_v \neq \Delta g_v + \Delta g_0, \quad (\text{A.19})$$

where Δg_0 is as defined in Case III. This inequality in combination with those from Case II, we have that $r^* \neq \hat{r}$ if assumptions 2.2. and 2.3. are violated.

Case VII - Assumption 2.1.,2.2. and 2.3. are violated: Due to violation of assumption 2.3., we have

$$\Delta g_v \neq \Delta g_v + \Delta g_0, \quad (\text{A.20})$$

where Δg_0 is as defined in Case III. This inequality in combination with those from Case IV, we have that $r^* \neq \hat{r}$ if all three assumptions are violated.

If we denote by E the equivalence of r^* and \hat{r} , and by $A1, A2, A3$ assumptions 2.1.-2.3., it can be shown that Cases I, IV, V and VII together proof that $\neg A1 \rightarrow \neg E$, that Cases II, IV, VI and VII together proof that $\neg A2 \rightarrow \neg E$ and that Cases III, V, VI and VII together proof that $\neg A3 \rightarrow \neg E$. Furthermore, using Theorem 2.2.3 of Burris [1998], we can show that

$$(\neg A1 \rightarrow \neg E) \wedge (\neg A2 \rightarrow \neg E) \wedge (\neg A3 \rightarrow \neg E), \quad (\text{A.21})$$

is equivalent with

$$E \rightarrow (A1 \wedge A2 \wedge A3). \quad (\text{A.22})$$

Above we have shown the truth of (A.21), which proves that (A.22) is true, or equivalent that $r^* = \hat{r}$ implies that assumptions 2.1. to 2.3. hold. Together with the prove that $r^* = \hat{r}$ holds if assumptions 2.1. to 2.3. hold, the validity of Proposition 2.1 is shown. \square

Bibliography

S.N. Burris. Logic for Mathematics and Computer Science. Prentice Hall, Upper Saddle River, NJ, United States of America, 1998.

Appendix B

Motivation of Equation (3.13)

In Aaronson et al. [1970] a plausible formula for the volume free energy density associated with precipitate nucleation in dilute solution binary alloys:

$$\Delta g_v = -\frac{R_g T}{V_p^{\text{mole}}} \left[x_p \ln \left(\frac{x_m}{x_m^{p/m}} \right) + (1 - x_p) \ln \left(\frac{1 - x_m}{1 - x_m^{p/m}} \right) \right], \quad (\text{B.1})$$

in which x_p refers to the mole fraction of solute in the precipitate phase p at the precipitate/matrix interface, $x_m^{p/m}$ to the mole fraction of solute in the matrix phase m at the precipitate/matrix interface and x_m to the mole fraction of solute in the matrix phase m . R , T and V_p^{mole} , respectively, are the gas constant, the absolute temperature and the molar volume of the precipitate phase. In their motivation, they restricted themselves to a binary alloy in which precipitates nucleate at a known composition. The original discussion in Aaronson et al. [1970] can be adapted to calculate the volume free energy density associated with the nucleation of precipitates in a multi-component alloy, by making similar assumptions as in Aaronson et al. [1970].

In the discussion in Aaronson et al. [1970], the following three main assumptions are made:

This appendix is based on the article:

D. den Ouden, L. Zhao, C. Vuik, J. Sietsma and F.J. Vermolen. Modelling precipitate nucleation and growth with multiple precipitate species under isothermal conditions: Formulation and analysis. *Computational Materials Science*, 79:933–943, 2013b.

- B.1. A single precipitate has the same chemical composition as the entire precipitate phase at equilibrium.
- B.2. The composition of the matrix phase is uniform throughout the system.
- B.3. Only two species are present in the system, the solute and the solvent.

We now drop the third assumption, but the first two assumptions are maintained. In the remainder of the Appendix, we follow the derivation of Equation (B.1) as originally given in Aaronson et al. [1970] to motivate Equation (3.13), which provides the multi-component equivalence of Equation (B.1).

Assume one mole of the matrix phase m consists of $n \in \mathbb{N}$ elements with mole fractions $x_{m,e}, e \in \mathbb{E}$ for which $\sum_{e \in \mathbb{E}} x_{m,e} = 1$ and \mathbb{E} is the set of atoms present within the system. From this phase, A moles of the precipitate phase p nucleate, resulting in a system containing A moles of the precipitate phase and $B = 1 - A$ moles of a new matrix phase m_1 :



The phase p has a known and fixed composition with mole fractions $x_{p,e}, e \in \mathbb{E}$ at the precipitate/matrix interface, for which $\sum_{e \in \mathbb{E}} x_{p,e} = 1$, and the phase m_1 with resulting mole fractions $x_{m_1,e}, e \in \mathbb{E}$ for which $\sum_{e \in \mathbb{E}} x_{m_1,e} = 1$. A simple mass balance gives

$$Bx_{m_1,e} = x_{m,e} - Ax_{p,e}. \quad (\text{B.3})$$

The volume free energy change ΔG_v associated with phase transformation (B.2) is determined by

$$\Delta G_v = AG_p + BG_{m_1} - G_m. \quad (\text{B.4})$$

in which G_p, G_{m_1}, G_m are the molar free energies of the different phases. For any phase j , the molar free energy can be determined by the finite sum

$$G_j = \sum_{e \in \mathbb{E}} x_{j,e} \bar{G}_{j,e}, \quad (\text{B.5})$$

where $\bar{G}_{j,e}$ represents the partial molar free energy of element e in phase j . For $j = p$ these energies are taken, similar to the related mole fractions, in phase p at the precipitate/matrix interface. Using the above formula three times in (B.4) gives

$$\Delta G_v = \sum_{e \in \mathbb{E}} Ax_{p,e} \bar{G}_{p,e} + Bx_{m_1,e} \bar{G}_{m_1,e} - x_{m,e} \bar{G}_{m,e}. \quad (\text{B.6})$$

Due to the assumption on the composition of the precipitate being in equilibrium composition, we may replace the partial molar free energy $\bar{G}_{p,e}$ with $\bar{G}_{m,e}^{p/m}$, which is the partial molar free energy of element e in phase m at the precipitate/matrix (p/m) interface. Using this substitution and the results from the mass balance (B.3), formula (B.6) transforms to

$$\begin{aligned} \Delta G_v = & \sum_{e \in \mathbb{E}} Ax_{p,e} \left(\bar{G}_{m,e}^{p/m} - \bar{G}_{m_1,e} \right) \\ & + \sum_{e \in \mathbb{E}} x_{m,e} \left(\bar{G}_{m_1,e} - \bar{G}_{m,e} \right). \end{aligned} \quad (\text{B.7})$$

Based on the used assumptions, we express the partial molar free energies and the molar free energies of the pure elements in the various phases in (B.7) in terms of the activities of the elements in the different phases by using the formula

$$\bar{G}_{j,e} = G_{j,e} + R_g T \ln(a_{j,e}), \quad (\text{B.8})$$

in which $a_{j,e}$ represents the activity of element e in phase j . A superscript is introduced for $a_{j,e}$ if a specific location, being a phase or an interface, is described. Further, we assume that $G_{m,e} \approx G_{m_1,e}$. Replacing the partial molar free energies in (B.7) and rewriting gives

$$\begin{aligned} \Delta G_v = & R_g T A \sum_{e \in \mathbb{E}} x_{p,e} \ln \left(\frac{a_{m,e}^{p/m}}{a_{m_1,e}} \right) \\ & + R_g T \sum_{e \in \mathbb{E}} x_{m,e} \ln \left(\frac{a_{m_1,e}}{a_{m,e}} \right). \end{aligned} \quad (\text{B.9})$$

Division by the number of moles A of phase p and the molar volume V_p^{mole} of phase p results in the formula

$$\begin{aligned} \Delta \tilde{g}_v = & \frac{R_g T}{V_p^{\text{mole}}} \sum_{e \in \mathbb{E}} x_{p,e} \ln \left(\frac{a_{m,e}^{p/m}}{a_{m_1,e}} \right) \\ & + \frac{R_g T}{AV_p^{\text{mole}}} \sum_{e \in \mathbb{E}} x_{m,e} \ln \left(\frac{a_{m_1,e}}{a_{m,e}} \right), \end{aligned} \quad (\text{B.10})$$

for the volume free energy density. As A is usually small, we can take the limit of A to zero of the above formula.

First we need some preliminary calculations. Note that if we let A , the number of moles of phase p that nucleate, tend to zero, we have the following limit using (B.3) for arbitrary e :

$$\lim_{A \rightarrow 0} x_{m_1,e} = x_{m,e}. \quad (\text{B.11})$$

Due to this limit and due to the continuity of the expression, we will also have that $a_{m_1,e} \rightarrow a_{m,e}$ as A tends to zero. Using this fact we now take the limit for A to zero of (B.10):

$$\Delta g_v = \lim_{A \rightarrow 0} \Delta \tilde{g}_v \quad (\text{B.12})$$

$$\begin{aligned} = & \lim_{A \rightarrow 0} \left[\frac{R_g T}{V_p^{\text{mole}}} \sum_{e \in \mathbb{E}} x_{p,e} \ln \left(\frac{a_{m,e}^{p/m}}{a_{m,e}} \right) \right. \\ & \left. + \frac{R_g T}{AV_p^{\text{mole}}} \sum_{e \in \mathbb{E}} x_{m,e} \ln \left(\frac{a_{m_1,e}}{a_{m,e}} \right) \right] \end{aligned} \quad (\text{B.13})$$

$$\begin{aligned} = & \frac{R_g T}{V_p^{\text{mole}}} \sum_{e \in \mathbb{E}} x_{p,e} \ln \left(\frac{a_{m,e}^{p/m}}{a_{m,e}} \right) \\ & + \frac{R_g T}{V_p^{\text{mole}}} \lim_{A \rightarrow 0} \left[\frac{1}{A} \sum_{e \in \mathbb{E}} x_{m,e} \ln \left(\frac{a_{m_1,e}}{a_{m,e}} \right) \right]. \end{aligned} \quad (\text{B.14})$$

The latter limit is of an indeterminate form, but can be evaluated using l'Hôpital's Rule, provided the limit of the ratio of the derivatives exists:

$$= \frac{R_g T}{V_p^{\text{mole}}} \sum_{e \in \mathbb{E}} x_{p,e} \ln \left(\frac{a_{m,e}^{p/m}}{a_{m,e}} \right) \quad (\text{B.15})$$

$$+ \frac{R_g T}{V_p^{\text{mole}}} \lim_{A \rightarrow 0} \left[\frac{\frac{d}{dA} \left\{ \sum_{e \in \mathbb{E}} x_{m,e} \ln \left(\frac{a_{m_1,e}}{a_{m,e}} \right) \right\}}{\frac{d}{dA} \{A\}} \right]$$

$$= \frac{R_g T}{V_p^{\text{mole}}} \sum_{e \in \mathbb{E}} x_{p,e} \ln \left(\frac{a_{m,e}^{p/m}}{a_{m,e}} \right) \quad (\text{B.16})$$

$$+ \frac{R_g T}{V_p^{\text{mole}}} \lim_{A \rightarrow 0} \sum_{e \in \mathbb{E}} x_{m,e} \left[\frac{d}{dA} \left\{ \ln \left(\frac{a_{m_1,e}}{a_{m,e}} \right) \right\} \right].$$

If we differentiate the partial molar free energy of element e in any phase j , see Equation (B.8) with respect to A , we get

$$\frac{d\bar{G}_{j,e}}{dA} = \frac{dG_{j,e}}{dA} + R_g T \frac{d}{dA} [\ln(a_{j,e})]. \quad (\text{B.17})$$

Applying this to equation (B.16), using the definition of the derivative and pulling the summation within the limits, we get

$$\Delta g_v = \frac{R_g T}{V_p^{\text{mole}}} \sum_{e \in \mathbb{E}} x_{p,e} \ln \left(\frac{a_{m,e}^{p/m}}{a_{m,e}} \right) \quad (\text{B.18})$$

$$+ \frac{1}{V_p^{\text{mole}}} \lim_{A \rightarrow 0} \lim_{\Delta A \rightarrow 0} \left[\frac{\sum_{e \in \mathbb{E}} x_{m,e} (\Delta \bar{G}_{m,e} - \Delta \bar{G}_{m_1,e})}{\Delta A} \right].$$

The numerator of the fraction inside the double limit can be further simplified using the Gibbs-Duhem equation, from which it follows that

$$\Delta g_v = \frac{R_g T}{V_p^{\text{mole}}} \sum_{e \in \mathbb{E}} x_{p,e} \ln \left(\frac{a_{m,e}^{p/m}}{a_{m,e}} \right) \quad (\text{B.19})$$

$$+ \frac{1}{V_p^{\text{mole}}} \lim_{A \rightarrow 0} \lim_{\Delta A \rightarrow 0} \left[\frac{0}{\Delta A} \right], \quad (\text{B.20})$$

which immediately gives

$$\Delta g_v = \frac{R_g T}{V_p^{\text{mole}}} \sum_{e \in \mathbb{E}} x_{p,e} \ln \left(\frac{a_{m,e}^{p/m}}{a_{m,e}} \right). \quad (\text{B.21})$$

On basis of the dilute solution assumption we redefine (B.21) as

$$\Delta g_v = \frac{R_g T}{V_p^{\text{mole}}} \sum_{e \in \mathbb{E}} x_{p,e} \ln \left(\frac{x_{m,e}^{p/m}}{x_{m,e}} \right), \quad (\text{B.22})$$

or equivalently

$$\Delta g_v = -\frac{R_g T}{V_p^{\text{mole}}} \sum_{e \in \mathbb{E}} x_{p,e} \ln \left(\frac{x_{m,e}}{x_{m,e}^{p/m}} \right). \quad (3.13)$$

Note that Equation (3.13) reduces to Equation (B.1) for a binary alloy.

Bibliography

H.I. Aaronson, K.R. Kinsman and K.C. Russel. The volume free energy change associated with precipitate nucleation. Scripta Metallurgica, 4(2):101–106, 1970.

Appendix C

Derivation of Equation (3.37)

In Chapter 3 a formula for the effective attachment frequency λ_p^m was derived using a Continuous-Time Markov chain. To determining the value of λ_p^m , Equation (3.37)

$$t_p^* = \int_0^\infty t \sum_{j \in \mathcal{T}} \frac{dp_j}{dt}(t) dt, \quad (3.37)$$

has to be evaluated. In the following we give a derivation of Equation (3.37) and determine its value.

Assume a Continuous-Time Markov chain is given, consisting of \mathbb{S} unique states, of which a subset \mathcal{T} are terminating. Let T be the time at which the Continuous-Time Markov chain is in one of the terminating states. The cumulative distribution function $F_T(t)$ of T is given by

$$F_T(t) = \Pr(T \leq t) \quad (C.1)$$

$$= 1 - \Pr(T > t) \quad (C.2)$$

$$= 1 - \sum_{i \notin \mathcal{T}} p_i(t) \quad (C.3)$$

$$= \sum_{j \in \mathcal{T}} p_j(t), \quad (C.4)$$

where we have used in Equation (C.2) that if $T > t$, we are in one of the non-terminating states, and that $\|\mathbf{p}\|_1 = 1$ in Equation (C.4). The above gives that the probability density function $f_T(t)$ of T is given by

$$f_T(t) = \frac{dF_T}{dt}(t) = \sum_{j \in \mathcal{T}} \frac{dp_j}{dt}(t). \quad (C.5)$$

The expected time at which the Continuous-Time Markov chain is in one of the

terminating states is thus given by

$$t_p^* = \int_0^\infty t \sum_{j \in \mathcal{T}} \frac{dp_j}{dt}(t) dt. \quad (3.37)$$

The evaluation of Equation (3.37) can easily be achieved by renumbering of the states. Define \mathbb{T} to be the number of elements in \mathcal{T} and let $\mathbb{U} = \mathbb{S} - \mathbb{T}$. Renumber the states such that the first \mathbb{T} states are terminating and the last \mathbb{U} are transient. Furthermore, define $\mathcal{O}_{m \times n}$ as the $m \times n$ empty matrix, $\text{Id}_{m \times n}$ as the $m \times n$ identity matrix and $\mathbf{1}_{m \times n}$ as the $m \times n$ matrix filled with ones. The transition matrix Q has, after renumbering, the block form

$$Q = \left[\begin{array}{c|c} \mathcal{O}_{\mathbb{T} \times \mathbb{T}} & \mathcal{O}_{\mathbb{T} \times \mathbb{U}} \\ \hline R & S \end{array} \right], \quad (C.6)$$

with R a $\mathbb{U} \times \mathbb{T}$ matrix and S a $\mathbb{U} \times \mathbb{U}$ matrix. Due to the zero row sum of Q , we have the relation

$$\sum_{j=1}^{\mathbb{T}} R_{ij} = \sum_{j=1}^{\mathbb{U}} S_{ij}, \quad (C.7)$$

for R and S .

Let $\mathbf{p}(t)$ be the row vector $[p_1(t), \dots, p_{\mathbb{S}}(t)]$, where $p_i(t)$ is the probability to be in state i at time t . The probability vector $\mathbf{p}(t)$ is the solution of the initial value problem

$$\begin{cases} \frac{d\mathbf{p}}{dt}(t) = \mathbf{p}(t)Q, & \text{for } t > 0, \\ \mathbf{p}(t) = \mathbf{p}^0, \end{cases} \quad (C.8)$$

which has solution

$$\mathbf{p}(t) = \mathbf{p}^0 e^{Qt}. \quad (C.9)$$

Using Equations (C.6), (C.8) and (C.9), Equation (C.5) can be rewritten as fol-

lows:

$$f_T(t) = \sum_{j \in \mathcal{T}} \frac{dp_j}{dt}(t) \quad (\text{C.10})$$

$$= \frac{d\mathbf{p}}{dt} \begin{bmatrix} \mathbf{1}_{\mathbb{T} \times 1} \\ \emptyset_{\mathbb{U} \times 1} \end{bmatrix} \quad (\text{C.11})$$

$$= \mathbf{p}Q \begin{bmatrix} \mathbf{1}_{\mathbb{T} \times 1} \\ \emptyset_{\mathbb{U} \times 1} \end{bmatrix} \quad (\text{C.12})$$

$$= \mathbf{p}^0 e^{Qt} \begin{bmatrix} \emptyset_{\mathbb{T} \times \mathbb{T}} & \emptyset_{\mathbb{T} \times \mathbb{U}} \\ R & S \end{bmatrix} \begin{bmatrix} \mathbf{1}_{\mathbb{T} \times 1} \\ \emptyset_{\mathbb{U} \times 1} \end{bmatrix} \quad (\text{C.13})$$

$$= \mathbf{p}^0 \begin{bmatrix} \text{Id}_{\mathbb{T} \times \mathbb{T}} & \emptyset_{\mathbb{T} \times \mathbb{U}} \\ F(R, S, t) & e^{St} \end{bmatrix} \begin{bmatrix} \emptyset_{\mathbb{T} \times \mathbb{T}} & \emptyset_{\mathbb{T} \times \mathbb{U}} \\ R & S \end{bmatrix} \begin{bmatrix} \mathbf{1}_{\mathbb{T} \times 1} \\ \emptyset_{\mathbb{U} \times 1} \end{bmatrix} \quad (\text{C.14})$$

$$= \mathbf{p}^0 \begin{bmatrix} \text{Id}_{\mathbb{T} \times \mathbb{T}} & \emptyset_{\mathbb{T} \times \mathbb{U}} \\ F(R, S, t) & e^{St} \end{bmatrix} \begin{bmatrix} \emptyset_{\mathbb{T} \times 1} \\ R \mathbf{1}_{\mathbb{T} \times 1} \end{bmatrix} \quad (\text{C.15})$$

$$= \mathbf{p}^0 \begin{bmatrix} \emptyset_{\mathbb{T} \times 1} \\ e^{St} R \mathbf{1}_{\mathbb{T} \times 1} \end{bmatrix} \quad (\text{C.16})$$

$$= \mathbf{p}_U^0 e^{St} R \mathbf{1}_{\mathbb{T} \times 1} \quad (\text{C.17})$$

$$= -\mathbf{p}_U^0 e^{St} S \mathbf{1}_{\mathbb{U} \times 1}, \quad (\text{C.18})$$

where $F(R, S, t)$ is a $\mathbb{U} \times \mathbb{T}$ matrix and \mathbf{p}_U^0 the initial probability row vector of the transient states.

Using Equation (C.18), Equation (3.37) can be computed to be

$$t_p^* = \int_0^\infty t \sum_{j \in \mathcal{T}} \frac{dp_j}{dt}(t) dt \quad (\text{3.37})$$

$$= - \int_0^\infty t \mathbf{p}_U^0 e^{St} S \mathbf{1}_{\mathbb{U} \times 1} dt \quad (\text{C.19})$$

$$= -\mathbf{p}_U^0 \int_0^\infty t e^{St} S dt \mathbf{1}_{\mathbb{U} \times 1} \quad (\text{C.20})$$

$$= -\mathbf{p}_U^0 S^{-1} \mathbf{1}_{\mathbb{U} \times 1}. \quad (\text{C.21})$$

Curriculum Vitae

Dennis den Ouden was born on October 21, 1983, in Lekkerkerk, the Netherlands. He received secondary education at the Krimpenerwaardcollege in Krimpen aan den IJssel, the Netherlands, 1996-2003. He obtained his Bachelor of Science Applied Mathematics degree at the Delft University of Technology, the Netherlands, in 2007. He obtained his Master of Science Applied Mathematics degree at the Delft University of Technology, the Netherlands, in 2009.

He worked for the Materials Innovation Institute for 4 years, from 2010 to 2013, during which he conducted research for his Ph.D study at the Delft University of Technology. There, he was a member of the Numerical Analysis group within the Delft Institute of Applied Mathematics and of the Metals Processing, Microstructure and Properties group within the department of Materials Science and Engineering. He was supervised by prof.dr.ir. C. Vuik, prof.dr.ir. J. Sietsma, dr.ir. F.J. Vermolen and dr. L. Zhao.

Publications

Journal papers

- D. den Ouden, F.J. Vermolen, L. Zhao, C. Vuik and J. Sietsma. Modelling of particle nucleation and growth in binary alloys under elastic deformation: An application to a Cu-0.95 wt%Co alloy. Computational Materials Science, 50(8): 2397–2410, 2011a.
- D. den Ouden, F.J. Vermolen, L. Zhao, C. Vuik and J. Sietsma. Mathematical Modelling of NbC Particle Nucleation and Growth in an HSLA Steel under Elastic Deformation. Solid State Phenomena, 172–174:893–898, 2011b.
- D. den Ouden, A. Segal, F.J. Vermolen, L. Zhao, C. Vuik and J. Sietsma. Application of the level-set method to a mixed-mode driven stefan problem in $2D$ and $3D$. Computing, 95(1):553–572, 2013a.
- D. den Ouden, L. Zhao, C. Vuik, J. Sietsma and F.J. Vermolen. Modelling precipitate nucleation and growth with multiple precipitate species under isothermal conditions: Formulation and analysis. Computational Materials Science, 79:933–943, 2013c.
- C.E.I.C. Öhlund, D. den Ouden, J. Weidow, M. Thuvander and S.E. Offerman. Modelling the evolution of multiple hardness components during tempering of Fe-C-Mn-Ti martensite. ISIJ International, 2015. ACCEPTED FOR PUBLICATION.

Refereed proceedings of international conferences

- D. den Ouden, F.J. Vermolen, L. Zhao, C. Vuik and J. Sietsma. Application of the level-set method to a mixed-mode and curvature driven stefan problem. In Andrea Cangiani, Ruslan L. Davidchack, Emmanuil Georgoulis, Alexander N. Gorban, Jeremy Levesley and Michael V. Tretyakov, editors, Numerical Mathematics and Advanced Applications 2011, pages 141–148. Springer, Berlin, Germany, 2013b.

Talks at international conferences

- Application of the level-set method to a mixed-mode driven Stefan problem. European Numerical Mathematics and Advanced Applications (ENUMATH), Leicester, United Kingdom of Great Britain and Northern Ireland, 2011.
- Application of the Level-Set Method to a Mixed-Mode Driven Stefan Problem: A Finite-Element Approach. European Seminar on Computing, Pilsen, Czech Republic, 2012.
- Application of the level-set method to a multi-component Stefan problem. European Numerical Mathematics and Advanced Applications (ENUMATH), Lausanne, Switzerland, 2013.
- Multiphase physics with a transport phenomenon in parametric space. Modeling and Simulation of Transport Phenomena (MoST), Treis-Karden, Germany, 2014.

Other talks

- Application of the Level-Set Method to a Mixed-Mode Driven Stefan Problem: A Finite-Element Approach. M2i Conference, Noord-wijkerhout, The Netherlands, 2012b.
- Application of the Level-Set Method to a Mixed-Mode Driven Stefan Problem. Spring meeting Werkgemeenschap Scientific Computing, Amsterdam, The Netherlands, 2013.

Poster presentations at international conferences

- Mathematical modelling of NbC particle nucleation and growth in an HSLA steel under elastic deformation. International Solid-to-Solid Phase Transformation in Inorganic Materials Conferences (PTM2010), Avignon, France, 2010.

Other poster presentations

- Modelling of nucleation and growth of Nb-containing precipitates during thermo-mechanical processing in HSLA steels. M2i Conference, Noord-wijkerhout, The Netherlands, 2010.
- Application of the level-set method to a mixed-mode driven Stefan problem. Thirty-sixth Woudschoten conference, Werkgemeenschap Scientific Computing, Zutphen, The Netherlands, 2011.
- Modelling of nucleation and growth of Nb-containing precipitates during thermo-mechanical processing in HSLA steels. M2i Conference, Noord-wijkerhout, The Netherlands, 2011.

- Modelling of nucleation and growth of Nb-containing precipitates during thermo-mechanical processing in HSLA steels. M2i Conference, Noord-wijkerhout, The Netherlands, 2012a.
- Modelling of nucleation and growth of Nb-containing precipitates during thermo-mechanical processing in HSLA steels. M2i Conference, Noord-wijkerhout, The Netherlands, 2013.

